Ultralow-field NMR on Room Temperature samples using a low T_C Two-Stage DC SQUID

by

Michèle Piscitelli

A thesis submitted for the degree of
Doctor of Philosophy

Royal Holloway, University of London
2010

Abstract

This thesis describes the development of low-field Nuclear Magnetic Resonance (NMR) systems based on Superconducting QUantum Interference Device (SQUID) detection for use on room temperature samples and presents initial test results using various liquid samples.

The original proof of principle low-field SQUID NMR spectrometer consists of a cryogenic dipper probe designed for small liquid samples on the order of 100 µl, which is operated in a liquid-helium Dewar equipped with a simple µ-metal shield. The samples are kept at room temperature inside a vacuum cell placed in the centre of a compact assembly of superconducting NMR coils. The two-stage DC SQUID sensor has a coupled energy sensitivity of $\sim 50\ h$, where h is Planck's constant, at 4.2 K and is coupled to the receiver coil via a superconducting flux transformer, offering highly sensitive broadband and frequency-independent signal detection. The obstacle of small sample polarization in low magnetic fields is overcome by means of sample prepolarization.

Using the low-field SQUID NMR dipper probe, proton signals from distilled water samples were observed down to 93 nT (corresponding to a Larmor frequency of $\sim$ 4 Hz). With the benefit of sample temperature control, two-component free induction decays were obtained from oil-water mixtures at temperatures between 275 K and 300 K. The dipper probe was also extensively used to measure proton NMR relaxation times T_1 and T_2 for aqueous solutions of coated magnetite (Fe_3O_4) and cobalt-ferrite ($CoFe_2O_4$) nanoparticles in micro-Tesla fields to gain knowledge on their effectiveness as contrast agents for Low-Field Magnetic Resonance Imaging (LF-MRI).

Finally, preliminary work on the design of the follow-up SQUID NMR system is presented. It will allow for larger samples, which will be placed underneath a cryogenic low-noise Dewar, housing the SQUID sensor and receiver coil, in the centre of room temperature coils providing the static background field and polarization pulses. The whole set-up will be operated inside a two-layer mu-metal magnetically shielded enclosure that will screen out extraneous magnetic fields such as the Earth's field. With the addition of gradient coils, such a system can be used for LF-MRI test experiments.

Acknowledgements

First of all, I would like to thank my supervisor Chris Lusher, whose hard work and effort permeates this thesis. In addition to many long and enlightening discussions about all aspects of this project, he has always taken the time to listen to any of my concerns, both work-related and personal, and I consider him to be not only a mentor but also a very good friend. The same goes for Andrew Casey, who provided me with financial support in the latter stages of my PhD, but who also gave me endless and invaluable moral support during the harder times. Furthermore, without his continued enthusiasm, expertise and great instincts when it comes to practical solutions, work on the Dewar could never have progressed as fast as it did.

I am immensely grateful to my advisor John Saunders, without whom none of this would have been possible and who has been an important source of encouragement for my work. I would also like to thank Moreton Moore for being my moderator and always providing me with useful and positive feedback.

I am indebted to Rainer Körber for putting up with me and my penchant for breaking sample cells during the first years of this project and especially for teaching me all of my experimental physics craft. Similarly, I want to thank Jan Nyéki for sharing his experimental know-how, but also for being a continued source of optimism in the face of adversity and for teaching me the value of the motto 'Never give up!'.

A huge thank you goes to all of the Physics workshop staff. A special mention is reserved for Dave Bosworth, without whose most useful advice and efficient machining skills, it would have been impossible to actually construct the Dewar. I am also grateful to Alan Betts, Leon Ellison and Howard Moore for among other things, sorting out all my electrical needs and keeping me safe.

In addition, I would like to thank all of the support staff, in particular Andrea Hodgetts, Gill Green, Andy Alway, and who could forget Graham Cakebread, for helping me with all sorts of day-to-day issues. I also want to give a special thanks to Ian Murray and Francis Greenough for always being there if I needed help, advice or simply a chat.

The daily life in lab would not have been the same without my contemporaries, with whom I have shared many laughs and equipment failures. First and foremost, I'd like to thank Aya Shibahara for our collaborative work and for being a dear friend. I can't imagine being in lab without her nearby. I would also like to thank Lev Levitin for being truly unique, Rob Bennett for his cheerful enthusiasm, George Nichols for satisfying all my vacuum grease needs, Andrea Magee for having the best laugh ever and finally Giovanna Tancredi for bringing me closer to my Italian roots.

I want to thank Quentin Pankhurst and especially Hugh Seton for agreeing to be my examiners.

Finally, I would like to express my eternal gratitude to my family in Luxembourg, especially my grandparents, who had to make due without me for the entirety of my PhD. And last, but definitely not least, I am grateful for having had Ben Yager at my side through all of the toughest times and I truly cannot express in words how much his unwavering support has meant to me. I owe it all to you, babe!

Contents

List of Figures

List of Tables

Chapter 1

Introduction

In order to improve the resolution and the sensitivity of Nuclear Magnetic Resonance (NMR) and Magnetic Resonance Imaging (MRI) experiments, there has been a general move to use stronger, superconducting magnets in order to increase the sample magnetization. This is desirable since the signal sensitivity for conventional Faraday coil NMR detection is proportional to the rate of change of magnetic flux, which means that the measureable signal strength has a quadratic dependence on the magnetic field. A consequence of working in higher magnetic fields is the requirement that the magnets used to produce them need to provide a very high degree of field homogeneity, since the NMR linewidth signal broadening scales linearly with field for a fixed magnet inhomogeneity. Consequently, modern state of the art NMR and MRI instrumentation can be very expensive and complex.

A DC Superconducting QUantum Interference Device (SQUID), when operated in conjunction with an untuned, superconducting input circuit, detects magnetic flux directly, resulting in a measureable signal strength that has a linear dependence on the magnetic field. Given the fact that SQUIDs are among the most sensitive magnetometers available, using DC SQUID detection therefore opens up the possibility of measuring NMR signals in low magnetic fields, where the sample polarization is too small for detection with conventional methods. In lower magnetic fields the

requirements on magnet homogeneity also become less stringent. Furthermore, a reduction in the measurement field also reduces the signal broadening intrinsic to the sample due to local fluctuations in field resulting from susceptibility variations within the sample.

The first reported use of a SQUID in a pulsed NMR experiment was that of Webb in 1977 [1], where an RF SQUID was used to monitor the longitudinal magnetization of liquid ^{3}He. DC SQUIDs are generally more sensitive than their RF counterparts, but were harder to make reliably until they could be fabricated using lithographic techniques [2], at which point various groups started using DC SQUIDs for NMR. The faster response of the DC SQUIDs enabled the direct detection of transverse magnetization. Friedman *et al.* [3] used a DC SQUID operating in flux-locked loop mode to measure ^{3}He Free Induction Decays (FIDs) at frequencies of 0.5–50 kHz using a flux transformer input circuit. Freeman *et al.* [4] used a DC SQUID operating in open loop mode to measure ^{3}He FIDs at 1.9 MHz using a tuned input circuit. John Clarke's group at Berkeley used DC SQUIDs in open loop mode for Nuclear Quadrupole Resonance (NQR) at 30 MHz [5] and then went on to use DC SQUIDs for NMR as well [6, 7].

In order to operate and to benefit from the improved sensitivity, the low T_C SQUIDs and NMR coils need to be kept at liquid helium temperatures, which presents a potential difficulty for measuring room temperature samples. Consequently, as evidenced in the 1998 review on SQUID NMR by Greenberg [8], much of the early work was carried out on cryogenic samples. Nevertheless, two different approaches for performing SQUID NMR on room temperature samples were already being used at this stage. Kumar *et al.* [9, 10] used a Dewar with a room temperature bore, while Seton *et al.* [11, 12] performed MRI measurements on samples that were placed directly under a specially modified Dewar [13], with the DC SQUIDs operating in a fast flux-locked loop mode and using a tuned input configuration.

In 2002 the Berkeley group published an article in Science [14] where they used DC SQUID NMR with a prepolarizing pulse, for measurements on liquid room temperature samples in micro-Tesla magnetic fields. The prepolarization technique had been employed previously by Packard and Varian [15], but this was the first time it had been used with SQUIDs. Further work on room temperature samples in low magnetic fields using the prepolarizing technique was carried out at PTB [16] and the Berkeley group went on to apply this technique to low-field MRI [17, 18]. In recent years, the group at Los Alamos has made significant progress in the development of SQUID-based ultralow-field MRI instrumentation [19], which has been adapted to perform MRI measurements of the human brain in combination with magnetoencephalography (MEG) [20] and for the detection of liquid explosives [21]. While the majority of the recent SQUID NMR work has been focussed on the use of low T_C DC SQUIDs, the group at Jülich for example have used high T_C RF SQUIDs, that are cooled using liquid nitrogen, to look at room temperature samples in the Earth's magnetic field [22].

The Low Temperature group at Royal Holloway started using SQUID NMR in the early 1990's, when initial measurements were carried out on ^{195}Pt in platinum powder [23] using a commercial DC SQUID from Quantum Design [24]. Following these measurements, a longstanding collaboration with the Cryosensors group at PTB [25] was set up, enabling the use of wide bandwidth DC SQUID systems operating in flux-locked loop mode out to frequencies of a few MHz. In recent years all NMR measurements have been carried out using SQUIDs fabricated at PTB, whose sensitivity improved with time. The earlier SQUIDs from PTB used additional positive feedback (APF) [26] to skew the flux-to-voltage characteristic, thereby amplifying both the signal and noise to allow the SQUID noise to determine the signal-to-noise ratio. As fabrication techniques improved, the APF SQUIDs were replaced first by SQUID arrays [27] and finally by Two-Stage SQUIDs, consisting of a single SQUID first stage and a SQUID array preamplifier [28].

At Royal Holloway SQUID NMR has been used to study a wide range of systems with low spin density at cryogenic temperatures, as outlined in [29]. Both tuned and broadband input circuits [30] were used for these measurements. Examples include thin slabs of superfluid ^{3}He with an area on the order of 1 cm^2 [31], very thin films of solid ^{3}He adsorbed on graphite [32], single-crystal samples of UPt_3 at low temperatures, where low fields are required to reduce eddy-current heating [33] and ^{3}He adsorbed in the pores of the molecular sieve MCM-41, a potential quasi-1D model system at low temperatures [34].

The work presented in this thesis was part of a programme of research aimed at developing our SQUID NMR techniques and instrumentation so that they could be applied to room temperature samples. As mentioned above, one difficulty here is that the SQUID sensors need to be operated at liquid helium temperatures, but the samples need to remain at room temperature. The solution that we adopted initially was to put the sample in a vacuum cell, so that it could be immersed in the liquid helium bath with the SQUID and the NMR coils while being kept at room temperature using a heater. This was technically demanding and this thesis gives a detailed account of the development of this set-up, which was evaluated using various liquid samples such as water, oil-water mixtures and aqueous solutions of magnetic nanoparticles, the results of which are also presented and analyzed. Furthermore, it includes a discussion of the initial development of a successor low-field NMR system, where the samples are placed outside a home-built Dewar, following the approach used by Seton *et al.* [12].

This thesis has been organized into 6 further chapters as follows: Chapter 2 gives a brief description of the main concepts of NMR and SQUID detectors. Chapter 3 describes the low-field NMR spectrometer cryogenic dipper probe used for all the NMR measurements presented in the thesis. Chapter 4 deals with the NMR measurements on liquid samples, specifically water, oil and oil-water mixtures, designed to test the performance of the probe described in the previous chapter. Chapter 5

gives a brief overview of the physical properties of magnetic nanoparticle suspensions and provides the necessary theoretical background regarding the relaxation behaviour of the protons in such solutions to allow for interpretation of the results presented in the subsequent chapter. Chapter 6 summarizes extensive NMR measurements on aqueous solutions of magnetic nanoparticles, which were evaluated for their potential use as contrast agents in low-field MRI. Finally, Chapter 7 presents current work on a follow-up low-field NMR system that is being developed.

Chapter 2

SQUID-detected Nuclear Magnetic Resonance

Nuclear Magnetic Resonance (NMR) was first used to investigate bulk matter in 1946, as described in two papers published independently in the same volume of Physical Review, by Purcell, Torrey and Pound [35] and by Bloch, Hansen and Packard [36]. Since then NMR measurements have found a wide range of applications. NMR instrumentation is continuously evolving and has benefited from the introduction of more sensitive magnetic flux detectors, such as the Superconducting QUantum Interference Device, commonly known as a SQUID [8]. This chapter gives a brief overview of the relevant physical concepts relating to SQUID-detected NMR. More detailed accounts of the theory behind NMR can be found in the books by Cowan [37], Slichter [38] and Abragam [39]. A comprehensive guide to SQUIDs and their applications is provided in the SQUID Handbook [40].

2.1 Nuclear Paramagnetism

A nucleus has a magnetic moment μ that is related to its total spin angular momentum I by the gyromagnetic ratio γ according to

$$\mu = \gamma \hbar I \tag{2.1}$$

The value of γ depends on the nucleus, as different elements have different gyromagnetic contants. The energy spectrum E associated with a nuclear magnetic moment in a magnetic field $\mathbf{B}_0$ is given by

$$E = -\boldsymbol{\mu} \cdot \mathbf{B}_0 = -m_i \hbar \gamma B_0 = -m_i \hbar \omega_0 \tag{2.2}$$

where ω_0 is the so-called Larmor frequency and $m_i = -I, -I+1, \ldots, I$ is the spin quantum number.

The NMR experiments described in this thesis are performed exclusively on protons contained in liquids. Protons possess a nuclear spin of $I = \frac{1}{2}$, such that in a magnetic field the energy splits into two states where $m = -\frac{1}{2}$ (spin antiparallel to B_0) and $m = +\frac{1}{2}$ (spin parallel to B_0) correspond to the higher and lower energy levels respectively. This situation is depicted in Figure 2.1.
The population density of the higher energy level is indicated by $N_\downarrow$ (spin down) and the lower energy level by $N_\uparrow$ (spin up). In thermal equilibrium the proportion of this two-level system is governed by Boltzmann statistics

$$\frac{N_\downarrow}{N_\uparrow} = \exp\left(-\frac{\Delta E}{kT}\right) \tag{2.3}$$

where $\Delta E = \hbar \gamma B_0$ for a $I = \frac{1}{2}$ system and k is the Boltzmann constant. The population difference $(N_\uparrow - N_\downarrow)$ results in a net magnetization $M_0 = \mu\,(N_\uparrow - N_\downarrow)$. For high temperatures T and/or low magnetic fields, such that

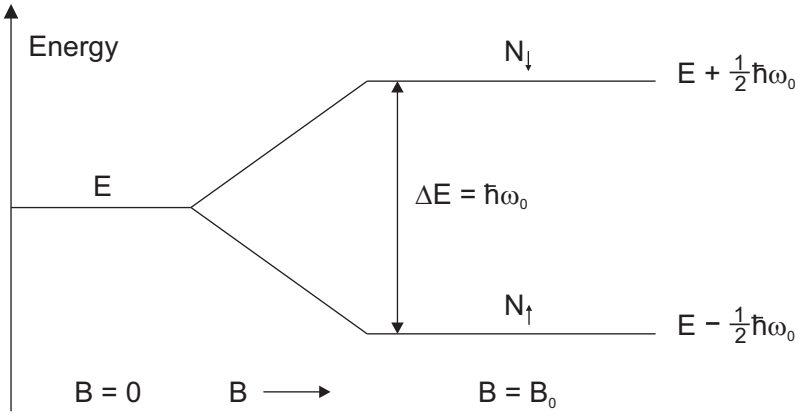

Figure 2.1: Nuclear Zeeman splitting of the energy levels for a nucleus with $I = \frac{1}{2}$ in a magnetic field B_0.

$$\hbar\gamma B_0 \ll 2kT \tag{2.4}$$

the equilibrium net magnetization follows Curie's law in which M_0 is proportional to B_0 and inversely proportional to T

$$M_0 = \frac{N_v \hbar^2 \gamma^2}{4kT} B_0 \tag{2.5}$$

where $N_v = N_\uparrow + N_\downarrow$ is the total number of spins per unit volume. Thus for a given temperature, the higher the applied field, the greater the sample polarization. With the static magnetic susceptibility χ_0 defined as

$$\chi_0 = \frac{\mu_0 N_v \hbar^2 \gamma^2}{4kT} \tag{2.6}$$

where $\mu_0 = 4\pi \times 10^{-7}\,\mathrm{H/m}$ is the permeability of free space, Equation 2.5 can be rewritten as

$$M_0 = \frac{\chi_0}{\mu_0} B_0 \tag{2.7}$$

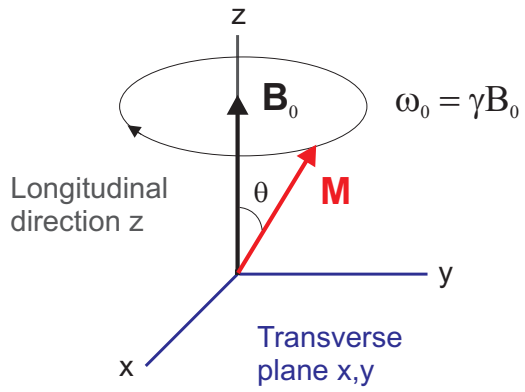

Figure 2.2: Larmor precession of the magnetization vector.

Nuclear magnetic moments in an externally applied static magnetic field will align themselves with this field, such that in thermal equilibrium the net magnetization lies along the direction of B_0. If the magnetization is tipped away from B_0 as a result of an NMR excitation pulse, it will start precessing around B_0 at the Larmor frequency introduced in Equation 2.2 and given by

$$\omega_0 = \gamma B_0 \tag{2.8}$$

The precession frequency is directly proportional to the strength of the applied static field B_0. It is the precession of the nuclear moments at their Larmor frequency that provides a detectable signal for NMR experiments.

For protons, $\gamma = 2.675 \times 10^8\,\mathrm{s^{-1}T^{-1}}$ or $\gamma/2\pi = 42.577\,\mathrm{MHzT^{-1}}$.

2.2 Pulsed NMR Principles

In pulsed NMR experiments a sample of nuclear spins is placed in a polarizing static magnetic background field B_0 to generate an equilibrium magnetization M_0 in the sample according to Equation 2.7. By convention, B_0 and hence M_0 point along the z-direction, which is generally referred to as the longitudinal direction. The sample is subsequently subjected to an electromagnetic tipping pulse to knock the magnetization M_0 off equilibrium and into the x-y plane, also known as the transverse plane. Upon removing the pulse, the resulting transverse magnetization vector will start to precess around the background field B_0, as illustrated in Figure 2.2, while the component of its magnitude in the transverse plane decays back to zero. Simultaneously the original magnetization in the longitudinal direction will be recovered as the moments realign with B_0. The time constants associated with these two equilibrating processes are the so-called relaxation times, T_1 and T_2.

2.2.1 Relaxation Mechanisms

Spin-lattice Relaxation Time T_1

T_1 is known as the spin-lattice relaxation time or longitudinal relaxation time and characterizes the time it takes for the magnetization parallel to the applied static field to grow to its equilibrium value. This relaxation refers to the longitudinal component of the magnetization M_z. According to Bloch [41] the longitudinal relaxation process is described by

$$\dot{M}_z = \gamma \left| \mathbf{M} \times \mathbf{B} \right|_z - \frac{M_0 - M_z}{T_1} \tag{2.9}$$

with the solution

$$M_z = M_0 - [M_0 - M(0)] \exp(-t/T_1) \tag{2.10}$$

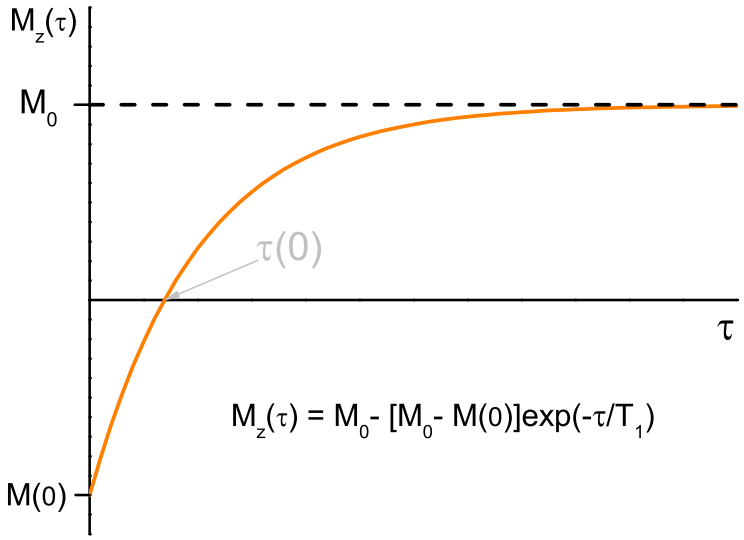

Figure 2.3: Longitudinal magnetization growing with time constant T_1.

This expression shows that the magnetization is recovering to its equilibrium value M_0 exponentially with the characteristic time constant T_1, see Figure 2.3. During the relaxation process the energy $-\mathbf{M}\cdot\mathbf{B}$ is released, hence there has to be an energy exchange mechanism in which the spin system couples to its surrounding or "lattice" and thus T_1 is a measure of how effectively the nuclear spins couple to the lattice.

Spin-spin Relaxation Time T_2

This relaxation applies to the transverse magnetization $M_{x,y}$ and is given by

$$\dot{M}_{x,y} = \gamma \left|\mathbf{M} \times \mathbf{B}\right|_{x,y} - \frac{M_{x,y}}{T_2} \tag{2.11}$$

with the solutions

$$M_x = M_x(0)\sin(\omega_0 t)\exp(-t/T_2) \tag{2.12}$$

$$M_y = M_y(0)\cos(\omega_0 t)\exp(-t/T_2) \tag{2.13}$$

Spin-spin relaxation does not require an energy exchange with the lattice and the Zeeman energy is unaltered. The local magnetic field that each nucleus sees is not constant throughout the sample and therefore the spins precess at slightly different rates. A destructive interference of the precessing spins leads to the magnetization in the xy-plane decaying to zero. Intrinsic field variations can be due to neighbouring nuclear spins or electronic magnetization. A contribution to the field inhomogeneity originates also from the NMR magnet. The measured effective spin-spin relaxation time T_2^* differs from the true T_2 and is given by the following relation:

$$\frac{1}{T_2^*} = \frac{1}{T_2} + \gamma \Delta B \tag{2.14}$$

where ΔB is the spread in the field of the NMR magnet, known as its inhomogeneity. When $T_2 \gg T_2^*$, T_2 is usually measured by the Spin-Echo method described in Section 2.2.3. For $T_2 \approx T_2^*$ one can determine T_2 by measuring the dependence of T_2^* on the magnetic field B since $\Delta B \propto B$ is usually fulfilled, such that the relative inhomogeneity obeys:

$$\frac{\Delta B}{B} = \alpha \tag{2.15}$$

where α is a constant. Determining the T_2^* field dependence therefore also presents a technique to measure the field homogeneity of an NMR magnet.

In a conventional pulsed NMR experiment, the sample is polarized in the longitudinal direction and the resulting magnetization is then tipped into the transverse plane for detection. The resulting signal, referred to as a Free Induction Decay (FID) and shown in Figure 2.4, is composed of an oscillating component at the Larmor frequency and a decaying component that is exponential with a time constant T_2^* as described by Equation 2.13.

2.2.2 Fourier Analysis

The decaying magnetization signal is recorded as a voltage signal of the form:

$$V(t) = V_0 \cos(\omega_0 t) \exp(-t/T_2) \tag{2.16}$$

The corresponding frequency spectrum is obtained by applying a Fourier transform to the time domain voltage signal. The Fourier transform in this case is defined as:

$$F(\omega) = \int_{-\infty}^{+\infty} \exp(i\omega t) V(t) dt \tag{2.17}$$

The modulus of this Fourier transform is:

$$|F(\omega)| = \frac{V_0}{2\left(\frac{1}{(T_2^*)^2} + (\omega - \omega_0)^2\right)^{1/2}} \tag{2.18}$$

The square of the modulus is a Lorentzian for which the full width at half maximum (FWHM) $\Delta\omega$ is related to the effective spin-spin relaxation time T_2^* as follows:

$$T_2^* = \frac{2}{\Delta\omega} = \frac{1}{\pi \Delta f} \tag{2.19}$$

The Lorentzian peak given by the square of the Fourier transform of the exponential FID signal is illustrated in Figure 2.4. The magnitude S_p of the discrete Fourier transform peak of the FID is related to the initial voltage V_0 in the time domain by:

$$S_p = \frac{V_0 T_2^*}{2\Delta} \tag{2.20}$$

where the Nyquist frequency $1/2\Delta$ depends on the time between data points in the time domain Δ. As a rule of thumb, one also has to capture the FID for a time of order $5 \times T_2^*$ in order to avoid a line distortion caused by the truncation of the time domain signal.

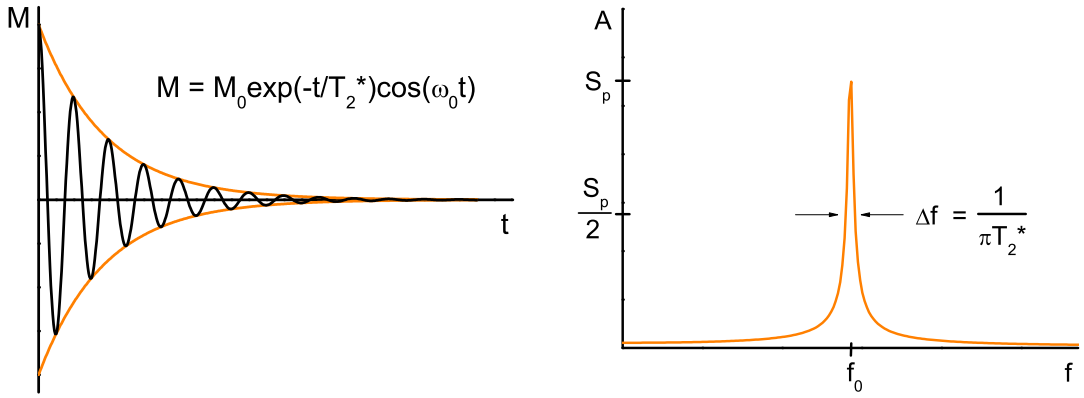

Figure 2.4: Free Induction Decay (FID) in the time domain and Fourier transformed Lorentzian signals in the frequency domain.

2.2.3 Conventional NMR Measurement Techniques

In conventional pulsed NMR, a transmitter coil oriented perpendicular to the applied field B_0, is used to transmit an oscillating RF tipping pulse at the Larmor frequency ω_0. From their rotating frame of reference, spins aligned with B_0 will see a large static field B_1 in the transverse plane and start to rotate around B_1 with the corresponding Larmor frequency γB_1. By varying the length of the B_1 pulse, the sample magnetization along B_0 can be rotated through an arbitrary angle. The amplitude of the RF pulse is usually calibrated for a given pulse length to obtain either a 90° or 180° pulse, where a 90° pulse transfers the magnetization into the transverse plane and a 180° pulse aligns it along $-B_0$. Spins precessing coherently in the transverse plane produce an oscillating signal that is coupled to a receiver coil connected to a detector.

The two most important pulse sequences are the $90° - \tau - 180°$ and $180° - \tau - 90°$ sequences, where the variable τ is the time between pulses. The $90° - \tau - 180°$ sequence is called a Spin-Echo sequence and allows for direct measurement of the intrinsic T_2, due to the 180° pulse resulting in a temporary rephasing of the spins that have already dephased because of the magnet inhomogeneity after a time 2τ.

To measure T_1, a $90°-\tau-90°$ sequence can be used, which allows the longitudinal magnetization to grow back to its equilibrium value for a time τ, before using a second 90° pulse to tip it back into the transverse plane for read out. A more common method is to use a $180° - \tau - 90°$ sequence, also known as an Inversion Recovery Sequence, to start off with the magnetization in $-B_0$ in order to trace the equilibrium magnetization recovery as depicted in Figure 2.3. The measured or interpolated time $\tau(0)$ for which the magnetization along z is 0, also known as the zero-crossing point, can be used to calculate T_1 from the relation [37]:

$$T_1 = \tau(0)/\ln 2 \tag{2.21}$$

2.3 NMR in Low Magnetic Fields

In low fields the magnetic response to be measured is very small and much averaging is necessary with conventional spectrometers in order to obtain any useful information. Through the use of SQUIDs in NMR, it becomes practically feasible to measure such small signals in a comparatively short time, since SQUID magnetometers are unequalled in their resolution and sensitivity to magnetic flux. They can measure magnetic fields down to fractions of 1×10^{-15} T, which is about ten orders of magnitude smaller than the Earth's magnetic field.

But in addition to being able to detect very small signals it is still necessary to achieve a large enough sample polarization to generate signals that reach above the noise background with a reasonable amount of averaging. To this end the loss in magnetization due to the lowering of the static magnetic field strength can be compensated for by subjecting the sample to a DC prepolarizing pulse, as demonstrated by McDermott *et al.* [14]. For a given polarizing pulse that is large compared with B_0, we will always obtain the same amount of transverse magnetization, regardless of the static magnetic background field strength. Consequently, since the area under the NMR line is related to the initial magnetization of the sample in the detection plane, the area will remain constant, independent of the applied static field.

If the area of the signal remains constant, then the narrower its width, the bigger its peak height will be. Therefore, since the NMR linewidth decreases with decreasing field because the broadening effect due to the magnet inhomogeneity is reduced, the prepolarizing technique has the added benefit of an increased signal size at lower fields. This also means that for an approximately constant noise background, the signal-to-noise ratio (SNR) will improve as you go down in field [14]. Both effects are shown in Figure 4.1 in Chapter 4.

2.3.1 Measuring T_2^* using Sample Prepolarization

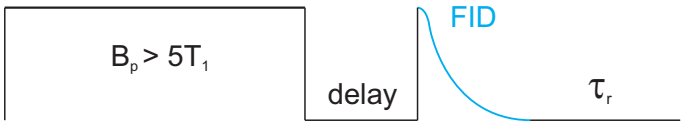

Figure 2.5: Pulse sequence for measuring T_2^* with a prepolarizing field in the transverse plane, where τ_r is the repetition time.

In the prepolarizing technique, a large DC current is sent through the transmitter coil [14]. This produces a static magnetic field B_p in the transverse plane that is large compared with B_0, so that the net magnetization of the sample will grow in the transverse plane up to an equilibrium value that is proportional to B_p. Hence, polarizing pulses need to be long enough for the transverse magnetization to grow sufficiently, *i.e.* several T_1s. As depicted in Figure 2.6, the magnetization grows with T_1 in the prepolarizing field B_p and then upon removal of B_p starts precessing at the Larmor frequency $\omega_0 = \gamma B_0$ in the transverse plane, giving a signal that decays with the time constant T_2^*. For precession to occur, B_p has to be removed non-adiabatically. This is discussed further in Section 4.2.1. Figure 2.5 shows a schematic of the simple pulse sequence needed to measure T_2^* at low fields.

2.3.2 Measuring T_1 in the Prepolarizing Field

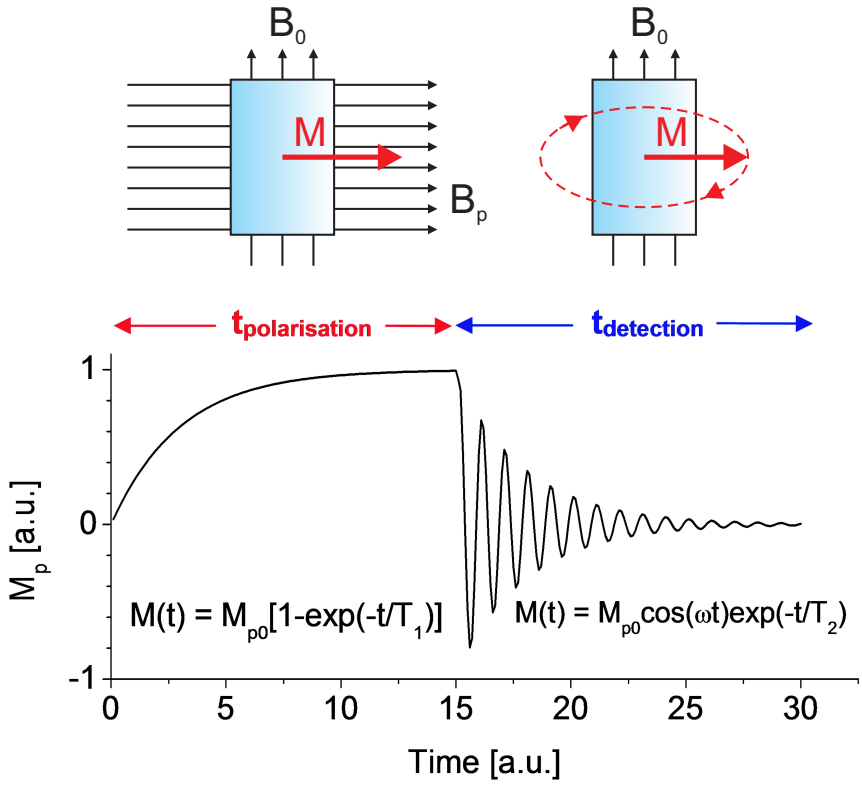

Figure 2.6: Sample prepolarization and resulting FID.

The T_1 relaxation time in the prepolarizing field is determined by varying the length of the prepolarizing pulse. The magnetization grows in the prepolarizing field with a time constant T_1 for that field, see Figure 2.6 again, so that the signal height obtained in the transverse plane after switching the prepolarizing field off will depend on the time the pulse was on for.

2.4 DC SQUID Magnetometers

2.4.1 DC SQUID Characteristics

A DC Superconducting QUantum Interference Device consists of a loop of superconductor containing two Josephson junctions in parallel [40], as shown in Figure 2.7. SQUIDs exploit the quantum-mechanical phenomenon of flux quantization. A current flowing around a closed loop produces a magnetic field threading through it and vice versa. In the case of a superconducting loop, the magnetic flux threading it cannot take on any arbitrary value, but is quantized in integral multiples of $h/2e = \phi_0$, where h is Planck's constant $\phi_0 = 2 \times 10^{-15}\,\mathrm{Tm}^2$ is the flux quantum.

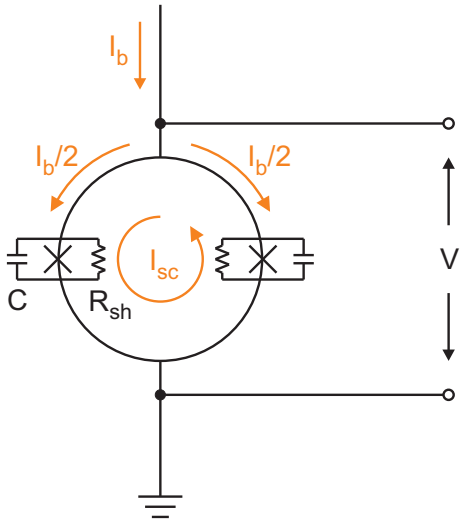

Figure 2.7: Schematic of a SQUID. The crosses represent the Josephson junctions.

If the flux through such a loop is a non-integer multiple of ϕ_0, a screening current I_{SC} will flow in the loop to generate an opposing or additional field, such that the total flux threading the loop remains $n\phi_0$. Therefore, as can be seen in Figure 2.7, the total current in each branch of a SQUID is given by $I = \frac{1}{2}I_b \pm I_{SC}$, where I_b is the applied bias current.

A Josephson junction consists of a thin layer of insulating material separating two superconductors. The electron Cooper pairs in a superconductor are described by a single wavefunction and can tunnel through such junctions, making them act like weak superconductors. This is known as the DC Josephson effect. The Josephson junctions therefore determine the critical current I_C that can pass through the SQUID without resistance. The bias current that can be applied without exceeding the critical current, will be at a maximum if $I_{SC} = 0$. The $I - V$ curve for a SQUID is inherently hysteretic, but this behaviour is suppressed by the addition of a shunt resistance R_{sh} in parallel with each Josephson junction, provided that the hysteresis parameter β_c fulfills the condition [40]

$$\beta_c \equiv 2\pi I_0 R_{sh}^2 C/\phi_0 \leq 1 \tag{2.22}$$

where I_0 and C are the critical current and the self-capacitance of the junction respectively.

If the total current flowing in the SQUID stays below I_C, the voltage measured across it remains zero. But when biasing the SQUID with a current that is close to the maximum critical current of the Josephson junctions, changes in the screening current produced by changes in the external magnetic field, will result in a measureable periodic voltage change across the SQUID, depicted by the typical $V - \phi$ characteristic in Figure 2.8. It shows the $V - \phi$ curve of a SQUID to be non-linear, except for an approximately linear regime around the chosen working point W, such that when operating the SQUID at W, for small enough signals, it acts as a linear flux to voltage converter. By applying a voltage bias V_b and a flux bias ϕ_b, W can be set to the steepest part of the $V - \phi$ curve. The gain for small signals is then given by the gradient $V_\phi = \delta V/\Delta\phi$ at the working point. The bias current I_b can be adjusted to obtain the largest V_ϕ.

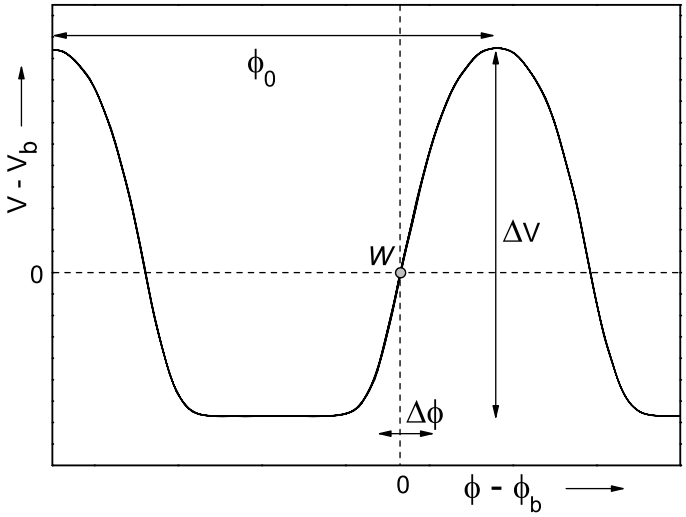

Figure 2.8: V-ϕ characteristic of a DC SQUID with working point W biased at V_b and ϕ_b, a voltage swing ΔV and the linear flux regime $\Delta\phi$.

2.4.2 FLL Mode Operation

In order to extend the range of the linear $V-\phi$ regime, the DC SQUID is operated as part of a Flux-Locked Loop (FLL), implemented through a Direct Offset Integration Technique (DOIT) FLL scheme after Drung [42]. This works essentially as a negative feedback system where the SQUID is used as a null-detector.

A voltage V developing across the SQUID is coupled to a room temperature low noise differential amplifier, giving an error voltage $V_e \propto V - V_b$ that is further amplified to give a feedback voltage V_f. V_f is then applied across the feedback resistor R_f, delivering a current I_f that is fed back into the SQUID as a flux via a feedback coil with inductance L_f (see Figure 3.3 in Chapter 3). The feedback flux ϕ_f is given by

$$\phi_f = M_f I_f = -\phi_{SQ} \tag{2.23}$$

where M_f is the mutual inductance between the SQUID and the feedback coil. ϕ_f exactly cancels the signal flux ϕ_{SQ}, thus keeping the total flux ϕ in the SQUID constant. The signal gain of the SQUID when operated in FLL mode, is given by

$$G_{FLL} = \frac{R_f}{M_f} \tag{2.24}$$

The dynamic behaviour of the FLL circuit is characterized by its bandwidth of typically a few MHz and its slew rate. If a signal coupled to the SQUID produces a feedback flux that exceeds the slew rate of the FLL electronics, it results in flux jumps and correspondingly discontinuous jumps in the output voltage.

2.4.3 Total Flux Noise

The overall noise in the circuit is comprised of three elements. The intrinsic flux-noise spectral density of the SQUID S_{SQ} stems from Johnson noise in the shunt resistors. The voltage and current noise of the preamplifier are taken into account by voltage noise source $V_{N_{amp}}$ and current noise source $I_{N_{amp}}$ terms. The total flux noise spectral density S_ϕ is then given by:

$$S_\phi = S_{SQ} + \frac{V_{N_{amp}}^2}{V_\phi^2} + \frac{I_{N_{amp}}^2 R_{dyn}^2}{V_\phi^2} \tag{2.25}$$

where R_{dyn} is the dynamic resistance of the SQUID at the working point. The problem associated with coupling the SQUID directly to the preamplifier is that the noise is usually dominated by the latter. It is necessary to enhance V_ϕ in order to make the preamplifier noise contribution negligible. One way this can be achieved is by using a Two-Stage SQUID, where a SQUID array is used to amplify the signal from the first stage SQUID, before connecting to the FLL electronics. Two-Stage SQUIDs have been used for all the work presented in this thesis.

2.4.4 Coupled Energy Sensitivity

A figure of merit of a SQUID is the coupled energy sensitivity ε_c, *i.e.* the energy equivalent of the minimum detectable current in the SQUID input coil, given by

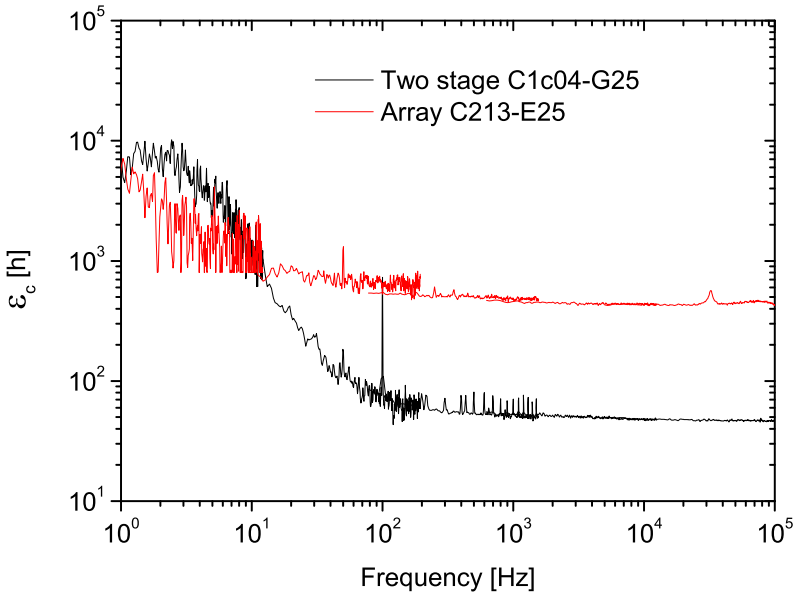

Figure 2.9: Comparison of coupled energy sensitivity of a SQUID array and a Two-stage SQUID sensor (open input coil).

$$\varepsilon_c = \frac{\langle \phi_N^2 \rangle \, L_i}{2M_i^2} \tag{2.26}$$

where L_i is the input coil inductance, M_i is the mutual inductance between the input coil and SQUID and $\langle \phi_N^2 \rangle^{1/2} = \sqrt{S_\Phi}$ is the total rms flux noise per $\sqrt{Hz}$. If the noise is dominated by the noise in the SQUID, then $\langle \phi_N^2 \rangle \approx \sqrt{S_{SQ}}$.

The most significant advantage of Two-Stage sensors over the previously used arrays is the decrease in coupled energy sensitivity ε_c, resulting from the higher mutual inductance M_i between the single front end SQUID and the input coil, that are coupled via a double transformer to match up their respective inductances, as described by Drung *et al.* [28]. Figure 2.9 shows a comparison of the coupled energy sensitivities of an array and a Two-Stage sensor. It can be seen that ε_c is as low as 50 h in the white noise region. This improvement of an order of magnitude over the array results in an order of magnitude decrease in measuring time for a given signal amplitude.

Chapter 3

Low-Field NMR DC SQUID Spectrometer Probe

This chapter describes the DC SQUID spectrometer probe used for performing low-field NMR measurements on small liquid samples at room temperature. After an overview of the set-up as a whole, a section summarizing the specifications of the SQUID sensors used is followed by detailed descriptions of the superconducting NMR coils and the sample cells. The final section describes the development of a second generation probe and general modifications to the set-up leading to an improved signal-to-noise ratio.

3.1 Overview of the Spectrometer

The low-field SQUID NMR spectrometer probe set-up incorporates a compact shielding arrangement comprising both superconducting shields on the probe and an external high permeability magnetic shield made of mu-metal surrounding a designated liquid helium Dewar. Sufficient shielding is an essential requirement for performing NMR in low fields, due to the need to screen the sample region as much as possible from interfering sources of noise and from the Earth's field.

A schematic of the magnet assembly and positioning of the NMR coils is shown in Figure 3.1. The whole assembly has a cylindrical geometry. The sample is contained inside a Kel-F (PTCFE) vacuum cell in a container machined from Stycast 1266 epoxy resin that can hold a liquid volume of $\sim 0.14\,\mathrm{ml}$. The sample holder, which had to be modified for the experiments described in Chapter 6, is described further in Section 3.4. The NMR coil-set comprises a saddle receiver coil inside an orthogonal saddle transmitter coil, both of which are wound from superconducting niobium-titanium wire. More detail on the pick-up and excitation coils is given in Sections 3.3.3 and 3.3.2. The receiver coil is placed closest to the sample and is connected to the input terminals of the SQUID sensor via a superconducting flux transformer. The transmitter coil is kept orthogonal to the receiver coil in order to minimize cross-coupling.

The coil-set is placed inside a home-built superconducting magnet, described in Section 3.3.1, that is operated in persistent mode and placed inside a superconducting shield. The shield serves to screen the sample from any extraneous magnetic fields. An open-ended superconducting shield made from overlapping niobium foil is inserted between the magnet and the transmitter coil. This shield serves to reduce the transient response due to eddy currents in the copper magnet former arising from the prepolarizing pulse.

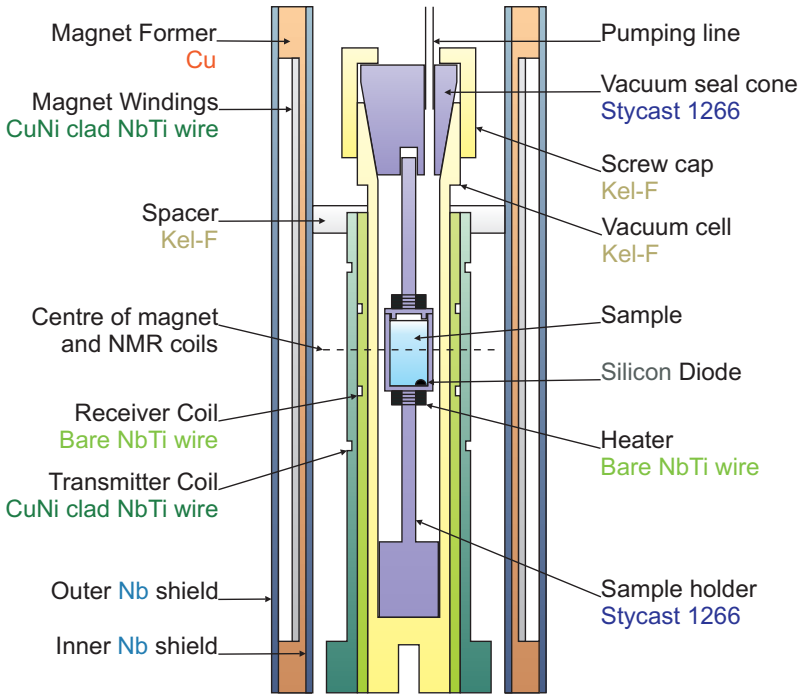

Figure 3.1: Schematic of the compact NMR coil configuration and sample space.

A greased spacer is fitted inside the inner overlapping shield and around the top of the NMR coils, to prevent unwanted vibration and magneto-acoustic noise, by improving the rigidity of the coilset. The magnet, NMR coils and vacuum cell are all screwed down onto the magnet base plate to fix their alignment relative to each other and to ensure mechanical stability.

The SQUID in its closed cylindrical niobium shield, as well as the magnet and NMR coils, all need to be kept at 4.2 K in order to be superconducting and are therefore mounted on a dipper probe designed for use in a liquid helium Dewar that has a single layer cylindrical mu-metal shield with a closed end at the bottom. Mu-metal is a high permeability nickel alloy that keeps out stray magnetic fields from the area it encloses by providing a low resistance path for them. Figure 3.2 shows a plot of the field profile inside the mu-metal shielded Dewar, measured using a Bartington [43] triple-axis fluxgate magnetometer.

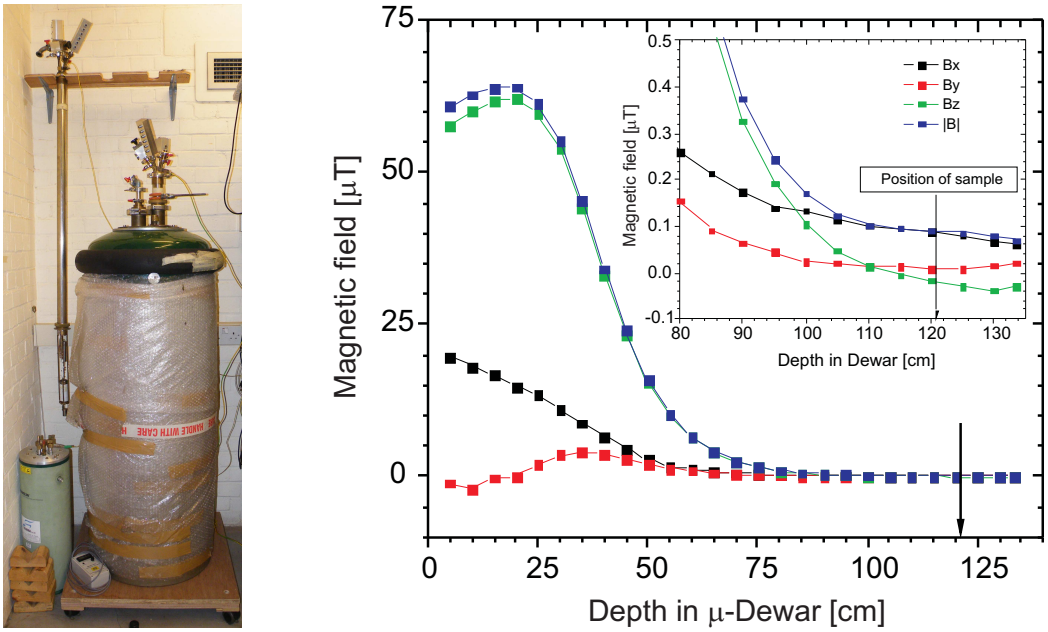

Figure 3.2: Left: Photograph of the mu-metal shielded Dewar holding the second generation spectrometer probe and the original probe hanging on the wall next to them; Right: Field profile inside the mu-metal shielded Dewar, with the arrow indicating the position of the liquid sample when the probe is in place. The insert shows a blow-up of the sample region inside the Dewar.

When the probe is cooled down, it is inserted all the way into the Dewar, where the shielding is optimal, before the liquid helium transfer is carried out, in order to ensure that the magnet assembly goes superconducting in an environment with minimal field gradients.

Since the probe is used for NMR on room temperature samples, which need to be positioned in the centre of the magnet and NMR coils in their cryogenic environment, the samples are kept at room temperature using a heater while immersed in the liquid helium. For this reason the sample holder is placed inside a vacuum cell in order to avoid direct thermal contact with the helium bath. The warm-cold distance between the sample and the helium bath is about 1 mm. The sample is heated using a resistive heater wound non-inductively from niobium-titanium wire. The temperature of the sample is monitored using a silicon diode. This set-up allows the sample temperature to be varied easily between 4.2 K and 300 K.

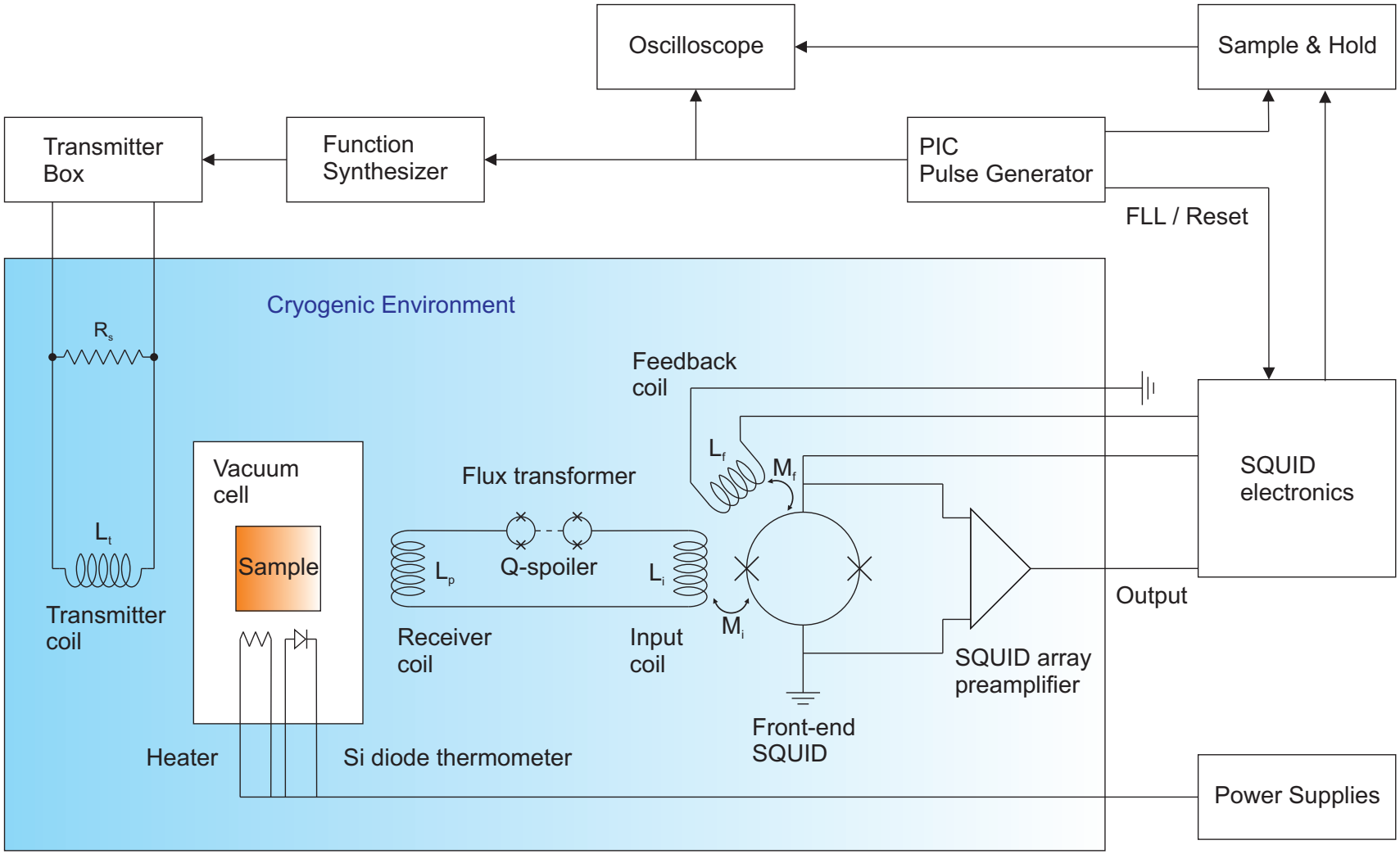

Figure 3.3: Schematic of the SQUID spectrometer set-up.

Figure 3.3 shows a schematic overview of the spectrometer set-up. The SQUID electronics are in reset mode whilst the prepolarizing pulse is applied and are put back into FLL mode for data capture. A sample-and-hold unit removes any DC offset at the output of the FLL electronics before the resulting FID is captured on a 12-bit A-D card [44] or a TS410 oscilloscope [45]. The SQUID has to be in the open loop mode while the transmitter pulse is on due to the cross-coupling between the transmitter and receiver coils. The quicker the prepolarizing pulse switches off, the sooner FLL operation can resume. The pulse can be removed rapidly and non-adiabatically at all accessible fields. Non-adiabatic removal of the pulse is necessary to preserve the magnetization in the transverse plane. In certain circumstances, the pulse is removed adiabatically, as described in Section 4.2.1. The shortest dead time of the system is $\approx 300\,\mu s$. It is limited by transients from the prepolarizing pulse and is significantly shorter than the dead times achieved by McDermott *et al.* [14] and Burghoff *et al.* [16]. The SQUID noise was found to be the limiting noise source in the spectrometer. The observed signal sizes were consistent with those calculated using the principle of reciprocity [30].

3.2 Two-Stage DC SQUID magnetometer

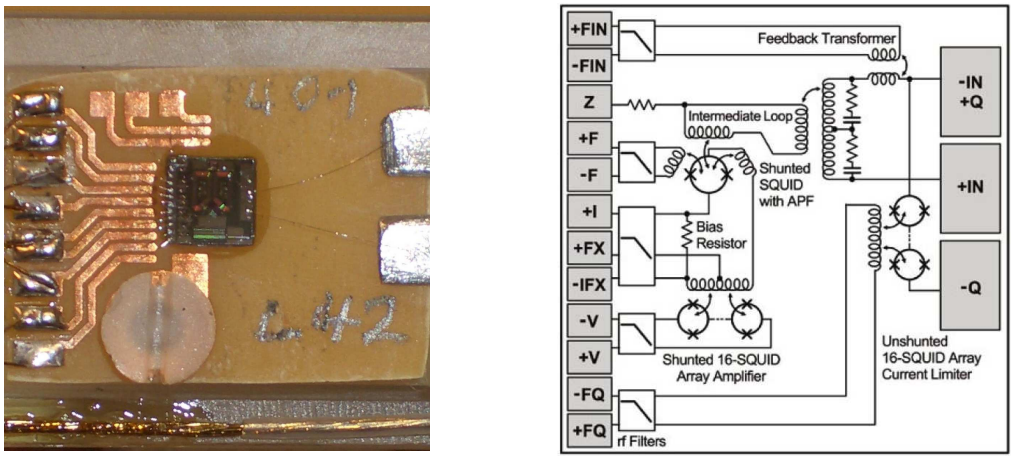

Figure 3.4: Left: Photograph of the Two-Stage SQUID chip and its connection terminals; Right: Schematic of Two-Stage SQUID chip.

We are working exclusively with SQUIDs made from low T_C superconductors, because of the reduced thermal noise at liquid helium temperatures. Rather than using a single SQUID sensor, we were previously working with SQUID arrays, provided by Physikalisch Technische Bundesanstalt (PTB) [25] and controlled by Magnicon SEL-1 FLL SQUID electronics [46], because of the large voltage swing and wide linear range in their $V - \phi$ characteristic. These are desirable qualities for optimum system dynamics and are necessary to allow for direct and fast read-out with the electronics. Provided that all individual SQUIDs of an array are biased at the same working point and that the same flux is coupled into each one, the array will behave like a single SQUID with an enlarged voltage signal and increased gain. However, one drawback of using arrays is that, when they are cooled in large external magnetic fields such as the Earth's field, the $V - \phi$ may become strongly distorted due to trapped flux causing variations in the flux biases of the SQUIDs. Furthermore they developed malfunctions after prolonged use.

Prior to starting any of the work presented in the subsequent chapters, we upgraded to PTB C3 and C4 generation SQUID sensors [28], designed to be operated using Magnicon XXF-1 FLL electronics [27]. These latest sensors are so-called Two-Stage devices that consist of a front-end single SQUID into which the input signal is coupled and which is then preamplified by an array of 16 further SQUIDs, before being amplified by the XXF electronics, where the gain of the room temperature amplifier is 2000. All of the SQUIDs in the array are designed as gradiometers and have a maximum linewidth of 5 µm [28], which improves the problem of trapped flux encountered with previous SQUID array sensors by reducing the amount of flux coupled to each SQUID due to external magnetic fields. In addition, the Two-Stage chips can be heated above the T_C of the SQUIDs using the XXF electronics, in order to expel trapped flux in the second stage array, which also allows for the Two-Stage sensors to be cooled down in an unshielded environment.

As noted in Section 2.4.4, having a single front-end SQUID coupled to the input coil via a double flux transformer scheme, results in a higher mutual inductance between the SQUID and the input coil. While it was ~ 1.1 nH for the array sensors, for the Two-Stage sensors used here we have $M_i \sim 7$ nH, with an inductance of $L_i \sim 1.1$ µH for the integrated input coils. The Two-Stage SQUID sensors are also designed to be coolable down to 300 mK to achieve even better noise performance. But in our case the SQUID operation temperature remains at 4.2 K.

The results presented in Chapter 4 were obtained using the C3 Two-Stage SQUID chip C1c04-G25, for which parameters and bias settings are given in Table 3.1. All the measurements in Chapter 6 were taken with a C4 SQUID. The C4 generation includes an integrated on-chip Q-spoiler in the input circuit that is made up of 16 unshunted SQUIDs. A Q-spoiler, described further in Section 3.3.3, is essentially a current-limiter that is needed to protect the SQUID during application of the large NMR transmitter pulses and to minimize the measurement dead time after their removal. Parameters for the C401-L42 SQUID chip are summarized in Table 3.2.

Coupled energy sensitivity, ε_c at 1 kHz	~ 30	h
Voltage swing, ΔV	317	$\mu V/\phi_0$
Coupling constant, k	44	$\mu A/\phi_0$
Gain in FLL, G_{FLL}	280	mV/ϕ_0
Feedback resistor, R_f	10	$k\Omega$
Gain bandwidth product, GBP	0.23	GHz
Current, I	37	μA
Bias current, I_b	7.3	μA
Critical current, I_c	$\sim$ 7–9.6	μA
Voltage bias, V_b	125.78	μV
Flux bias current, ϕ_x	6	μA

Table 3.1: Summary of C1c04-G25 SQUID Parameters.

Coupled energy sensitivity, ε_c at 1 kHz	~ 50	h
Voltage swing, ΔV	211	$\mu V/\phi_0$
Coupling constant, k	42	$\mu A/\phi_0$
Gain in FLL, G_{FLL}	1.24	V/ϕ_0
Feedback resistor, R_f	30	$k\Omega$
Gain bandwidth product, GBP	1.04	GHz
Current, I	30	μA
Bias current, I_b	11.22	μA
Critical current, I_c	5.2–12.7	μA
Voltage bias, V_b	103.39	μV
Flux bias current, ϕ_x	10.54	μA

Table 3.2: Summary of C401-L42 SQUID Parameters.

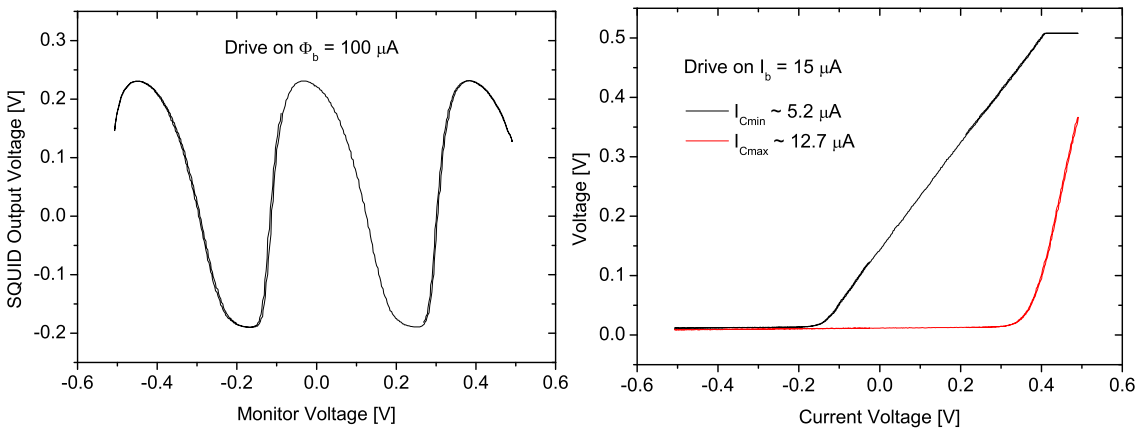

Figure 3.5: Left: $V - \phi$ characteristic for Two-stage SQUID C401-L42, open Input Coil. Right: $V - I$ curve for C401-L42, shorted input coil.

Figure 3.5 shows an example of a typical $V - \phi$ characteristic for the C4 SQUID, as well as its $V - I$ curve used to determine the maximum and minimum critical currents of the Josephson junctions. Finally, Figure 3.6 shows a comparison of the measured SQUID noise in FLL mode for each of the two SQUIDs used in this work.

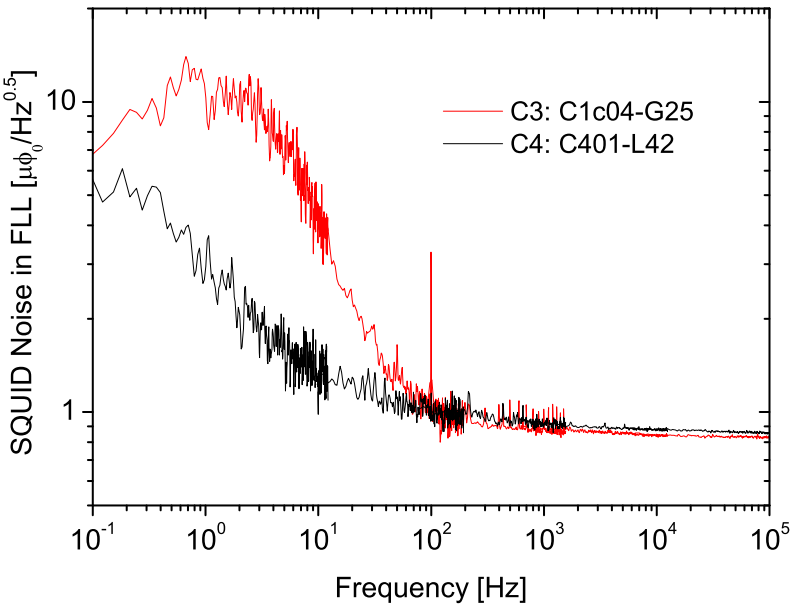

Figure 3.6: Comparison of FLL noise for C3 and C4 SQUIDs (open input coil).

3.3 NMR Coils

3.3.1 Superconducting Magnet

The magnet used to generate the static background field is a two layer superconducting solenoid wound on top of a sheet of Kapton insulation onto a copper former with a 30 mm bore. The inner diameter of the solenoid is 32 mm and the windings are 80 mm long. The wire used is copper-nickel clad niobium-titanium with a core diameter of 71 µm, a cladding and outer diameter of 81 µm and 106 µm respectively and a resistance of 5.6 Ω/m.

Superconducting Shields

The magnet is sandwiched between two superconducting niobium shields, pictured in Figure 3.7. The outer shield is a 100 mm long niobium cylinder with an inner diameter of 35 mm and a wall thickness of 1 mm and screens the magnet and sample area from any extraneous fields. The inner niobium shield, serving to screen the magnet from exposure to the transmitter pulses, is an overlapping shield as described by Hechtfischer *et al.* [47]. It is assembled from a 98 mm high and 210 mm long piece of 50 µm thick niobium foil of 99.85 % purity. A slightly larger corresponding piece of Kapton sheet is fitted to one side of the niobium before rolling the foil up and setting it with a 50:50 mixture of Stycast 2850 and 1266. The resulting shield is a cylinder with an inner diameter of 28 mm consisting of two layers of niobium plus an overlap of 20 mm. Two niobium tabs extruding from the top of the shield are used for grounding the inner shield on the magnet former when the magnet is put together. In the absence of an inner shield, the large changes in field generated by switching the prepolarizing pulse on and off, would result in eddy currents flowing in the copper magnet former that would take some time to decay. The presence of an inner shield thus reduces the dead time after the application of the prepolarizing pulse by improving the transient response of the system.

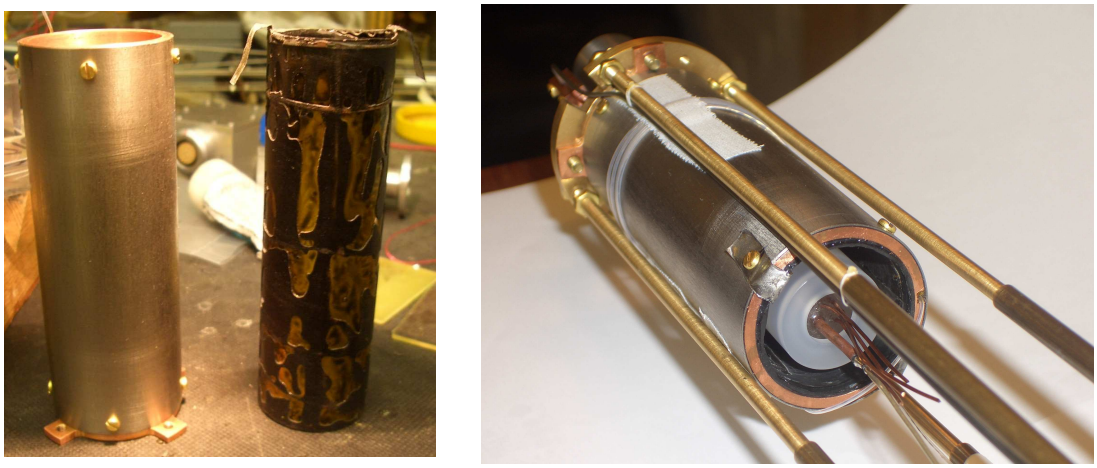

Figure 3.7: Left: Picture showing the outer and inner superconducting Nb shields; Right: Magnet assembly in situ inside probe.

Persistent Mode Operation

When performing NMR experiments, the magnet is operated in persisted mode, meaning that the current in the magnet is flowing in a closed superconducting loop, which provides a magnetic field that is temporally stable. To this end, we have a persistent switch [48] in the magnet circuit that acts as a superconducting shunt in parallel with the magnet when at 4.2 K, thus forming a closed loop with the magnet. The switch consists of copper-nickel clad niobium-titanium wire that is wound around a resistor and spotwelded onto the magnet leads. To change the current persisted in the magnet, a current is driven through the resistor to heat it enough for the superconducting shunt to go normal, allowing the magnet to form a circuit with its power supply. Once the desired current is flowing in the magnet, the current through the resistor is turned off and the shunt cools down until it goes superconducting again.

Magnet Characteristics

While persisting or depersisting the magnet, the voltage across it is monitored to ensure that the rate of change of the current does not induce a voltage so high as to quench the magnet. This also provides a convenient way of measuring the inductance of the magnet, given that $L = V\left(\frac{di}{dt}\right)^{-1}$. Using this method, the inductance of a fully assembled magnet of the type described above was measured to be $L_m \sim 4\,\mathrm{mH}$. The magnet homogeneity over the sample region can be determined according to Equation 2.14 by measuring T_2^* as a function of frequency, as done in Section 4.1.1.

Two different magnets, with dissimilar homogeneities, were used for the work presented in the subsequent chapters. The first one was the old magnet on the original probe, which was used for all the results discussed in Chapter 4 and the second one was the new magnet made for the second generation probe with which all the nanoparticle measurements in Chapter 6 were taken.

The old magnet had about 727 turns per layer and a room temperature resistance of 17.42 kΩ with a short to ground of 4.27 kΩ. Its field-current ratio was measured to be 2.727 mT/A and the homogeneity over the sample volume was approximately 800 ppm. It was later found that the homogeneity of the new magnet was significantly better than this. Upon inspecting the old magnet, it was discovered that about two thirds down the length of the solenoid, a split had formed in the windings across both layers that was about 2–3 wire thicknesses wide. Field profile calculations using a superconducting solenoid simulation program [49] showed that this split was indeed responsible for the worse homogeneity of the old magnet.

The new magnet had 730 turns per layer and a room temperature resistance of 17.36 kΩ with no short to ground. It has a field-current ratio of 2.925 mT/A and a homogeneity of about 100 ppm.

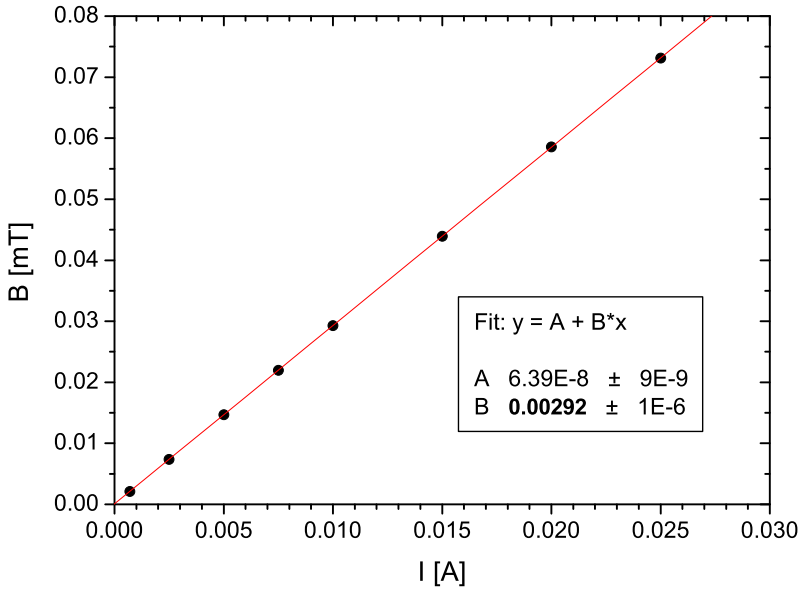

Figure 3.8: Magnetic field, as calculated from proton signal frequencies, as a function of the current in the new magnet. The linear fit gives a slope of 2.92 mT/A, which corresponds to the field-current ratio for this magnet.

The field-current ratio B/I of a given magnet with its shielding can be confirmed experimentally by measuring the frequency of the NMR signals as a function of the current in the magnet. Knowing the slope b the field-current ratio is given by

$$\frac{B}{I} = \frac{2\pi}{\gamma} b \tag{3.1}$$

Figure 3.8 shows a plot of the magnetic field versus current calibration curve for the new magnet, where the values for B have been calculated from the corresponding NMR signal frequencies, such that $B/I = b = 2.92\,\mathrm{mT/A}$.

3.3.2 Transmitter Coil

We use formers made from Kel-F rather than PTFE for both the transmitter and receiver coils, since the thermal contraction of Kel-F is better matched to that of copper, which ensures that the vertical centre of the coils stays more aligned with that of the copper magnet former at 4 K. It is also possible to bond Stycast to the Kel-F in order to set the windings of the coils. Furthermore, the vacuum cell, which fits tightly inside the receiver coil, is made from Kel-F. In order to minimize potential Johnson noise sources close to the NMR cell, the windings of the transmitter and receiver coils are made from superconducting wire instead of copper.

The transmitter coil is mostly used to generate the DC prepolarizing field B_p (refer to Section 2.3), but is also used to provide RF tipping pulses (see Section 2.2.3). Two slightly different transmitter coils were used to obtain the results presented in this thesis. Both were 30-turn saddle coils of length $l = 28\,\text{mm}$ and radius $a = 14\,\text{mm}$.

The first transmitter coil was wound from insulated bare niobium-titanium wire with a core diameter of 100 μm, an outer diameter of 127 μm and a room temperature resistance of 98 Ω/m. The total resistance at room temperature was $\sim 500\,\Omega$. It was used in the original probe to perform the measurements detailed in Section 4.1 and for all the work completed with the second generation probe. In both cases the transmitter circuit included a $R_s = 27\,\Omega$ shunt resistor in parallel with the coil. The time constant of this transmitter circuit is equal to $\tau = L/R = 3.3\,\mu\text{s}$.

The second transmitter coil was wound from copper-nickel clad niobium-titanium wire with a core diameter of 71 μm, a cladding and outer diameter of 81 μm and 106 μm respectively and a room temperature resistance of 5.6 Ω/m. The total resistance at room temperature was $\sim 28\,\Omega$. It was used in the original probe to perform the measurements detailed in Section 4.2 and was put in parallel with a shunt resistor of $R_s = 100\,\Omega$. The time constant of this transmitter circuit is $\tau = L/R = 900\,\text{ns}$.

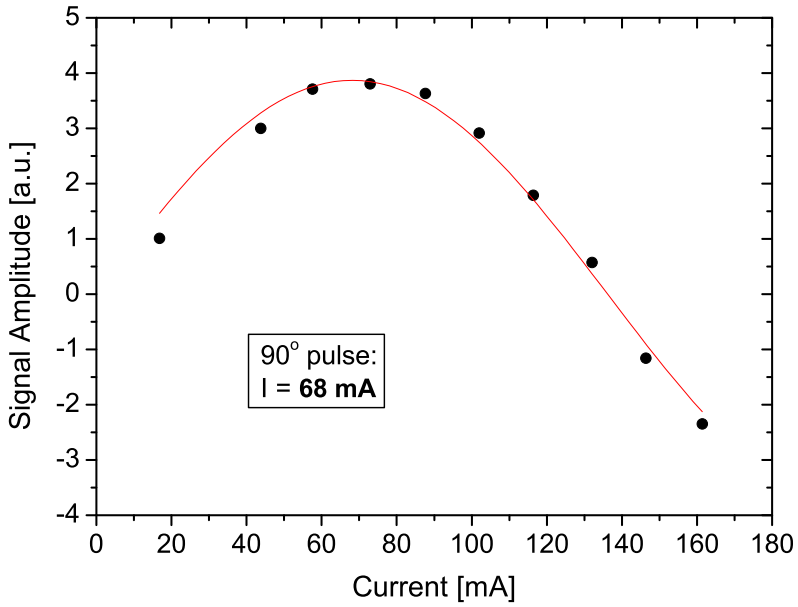

Figure 3.9: Calibration curve for 200 µs long 90° tipping pulse at 40 kHz using the bare niobium-titanium transmitter coil.

The field-current ratio of a saddle coil can be calculated using [50]:

$$\frac{B}{I} = \frac{N\sqrt{3}\mu_0}{\pi}\left(\frac{ag}{(a^2+g^2)^{3/2}} + \frac{g}{a\,(a^2+g^2)^{1/2}}\right) \tag{3.2}$$

where a is the radius and g is half of the length of the saddle coil. For a saddle coil with dimensions $a = g = 14\,\text{mm}$ this gives a field-current ratio of $B/I = 3.18\,\text{mT/A}$.

The field-current ratio of the bare niobium-titanium transmitter coil was determined from the calibration of the 200 µs long 90° RF tipping pulse used to measure T_1 at 40 and 50 kHz with conventional NMR methods. The corresponding calibration curve for this coil at a frequency of 40 kHz is shown in Figure 3.9.

A rotation of the proton spins by 90° in 200 µs corresponds to a Larmor frequency of 1250 Hz, thus requiring an RF field strength of $B_1 = 117\,\mu\text{T}$. At finite frequencies the input current is divided between the coil and the shunt resistor, $R_s = 27\,\Omega$, such that the fraction of current flowing through the transmitter coil is given by

$$\frac{I_{trans}}{I_{in}} = \sqrt{\frac{1}{1+\omega^2 L^2/R_s^2}} \tag{3.3}$$

where I_{in} is the input current, I_{trans} is the current in the transmitter coil and $L = 90\,\mu\text{H}$ is the transmitter coil inductance. At 40 kHz this gives

$$\frac{I_{trans}}{I_{in}} = \left(1 + \frac{4\pi^2(4\times10^4)^2(90\times10^{-6})^2}{(27)^2}\right)^{-1/2} = 0.767$$

and the field current ratio is therefore given by

$$\frac{B}{I} = \frac{(117\times10^{-6})}{(0.767)(68\times10^{-3})} = 2.24\,\text{mT/A}$$

3.3.3 Receiver Coil

The superconducting receiver coil is a 5-turn saddle coil of length $l = 7\,\text{mm}$ and radius $a = 7\,\text{mm}$. It is wound on a Kel-F former from insulated bare niobium-titanium wire with a core diameter of 40 µm and an outer diameter of 50 µm. Its calculated field-current ratio using Equation 3.2 is $B/I = 0.4\,\text{mT/A}$ and it has a measured inductance of $L_R = 1.05\,\mu\text{H}$.

Superconducting Flux Transformer

The flux transformer consists of the receiver coil, SQUID input coil and the Q-spoiler, connected via a superconducting twisted pair to form a closed superconducting loop, as depicted in Figure 3.3. The twisted pair is made from bare niobium-titanium wire with a 100 µm core diameter and an outer diameter of 127 µm. It is run through 1 mm inner diameter niobium tubing, for shielding against electromagnetic noise, inside PTFE sleeving filled with Apiezon N grease, to prevent the wires from vibrating.

Any flux in the receiver coil ϕ_r induces a current in the flux transformer that then induces a flux ϕ_{SQ} in the SQUID via the mutual inductance M_i between the SQUID and its input coil. The flux in the SQUID is given by

$$\phi_{SQ} = \frac{\phi_r M_i}{L_i + L_p} \tag{3.4}$$

where L_i and L_p are the inductances of the input and receiver coils respectively. Maximum flux transfer occurs if $L_i = L_p$, so the inductance of the receiver coil is matched to that of the input coil, since the input coil is integrated onto the SQUID chip (see Figure 3.4). The Q-spoiler consists of an array of hysteretic SQUIDs. If the current in the flux transformer is below the critical current of the Q-spoiler, usually $\sim 20\,\mu\text{A}$, the array behaves like a superconducting wire. If it exceeds the critical current, the Q-spoiler goes normal with a normal-state resistance of $R_N \sim 1\,\text{k}\Omega$. The Q-spoiler therefore protects the SQUID from exposure to excessively large fluxes, by reducing the current that flows in the input circuit.

3.4 Sample Cells

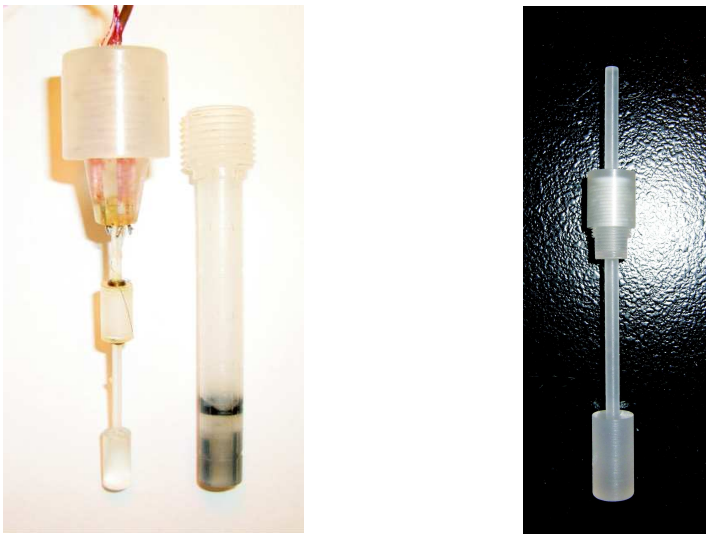

Figure 3.10: Left: Stycast sample cell connected up to the Stycast cone forming the vacuum cell seal next to the Kel-F vacuum cell; Right: Redesigned sample cell made from Kel-F.

3.4.1 Stycast Sample Cell

Figure 3.10 shows the Stycast 1266 sample cell, used for the measurements presented in Chapter 4, that is designed to fit into the Kel-F vacuum cell pictured in the same figure. It is put together from two machined Stycast pieces, a bottom stalk holding the sample cup and a top stalk with the fitting lid. These two pieces are glued together with Stycast 1266 to form an enclosed sample space, holding $\sim 150\,\mu$l, into which the sample is filled with a syringe through a small fill-hole in the lid, that is subsequently closed with another drop of Stycast. The fully assembled cell is varnished into the Stycast vacuum seal cone, as shown in Figure 3.10, that contains potted feedthroughs to which the heater and diode leads are soldered.

When immersed in the liquid helium bath, the Kel-F vacuum cell walls will be at 4 K. Taking the thermal contraction of Kel-F to be $\sim 1.2\,\%$ of its room temperature length, the 82 mm long main body of the vacuum cell will shorten by ~ 0.98 mm. A 1 mm gap between the bottom stalk and the vacuum cell, ensures that the sample holder at room temperature survives the thermal contraction of the surrounding Kel-F at 4 K.

Once the vacuum cell is sealed by means of the screw-down greased cone seal, it is evacuated using the turbo pump on a leak detector, which achieves a base pressure of 1×10^{-3} mbar. The cell is continuously pumped during the first helium transfer into the mu-metal Dewar, in order to pump away helium gas diffusing into the cell as the probe cools down. Using a leak detector allows us to monitor this diffusive leak. When the probe is cold and the helium leak rate has returned back to its base level, the vacuum line going to the cell is closed off at the top of the probe. The vacuum cell is never pumped while taking measurements.

3.4.2 Heater and Diode for Sample Temperature Control

We use a resisitive heater to heat the sample and monitor its temperature by means of a four-point measurement of the temperature-dependent voltage across a calibrated silicon diode from LakeShore [51]. The voltage across the heater is adjusted manually to achieve a given sample temperature. Once in thermal equilibrium, the temperature is stable to within a degree Kelvin over the course of a measurement. The diode is set in the bottom of the Stycast cup with more Stycast 1266, which isolates it from the sample and also seals the feedthrough hole for the platinum diode leads. The heater consists of a twisted pair of 40 µm niobium-titanium wire, with a room temperature resistance of $600\,\Omega/\mathrm{m}$, that is wound non-inductively around the top and bottom sample cell holder stalks. The length of the twisted pair is such that the resistance of the heater is $R_h \sim 1\,\mathrm{k}\Omega$ at room temperature.

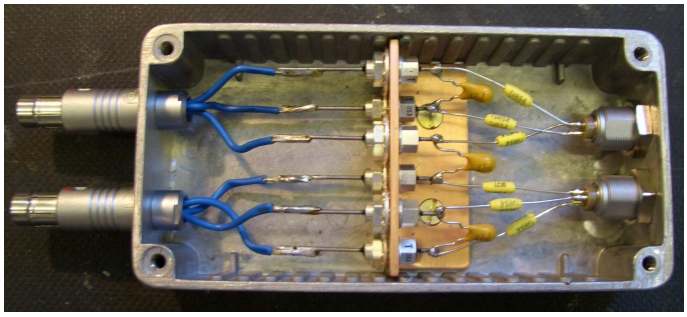

Figure 3.11: Filter-circuit for the heater and diode operation on the original spectrometer probe.

With the vacuum cell immersed in a 4 K environment, it takes a voltage of around $V_h \sim 15\,\mathrm{V}$ across the heater to keep a liquid sample at room temperature. A rough estimate of the power dissipated by the resistive heater is therefore given by

$$P = \frac{V_h^2}{R_h} = \frac{15^2}{1000} = 225\,\mathrm{mW}$$

The rate of liquid helium consumption at atmospheric pressure being 1.4 L/Wh [52], the heat leak from the vacuum cell to the liquid helium bath results in an additional boil-off of

$$(1.4\,\mathrm{L/Wh})(0.225\,\mathrm{W}) = 0.315\,\mathrm{L/h}$$

Due to the proximity of the heater and diode to the sample region, they are a potential sources of additional noise and interference, so care needs to be taken when choosing which material to use for the heater and the diode leads. After having tested heaters made from phosphor-bronze, beryllium copper and manganin, it was found that niobium-titanium wire had the least effect in terms of signal broadening. Niobium-titanium wire also has a convenient resistance, thus providing the necessary heating power with a reasonable heater length and small enough currents.

We try to minimize any interference from the heater and diode by including π-filters and low-pass LC filtering into their circuits. Figure 3.11 shows the inside of the filter box that attaches to the top of the original probe for this purpose. The cut-off frequency of the filtering circuit had to be adjusted to well below 50 Hz, see Section 6.1.2, in order to improve the stability of the nanoparticle suspensions for the measurements described in Chapter 6.

3.4.3 Kel-F Sample Cell

For the experimental work discussed in Chapter 6, the sample cell itself had to be redesigned. Figure 3.10 shows the modified sample cell made from Kel-F. The top part of the sample holder was changed into a screw-top lid that fits onto the corresponding thread on the outside of the sample cup, a design similar to the Kel-F vacuum cell seal. To fit this element into the constricting vacuum cell space, the volume of the sample cup ended up being reduced to $\sim 100\,\mu$l. The seal is made leak-tight by wrapping PTFE tape on the thread before doing it up, in addition to placing a small fitted Teflon lid on top of the Kel-F cup, that is then squeezed down onto the cup as the screw-top is tightened. Flats are machined onto the bottom of the cup below the thread, to provide better grip when tightening or undoing the seal. These flats are also used to glue a diode on externally once the cell is assembled.

The Kel-F cells constitute a big improvement over the original Stycast cells in many ways. They are generally more reuseable and diodes can easily be transferred between cups, which was not possible with the potted diodes in the Stycast cells. Also, despite having to rewind the top part of the heater each time a sample is changed, sample turn-around times are much quicker, since no preparing and curing of Stycast is involved. And most importantly, as described in Section 6.1.2, the Kel-F cells were found to improve the stability of our magnetic nanoparticle solutions in experimental conditions.

3.5 Instrumentation Development

Following the initial performance characterization work described in Chapter 4 and the acquisition of a magnetically screened enclosure, the original idea behind the second generation probe was to have an improved duplicate of the original spectrometer available, to be able to perform measurements of magnetic nanoparticle solutions and NMR spectroscopy on biological samples in parallel. Following the attempts at improving the signal-to-noise ratio of the spectrometers, as detailed in Section 3.5.2, it turned out that the planned spectroscopy experiments were not feasible with the dipper probe spectrometer set-up. The whole process nevertheless resulted in some concrete improvements that were useful when it came to taking all the measurements presented in Chapter 6.

3.5.1 Second Generation Probe

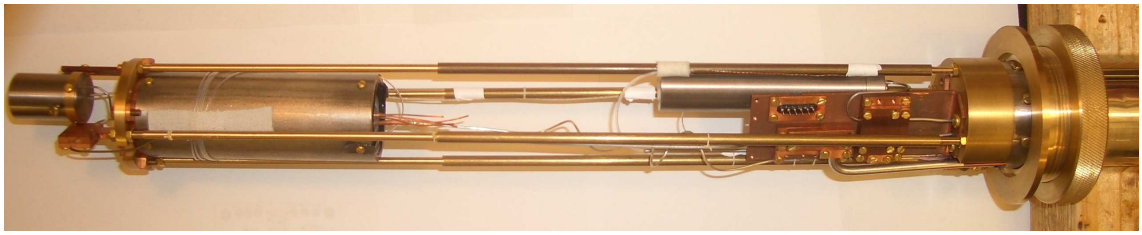

Figure 3.12: Photograph of newly assembled second generation probe, showing from left to right: shielded receiver and transmitter coil junction boxes, magnet, SQUID shield and junction box / pin connector holder bracket.

The second generation probe was built completely from scratch with all new components. Figure 3.12 shows the bottom of the newly assembled duplicate NMR spectrometer dipper probe. A summary of all the necessary room temperature to 4 K twisted pairs necessary for operating the spectrometer is given in Table 3.3.

SQUID septuplet	60 µm	Copper
Q-spoiler modulation pair	60 µm	Copper
Transmitter pair	300 µm	Copper
Heater pair	60 µm	Copper
Diode quadruplet	80 µm	Constantan
Persistent switch pair	60 µm	Copper
Magnet voltage tap pair	80 µm	Constantan
Magnet pair	300 µm	Copper
Spare pair	60 µm	Copper

Table 3.3: Summary of room temperature to 4 K wiring for second generation probe.

A major improvement made on the second generation probe was to separate the wiring for the heater and diode operation onto two separate Fisher connectors in order to allow us to operate one independently of the other. On the original probe, the four diode leads and the two heater leads were split across two 3-pin Fisher connectors, one of which is replaced on the duplicate probe with a 4-pin connector carrying all four diode leads. This is important in some instances where we pulse the heater during signal acquisition, to reduce the signal broadening effect due to additional fields created by the current flowing in the heater wire, while continuously measuring the sample temperature with the diode.

A practical improvement in terms of handling is that the total length of the probe was made shorter by virtue of a more compact top end, which makes it easier to insert the probe into the mu-metal shielded Dewar in the restricted height of the Biodiagnostics laboratory.

3.5.2 Signal-to-Noise Improvement

For some of our planned experiments, it was important to work towards improving the signal-to-noise ratio (SNR) of the SQUID spectrometer probes. A better SNR can be achieved by reducing the background noise or increasing the signal strength. We explored what could be done with our set-up in each case.

When trying to minimize the noise background, many factors need to be considered, such as ensuring adequate shielding of the sample area or removing sources of Johnson noise. One concrete step towards reducing the measured noise is the use of a 24-bit analogue-digital card [53] to capture data instead of the 12-bit card used previously. This increased our signal amplitude resolution, but also decreased the quantization noise.

But the main focus of our efforts to improve the SNR was on increasing the prepolarizing field B_p in order to boost the signal strength. The aim was to increase B_p by a factor of ten to about 20 mT. Two things had to be addressed in order to make this possible in practice: the need for a more powerful transmitter coil with a higher B/I ratio and the ability to put higher currents through the transmitter circuits of the probes.

The second point made it necessary to upgrade the wiring, connectors and junction boxes on both RT NMR probes, so that they could safely take up to 10 A in the transmitter circuit. A Techron 7792 power amplifier [54] was purchased to be used with our standard signal generators as a source for these currents. To connect the transmitter coils on the probes to the amplifier, we had to make up a suitable transmitter cable, as well as a new external transmitter box, pictured in Figure 3.13, with high power diodes to block noise from the amplifier and appropriately rated monitor resistors to measure the current in the transmitter coil. It was found that the diodes and resistors had to be properly heat-sunk for optimum noise performance.

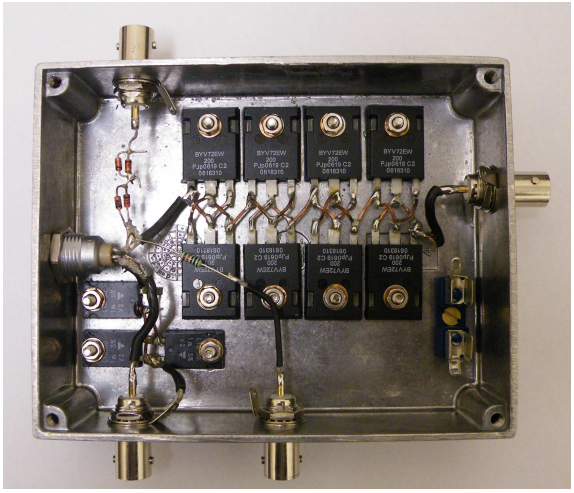

Figure 3.13: Properly heat-sunk transmitter box.

Concurrently we wound a 300-turn Helmholtz transmitter coil to obtain a significantly larger field-current ratio than for our previous 30-turn saddle coils. It was designed to be used in conjunction with an astatic receiver coil. Unfortunately after extensive testing it turned out that this transmitter coil could not be used to generate higher prepolarizing fields than previously possible, without trapping flux in the inner shield, which significantly and irreversibly increases the field inhomogeneity across the sample.

Having gone back to using our old 30-turn coil, but now with the Techron as a current source, we were faced with the same problem of flux trapping as the current in the transmitter coil was increased. We determined that the maximum current we can put through this coil, without broadening the signal noticeably, is about 1.8 A, corresponding to a prepolarizing field of $\approx 4\,\mathrm{mT}$. This is a slightly bigger field than was obtainable with the 300-turn coil, before starting to trap flux.

Even though we have only managed to increase B_p by a factor of two, this still constitutes a real improvement. Combined with the reduced noise background, our SNR ratio has increased by a factor of four, as shown in Figure 3.14. It is now generally sufficient to only take 10 averages to get a good signal, thus considerably reducing the time it takes to complete T_2^* frequency sweeps and T_1 measurements.

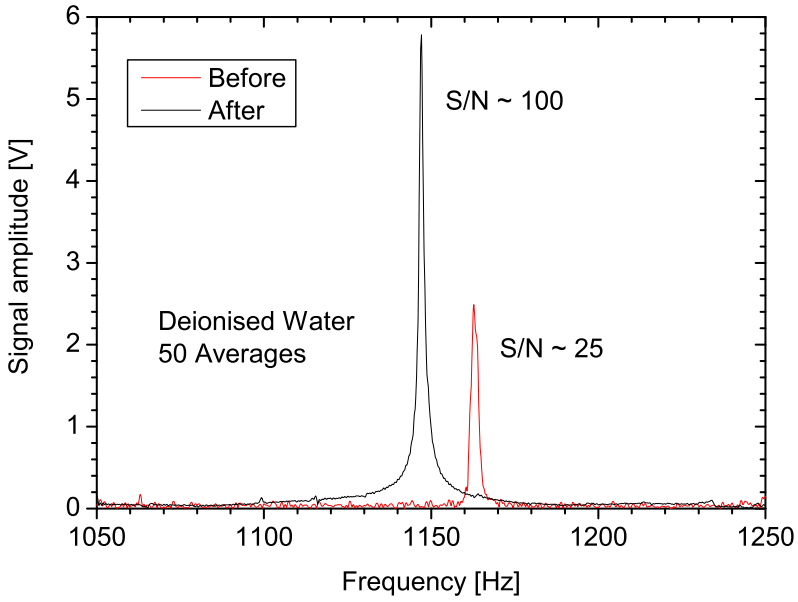

Figure 3.14: Comparison of Signal-to-noise ratio before and after the use of the Techron.

3.6 Summary

A DC SQUID spectrometer for NMR on small liquid samples at room temperature has been developed and improved upon with the building of a second generation probe. A new Two-Stage SQUID sensor has been used successfully, improving the sensitivity of the spectrometer. The sample cell was redesigned from Kel-F in a way to shorten sample turn-over times. Through changes to the experimental hardware we obtained a signal-to-noise improvement of a factor of four over the course of this work.

Chapter 4

NMR on Room Temperature Samples in Ultralow Fields

This chapter presents a number of initial measurements on simple liquid samples, whose aim was to test the performance of the DC SQUID dipper probe. These include the observation of free induction decays (FIDs) for water down to the lowest magnetic fields achievable with this probe, measurements on a machine oil sample with much shorter relaxation times and two-component signals recorded for a water and machine oil mixture. All of these measurements were presented in a paper by Köerber *et al.* [55].The chapter also describes the specialized pulse sequences required to measure the longitudinal relaxation time T_1 in low magnetic fields and presents direct low-field measurements of T_1 as a function of frequency for water at two different temperatures.

4.1 Testing of Spectrometer Performance

4.1.1 Linewidth as a Function of Field for Water Sample

The first sample studied with the C1c04-G25 Two-Stage SQUID sensor was a 0.14 ml sample of deionized water, containing 9.3×10^{21} protons. The sample was kept at a temperature of 280–300 K.

We applied a 10 s long prepolarizing pulse with $B_p = 2\,\mathrm{mT}$ to create a sample magnetization in the transverse plane where, upon removal of the pulse, the spins precessed around B_0 with a frequency ω_0 and dephased with a time constant T_2^*. We varied the current in the magnet in order to measure T_2^* as a function of Larmor frequency. The recorded FIDs were then Fourier transformed to obtain the frequency spectrum, where a Lorentzian could be fitted to the NMR signals to determine their width. Figure 4.1 shows how the signals are becoming sharper as B_0 is decreased, just as would be expected.

Figure 4.1 illustrates the frequency dependence of the NMR linewidth. From this it can be seen that the magnet inhomogeneity is not the only factor playing a role in the line broadening with field. The fact that the linewidths are different depending on the polarity of the current in the magnet, indicates that there is a residual field gradient trapped, which either adds or subtracts to the field gradient generated by the magnet, see Figure 4.2.

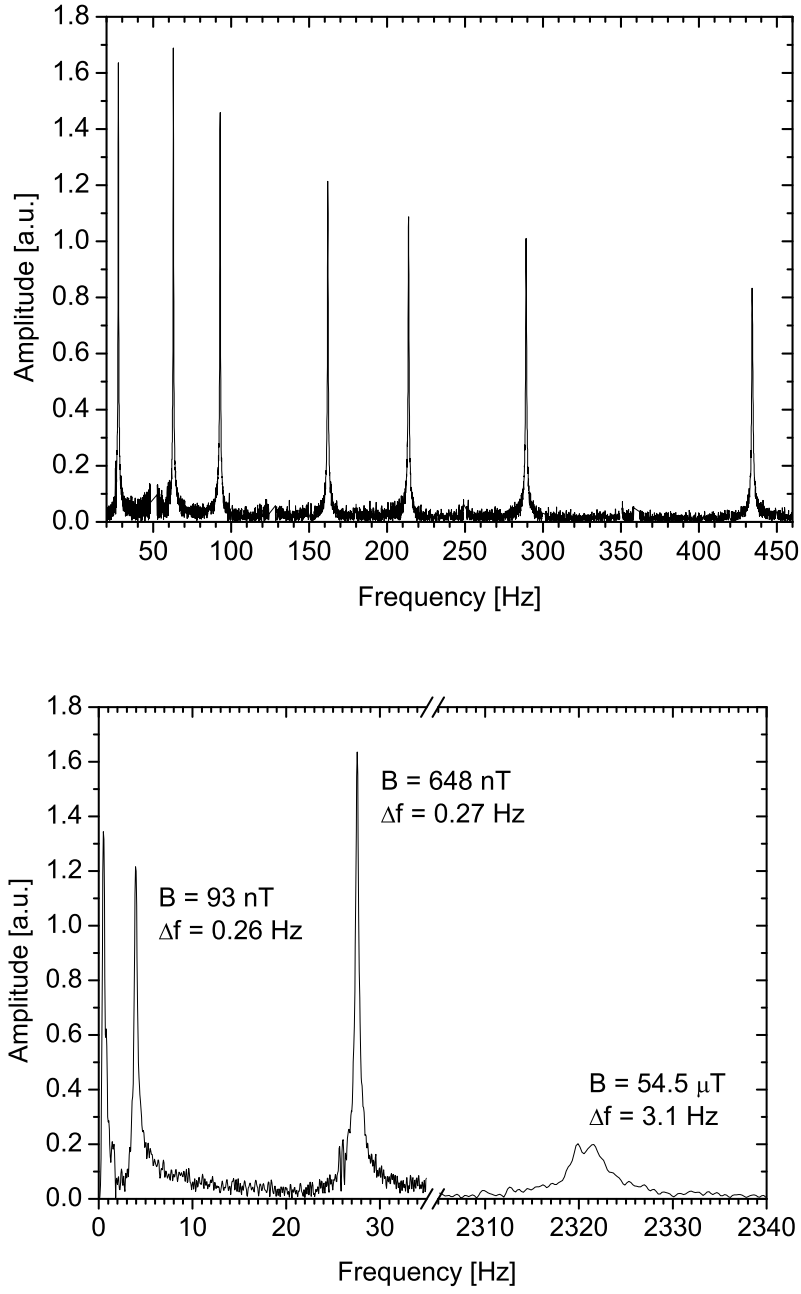

Figure 4.1: Signals from water at room temperature for a positive current in the magnet and a 10 second long prepolarizing pulse with $B_p = 2\,\mathrm{mT}$.

Determination of Residual Field Gradient

Figure 4.2 [55] shows the measured T_2^* for water as a function of the applied field. The measured linewidth $\Delta\nu = 1/\pi T_2^*$ is given by

$$\Delta\nu = \Delta\nu_{in} + |\alpha\nu + \beta| \tag{4.1}$$

where $\Delta\nu_{in} = 1/\pi T_2$ is the intrinsic linewidth.

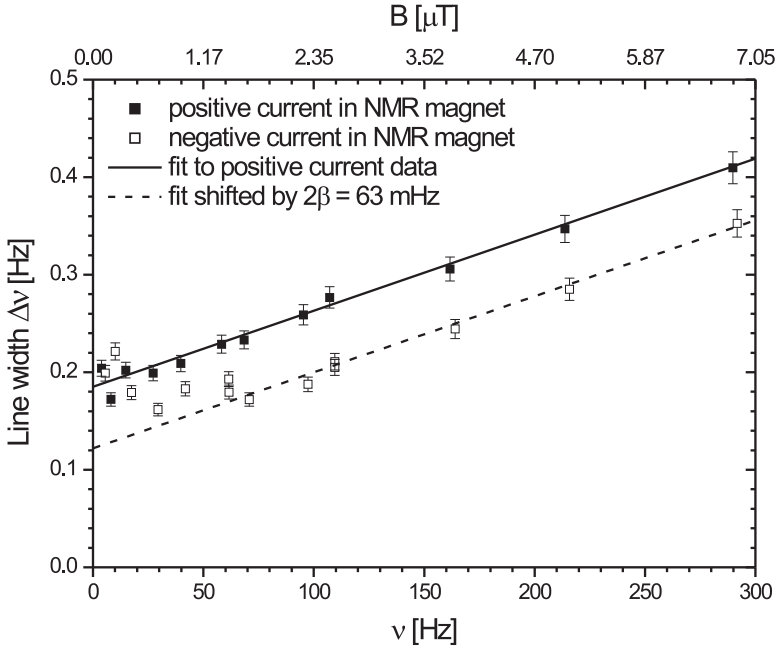

Figure 4.2: Frequency (and field) dependence of the NMR linewidth in water at 298 K [55]. The solid line is a linear fit to the positive current data. The slope is determined by the magnet inhomogeneity. A minimum linewidth of ~ 0.16 Hz is observed at a finite frequency for negative currents, where the field gradient from the magnet opposes the residual gradient.

α is the relative magnet inhomogeneity given by $\alpha = \Delta B/B_0$, where ΔB is the variation in field for a given static field strength B_0. α can be determined from the slope of the linear fit to the high frequency data (from both polarities) and from our measurements we obtain $\alpha \approx 800\,\text{ppm}$.

β is the frequency shift resulting from the environmental residual field gradient with zero current in the magnet. β can be determined from the vertical separation between the slopes of the linear fits for the two polarities. This gives a value of $\approx 31.5\,\text{mHz}$, corresponding to a residual gradient of $\approx 1\,\text{nT/cm}$, which is consistent with the measurements of the sample region inside the mu-metal shield taken with a fluxgate magnetometer in the absence of the probe (see Figure 3.2 in Section 3.1).

Furthermore, from the shift in the Larmor frequency when comparing signals in the same static field for both polarities, we can determine the residual field trapped in the superconducting shields to be $\approx 50\,\text{nT}$. Burghoff *et al.* [16] determined the linewidth for a 20 ml pure water sample in zero field to be $\approx 0.16\,\text{Hz}$. Because the residual field in the Berlin Magnetically Shielded Room, BMSR, is close to 0, the linewidth they obtain in zero field is approximately intrinsic.

In our case, because we have $\beta \neq 0$, α and β will cancel each other out more or less completely at a finite static field (for one of the two polarities), such that the linewidth at that field will approximately correspond to the intrinsic value. Our narrowest linewidth, 0.16 Hz, is consistent with the zero field data obtained by Burghoff *et al.* and corresponds to a T_2 of 2 seconds. In this frequency region (50 Hz) our SNR was ≈ 5 in a single shot. Our low field data is also consistent with low field T_1 measurements made by Graf *et al.* [56].

4.1.2 Machine Oil Samples

Pure Machine Oil

To demonstrate the suitability of our RT NMR spectrometer for looking at samples with much shorter relaxation times than those of water, we studied a sample of Vitrea 33 machine oil [57], containing 3.6×10^{21} protons, at a temperature of 300 K. Two signals for this sample are shown in Figure 4.3 at a Larmor frequency of 5 kHz, for both current polarities in the magnet.

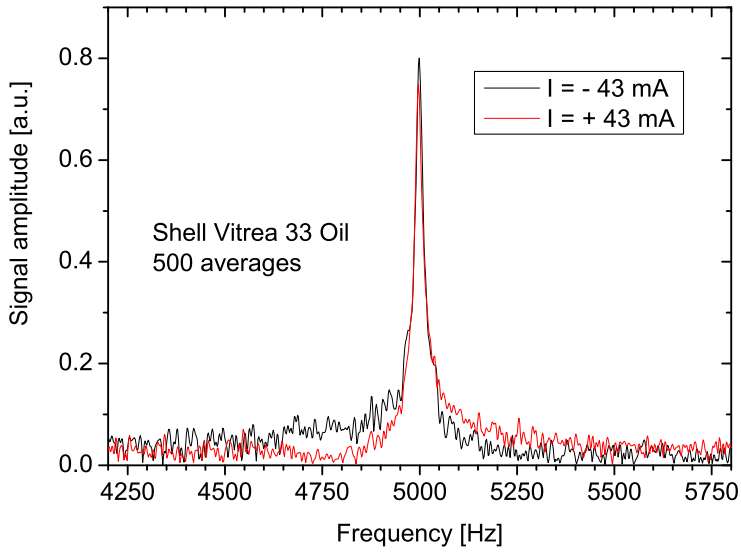

Figure 4.3: Oil signal at 5 kHz, showing the signal dependence on the current polarity.

Figure 4.4 shows our data for T_1 in the 2 mT prepolarizing field, with signals read-out at a Larmor frequency of 5 kHz (117 μT). Details on the procedure for measuring T_1 in the prepolarizing field are given in Section 2.3.2. Fitting to the data gives $T_1 = 27.3 \pm 0.3$ ms. The fit is not very good, since it does not account for a small component of the signal with a longer T_1, which could be the result of a slight water contamination. Therefore, this measurement also gives an indication of the ability of the spectrometer to detect small amounts of water contamination in oil samples.

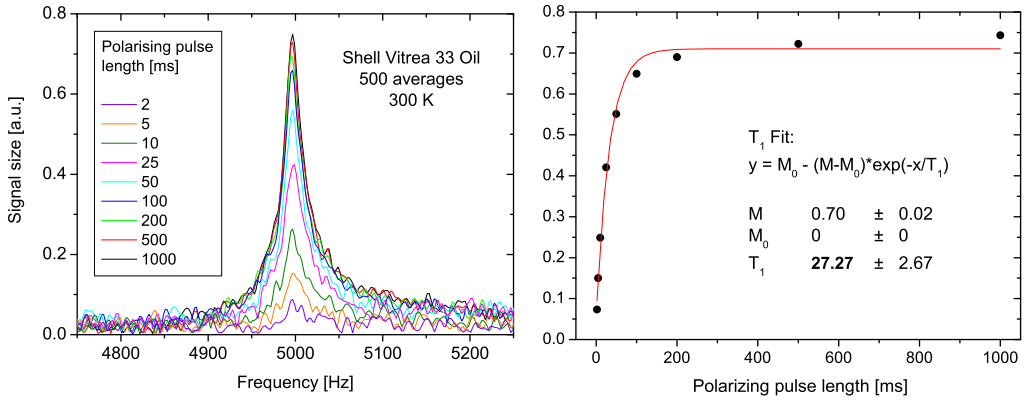

Figure 4.4: T_1 of machine oil in 2 mT prepolarizing field.

We determined the intrinsic T_2 of the machine oil sample by measuring the T_2^* frequency dependence, shown in Figure 4.5, from which we extrapolated the zero-field value. We obtained an intrinsic T_2 of 27.00 ± 0.66 ms. Thus our measurements confirm that for the machine oil we have $T_1 = T_2$ in the low-field limit. We also investigated the viscosity dependence of T_2^* [58], which is shown in Figure 4.6 [55]. We found that T_2^* decreased linearly with increasing viscosity, which is inversely proportional to the temperature of the oil. When the sample temperature was lowered to as far as 277 K, the signal was completely lost in the noise.

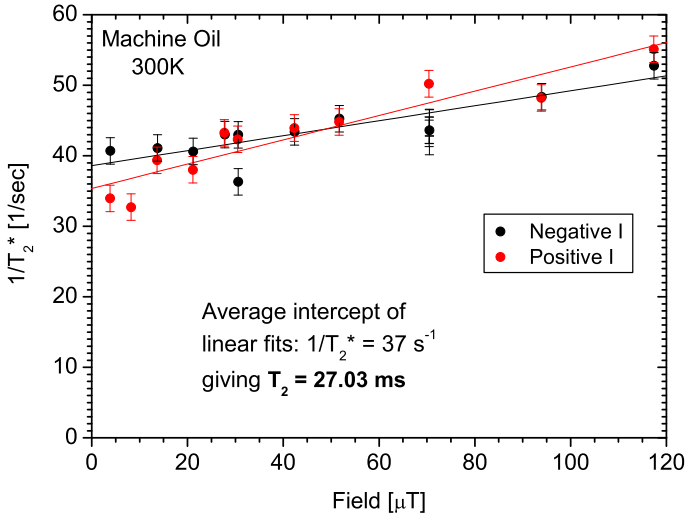

Figure 4.5: Frequency dependence of machine oil transverse relaxation rate.

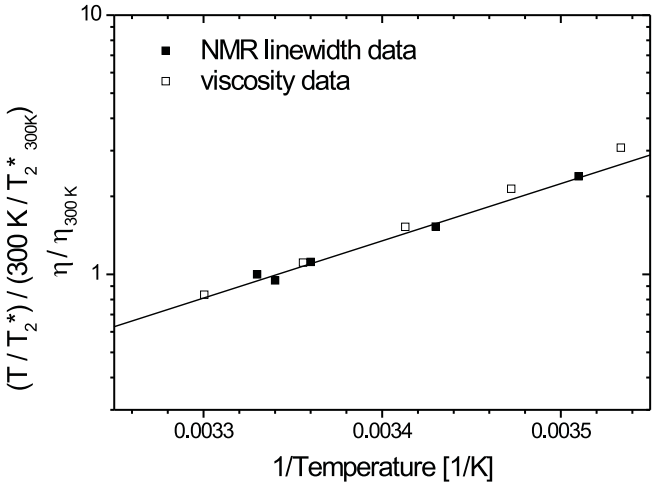

Figure 4.6: Temperature dependence of NMR linewidth and viscosity in Vitrea 33 machine oil normalized to 300 K values [55].

Oil-Water Mixture - 4:1 Ratio

The next step was to study a two-component NMR signal. After having failed to clearly observe the oil component in the NMR signals from a 1:4 oil-water mixture, we tried again with a sample that had a ratio of 4:1 oil to water. The effect of the oil on the NMR signal is manifested in broader flanks in the frequency domain and a quickly decaying component in the FID. To show this, we reduced the temperature of the mixture to 275 K, *i.e.* just above the freezing temperature of the water, where the oil is so viscous that its T_2^* is too short to be measurable, so that we see no signal from the oil. As can be seen in Figure 4.7, the disappearance of the oil component changes the NMR signal measurably. To obtain good quality signals we had to take 500 averages. The pulse sequence used in this case was just over 12 seconds long, such that the total measurement time was about 100 minutes. Furthermore, to get the cleanest possible FID, we initially Fourier transformed the time domain signal and then applied a Gaussian filter in the frequency domain, before transforming the resulting signal back to the time domain.

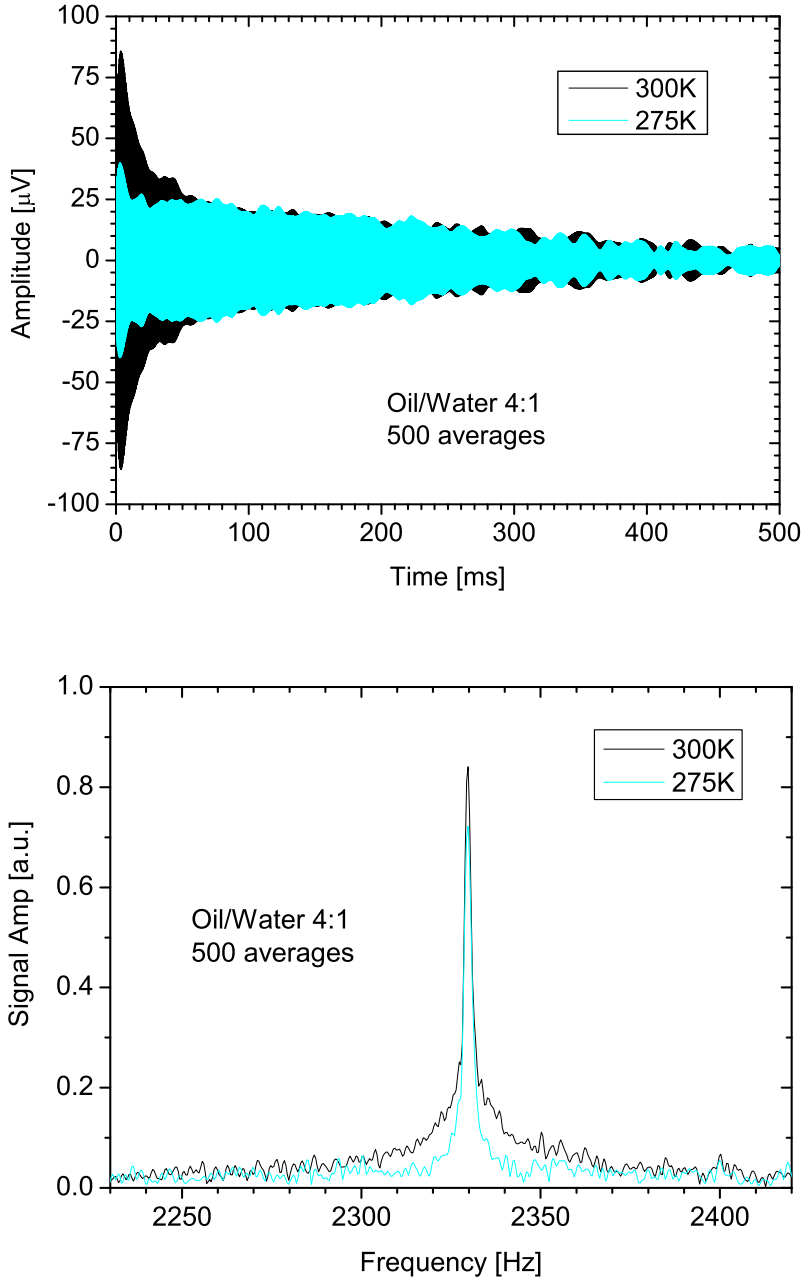

Figure 4.7: Oil-water mixture NMR signals at two temperatures. Top: Time domain signal was background subtracted and Fourier transformed. Gaussian filter (width 100Hz) applied to NMR signal in frequency domain. Data was then inverse FT back into the time domain. Bottom: Frequency domain signals.

4.2 T_1 as a Function of Frequency in Water

4.2.1 Techniques for Measuring T_1 in Low Fields

We measured seven T_1s of the deionized water sample at a temperature of 295–296 K, for Larmor frequencies ranging from 19.5 Hz to 158 kHz. To achieve this we used four different methods, depending on the strength of the field in which the spin-lattice relaxation was taking place in. As illustrated in Figure 4.8, our measurement range therefore subdivides into four field regimes: high (on the order of a few mT), intermediate (1×10^{-4} to 1×10^{-3} T), low (1×10^{-5} to 1×10^{-4} T) and ultralow (<10 μT) fields. In the intermediate to high field regimes, labelled 3 and 4 in Figure 4.8, we use the RF sequences described in Section 2.2.3 and the prepolarizing field method outlined in Section 2.3.2 respectively. At lower fields, *i.e.* regimes 1 and 2 in Figure 4.8, we start off with a non-equilibrium magnetization along B_0 and then measure the magnitude of the magnetization after allowing it to undergo longitudinal relaxation for a variable time τ. For the deionized water sample we took measurements with τ ranging from 200 ms to 15 s and depending on which of the four methods was used, exponential decay or hyperbolic tangent curves were then fitted to the data to determine T_1.

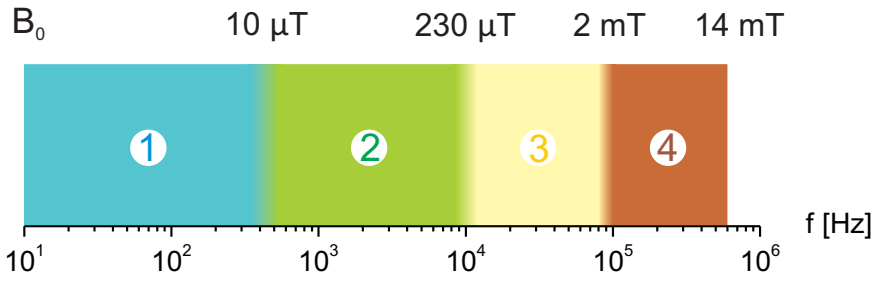

Figure 4.8: Frequency ranges for the different T_1 techniques. 1 – Ultralow field regime: 1/4 turn pulse sequence; 2 – Low field regime: Adiabatic turn-off of B_p; 3 – Intermediate field regime: RF measurement; 4 – High field regime: Prepolarizing field technique.

High to Intermediate Field Regime

For the highest fields, we measure T_1 in the prepolarizing field B_p, which is on the order of a few mT. The highest prepolarizing field available to us was $B_p = 3.7\,\mathrm{mT}$, corresponding to a proton Larmor frequency of 158 kHz. Higher prepolarizing pulses were achievable, but resulted in significant signal broadening due to flux trapping in the inner overlapping niobium shield. Nevertheless at the end of an experimental run before warming up the probe, we sometimes conducted measurements at frequencies up to about 600 kHz, corresponding to $B_p = 14\,\mathrm{mT}$. Figure 4.9 shows the fit to the T_1 data in the prepolarizing field of $B_p = 3.7\,\mathrm{mT}$.

At intermediate fields we can apply traditional RF tipping methods. We used the two different pulse sequences described in Section 2.2.3 to measure T_1 in a static field of 50 kHz ($\sim 1.2\,\mathrm{mT}$).

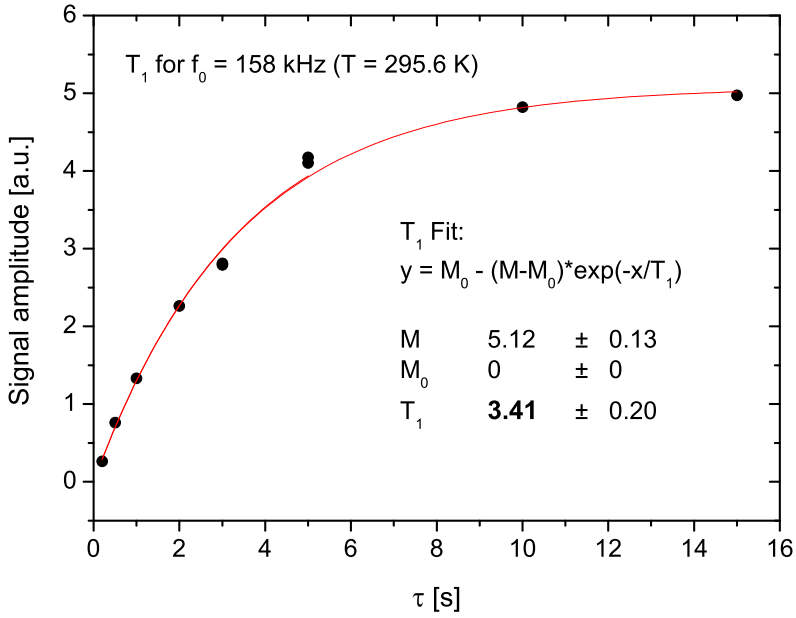

Figure 4.9: T_1 of deionized water in a prepolarizing field of $B_p = 3.7\,\mathrm{mT}$.

Low Field Regime

As we go down in field, the magnetization of the sample decreases proportionally and signal sizes become too small for accurate T_1 measurements. Consequently we need to increase the magnetization in the longitudinal direction, similar to the way that we use the prepolarizing pulse to increase the magnetization in the transverse plane for our T_2^* measurements.

This can be achieved by turning the transverse polarizing field B_p off adiabatically, *i.e.* slow enough for the magnetization generated by it to be largely transferred into the direction of the static field, as the effective field the sample sees (*i.e.*, which is equal to the sum of the prepolarizing and static field vectors, rotates from the transverse plane into the z-direction. The magnetization along z will then decrease back to its B_0 equilibrium value with a timescale T_1 and can be read out after a time τ by tipping it back into the transverse plane, using a broadband square DC tipping pulse, as demonstrated by Friedman *et al.* [3]. This tipping pulse is calibrated to produce a static field in the transverse plane that is equal to B_0, so that the effective field the sample sees is at an angle of 45° to the transverse plane and has a magnitude of $\sqrt{2}B_0$. The sample magnetization will precess around this effective field with the Larmor frequency of that field. The DC pulse length needs to be such that the magnetization will rotate by 180° from the z-direction into the transverse plane, *i.e.* half the Larmor period. An overview of the entire sequence is shown in Figure 4.10 (a).

The requirements for adiabatic turn-off given the relative fields of B_0 and B_p are given by Melton *et al.* [59] as:

$$\frac{dB_p}{dt} \ll \gamma B_0^2 \tag{4.2}$$

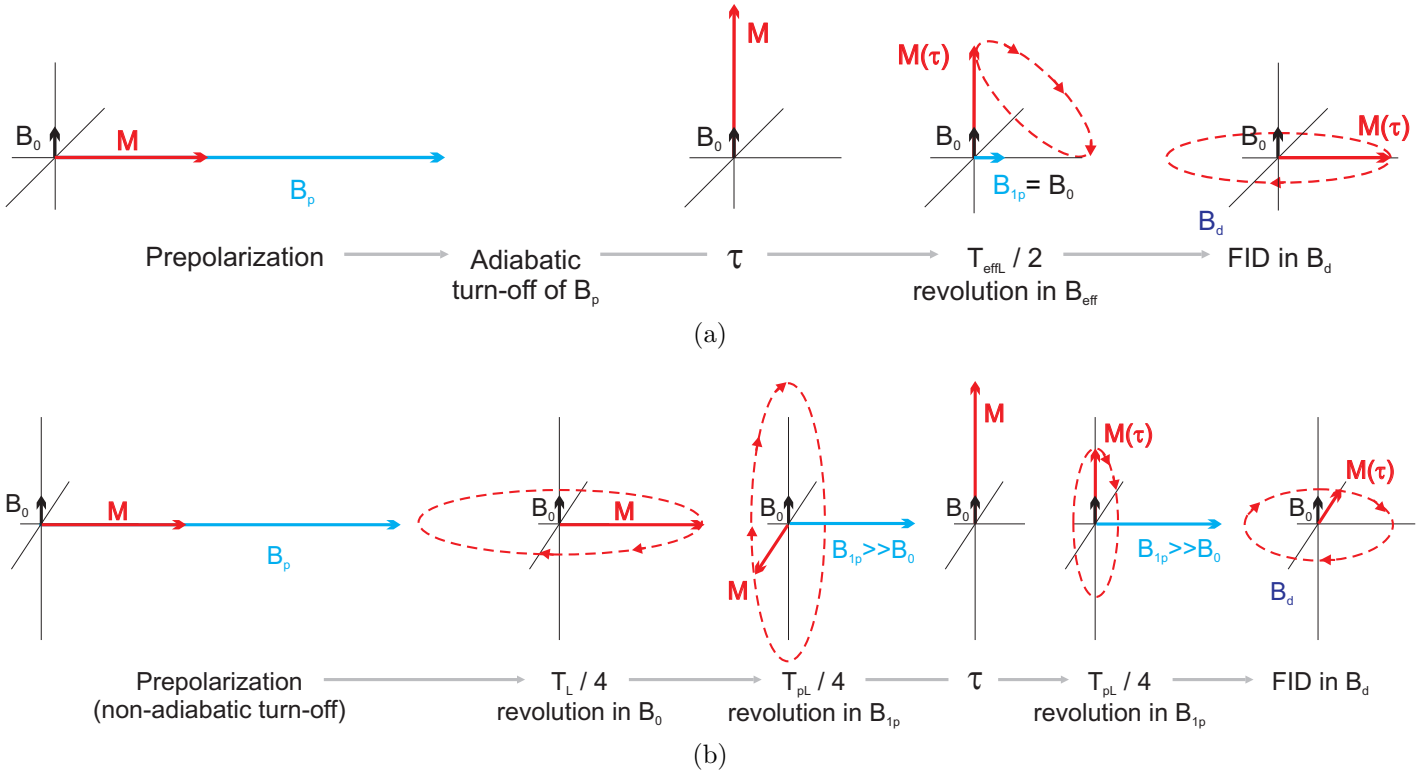

Figure 4.10: Measurement sequences for T_1 (a) at low fields using adiabatic turn-off and (b) at ultralow fields.

Their paper also demonstrates that the prepolarizing pulse can be reduced initially non-adiabatically to about $5B_0$ before an adiabatic removal is necessary to transfer the magnetization. The advantage of an initial fast turn-off to $5B_0$ is that ramp times will be greatly reduced. This is important as you go to lower fields, since as B_0 becomes smaller, the times over which a given prepolarizing field will need to be ramped down become longer and longer, up to a point where the ramp times become comparable with T_1. We used both adiabatic turn-off methods to measure T_1 in a static field of 2315 Hz.

For the simple adiabatic turn-off method, we used a 10 second long prepolarizing pulse $B_p = 3.7\,\mathrm{mT}$, which we ramped down linearly to 0 over 100 ms. After waiting a time τ while the magnetization in z decays, we applied the DC tipping pulse (90°) to read out the signal in the transverse plane. Figure 4.11 shows a comparison of the signals obtained with a normal 10 second long prepolarizing pulse and with an adiabatically ramped version of the same pulse.

It is a successful demonstration of an adiabatically turned off prepolarizing pulse, since no magnetization is left in the transverse plane at the end of the pulse. This was not a straightforward achievement, because initially we were always left with some residual signal in the measurement plane, until we realized that this was due to the time resolution of the ramp being insufficient, resulting in a not entirely linear and therefore slightly non-adiabatic ramp. This issue was resolved by generating the prepolarizing pulse as a composite pulse using two programmable signal generators.

The fast drop-off method was essentially the same as the linear ramp method, except that the prepolarizing field was reduced to $5B_0$ non-adiabatically first and the remaining field was then ramped down linearly to 0 over 7 ms. The actual pulse sequences for both methods are shown in Figure 4.14 in the next section.

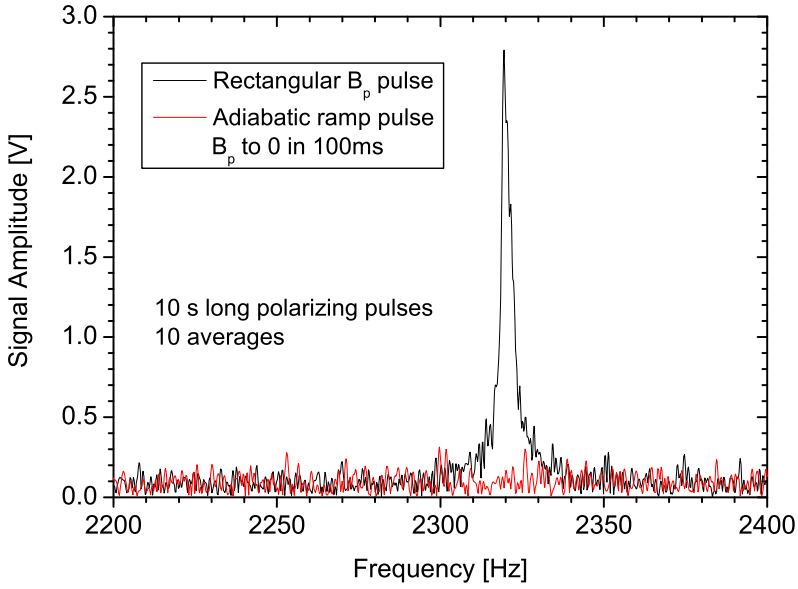

Figure 4.11: Transverse signals recorded immediately after the sudden turn-off and the adiabatic turn-off of prepolarizing pulses.

Ultralow Field Regime

At ultralow fields, the timescales over which B_p needs to be ramped down in order to guarantee adiabatic passage become too long, such that we need to use a more complicated technique to transfer the transversely polarized magnetization into the z-direction, as described below and depicted in Figure 4.10 (b).

Upon removing the prepolarizing pulse non-adiabatically, the magnetization will start to precess around B_0. After waiting for a time t_x, which is the time it will take the magnetization to precess by a 1/4 revolution, as calculated from the Larmor frequency for B_0, it will be pointing in x. At that moment we apply a DC tipping/polarizing pulse in the transverse plane that is large compared with B_0 and around which the magnetization along x will then start to precess with a Larmor frequency given by the field strength of the DC pulse B_{1p}.

Here we used the same square pulse as for the adiabatic methods for which $B_{1p} = 54\,\mu\text{T}$, corresponding to $f_{1p} = 2315\,\text{Hz}$, such that $t_z = 108\,\mu\text{s}$ for a 1/4 revolution. After applying B_{1p} for a time t_z, the magnetization will have precessed

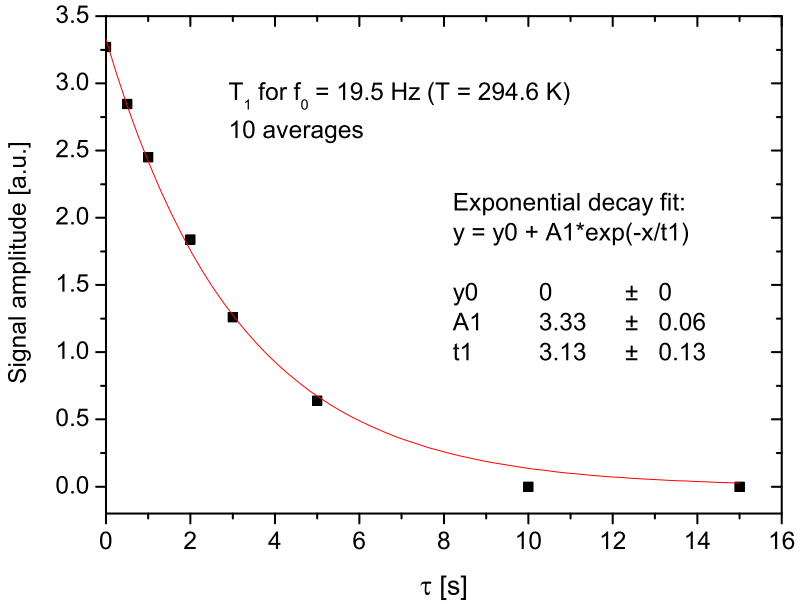

Figure 4.12: T_1 of deionized water at $f_0 = 19.5\,\mathrm{Hz}$ or $B_0 \sim 460\,\mathrm{nT}$.

by a 1/4 revolution in the z-direction. We then let it relax back to the B_0 equilibrium value for a time τ, before using the B_{1p} pulse in the same way again to tip it back into the transverse plane $(-x)$ for read-out.

We successfully used this method at two different static fields: $B_0 \sim 1.7\,\mu\mathrm{T}$, where $f_0 = 72\,\mathrm{Hz}$ ($t_x = 3.479\,\mathrm{ms}$) and $B_0 \sim 460\,\mathrm{nT}$, where $f_0 = 19.5\,\mathrm{Hz}$ ($t_x = 12.867\,\mathrm{ms}$). The 19.5 Hz data and T_1 fit are shown in Figure 4.12 and the corresponding pulse sequence is given as number 4 in Figure 4.14 in the next section.

4.2.2 Summary of T_1 Measurements

Figure 4.13 shows all our T_1 data for the deionized water sample and Figure 4.14 gives a summary of the pulse sequences for the four different methods used to obtain this data. Contrary to the results presented by Graf *et al.* [56], we found that for all our measurements T_1 was independent of frequency. For our temperature range of 295–296 K, T_1 was observed to be between $3.03 \pm 0.20\,\mathrm{s}$ (50 kHz) and $3.41 \pm 0.20\,\mathrm{s}$ (158 kHz).

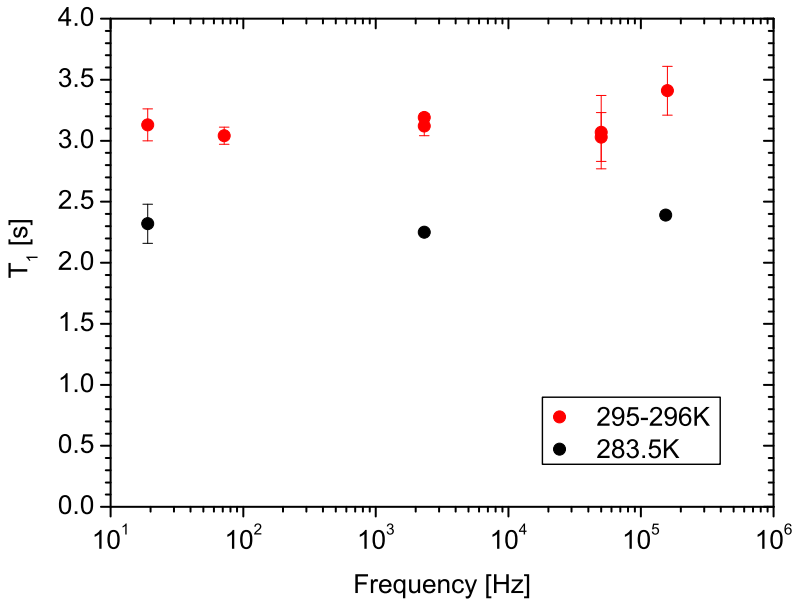

Figure 4.13: T_1 of deionized water as a function of frequency for two temperatures.

Three more measurements at some of the above fields were taken with the sample at lower temperature (283.5 K). T_1 was determined to be around 2.3–2.4 s, which is consistent with previous data.

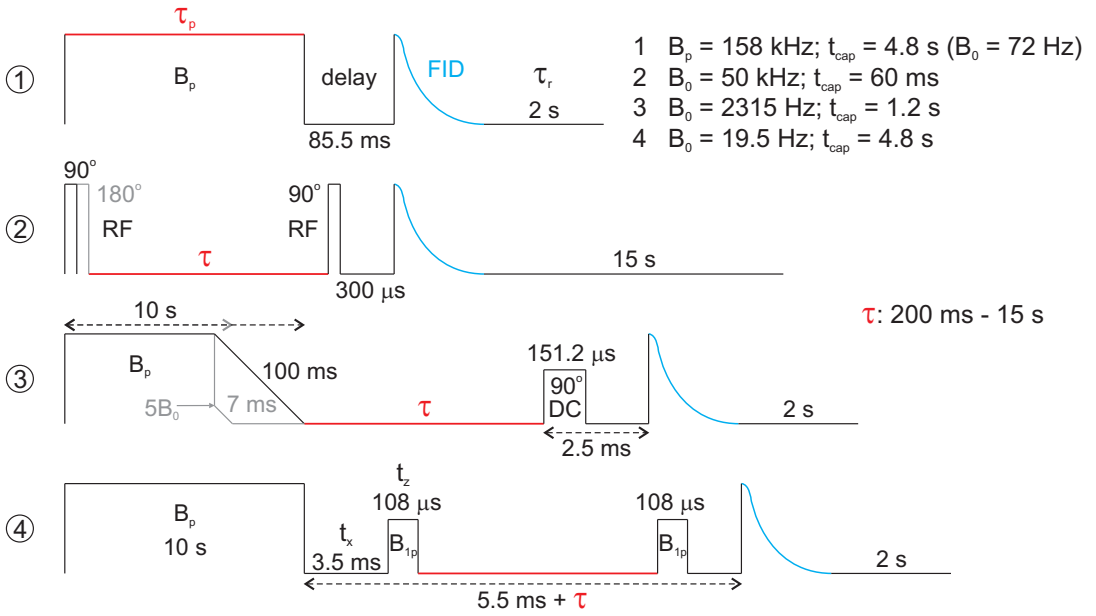

Figure 4.14: Summary of pulse sequences for T_1 measurements in deionized water.

4.3 Summary

The results discussed in the first section of Chapter 4 were presented in an APL paper published in 2007 [55]. They demonstrate the capability of the DC SQUID spectrometer probe for measuring both longitudinal and transverse relaxation times in ultra-low magnetic fields and give a measure of the magnetic environment across the sample region due to the magnetic inhomogeneity and residual field gradients. The sharpest linewidth of a water sample observable with this set-up was measured to be about 0.16 Hz, which corresponds to the linewidth measured for this sample in the best possible zero-field environment. Two-component signals and oil viscosity as a function of temperature were investigated. The first direct measurements of T_1 as a function of frequency for water in low magnetic fields showed T_1 to be largely independent of frequency below 1 MHz.

Chapter 5

Proton Relaxation in Magnetic Nanoparticle Solutions

In recent years magnetic nanoparticles have found numerous biomedical applications, a number of which are described in a review article by Pankhurst *et al.* [60]. Of interest to our research is their use as contrast agents in Magnetic Resonance Imaging (MRI) as described in numerous publications, see for example Wang *et al.* [61] and Sun *et al.* [62]. Superparamagnetic nanoparticles affect the relaxation times of surrounding protons in two ways. Their large magnetic moments introduce additional local magnetic fields that give rise to a shortened spin-spin relaxation time T_2. At the same time the relaxation behaviour of the moments, due to either Néel or Brownian relaxation, together with the diffusion of the protons past the particles, result in fluctuating local fields that can also shorten the spin-lattice relaxation time T_1, if a component of these fluctuations is at the Larmor frequency of the protons.

The first section in this chapter gives the necessary background on magnetic nanoparticle solutions, while in the following sections some theoretical aspects of proton relaxation in the presence of superparamagnetic nanoparticles are discussed, leading to a theoretical model which is then used to fit to some of the data presented in Chapter 6.

5.1 Physical Properties of Magnetic Nanoparticle Solutions

Methods of synthesizing different types of nanoparticles are reviewed by Gupta and Gupta [63] and by Tartaj *et al.* [64]. For in vivo use, magnetic nanoparticles need to be coated with a biocompatible polymer to prevent the formation of large aggregates and biodegradation when exposed to a biological system. Such a coating is also necessary in our case to keep the nanoparticles stably dispersed in aqueous solution [64]. The composition of magnetic nanoparticles can be either single-core or multi-core, but only single-core magnetic nanoparticles are used here.

The effect that different types of coated superparamagnetic nanoparticles will have on the relaxation times of the protons diffusing around them is dependent on the mechanism by which the particles relax, on their core size and hydrodynamic diameter and also on the type and thickness of their coating.

There are various different experimental techniques available to characterize ferrofluids, such as Tunneling Electron Microscopy (TEM) and Scanning Electron Microscopy (SEM) analysis [65], Magnetometry [66], Photon Correlation Spectroscopy [67], Mössbauer Spectroscopy [68], X-ray diffraction [65], Small-Angle Neutron Scattering (SANS) and AC-Susceptometry [69, 70]. A comparison of results obtained for some of these techniques for a given sample is given in Ludwig *et al.* [71].

Our samples were characterized externally by project partner Imego [72] by means of Photon Correlation Spectroscopy (PCS), Vibrating Sample Magnetometry (VSM), as well as AC susceptibility measurements, providing us with a measure of the magnetic moments of the nanoparticles and giving us an indication as to their core size and hydrodynamic diameter distributions.

5.1.1 Superparamagnetism

Superparamagnetism has been described by Bean and Livingston [73] and by Dormann [74]. Ferromagnetic particles below a critical diameter d_c have a single magnetic domain, since the formation of domain walls becomes energetically unfavourable [75]. All the spins within such a particle will therefore align along an easy axis that is determined by the crystalline structure, thus making the particle act like a very large single spin.

A static magnetization hysteresis curve for a liquid containing a collection of such particles looks like that of a paramagnetic substance, showing no remanence or coercivity, as illustrated in Figure 5.1. But it has a much larger magnetization for a given applied field with an initial susceptibility that can reach values of $\chi \sim 1$ and higher [76], which is orders of magnitude higher than for ordinary molecular paramagnetic liquids, hence the name *super*paramagnetic.

Superparamagnetic nanoparticles in a magnetic field relax via two different mechanisms: Néel and Brownian relaxation [77]. Néel relaxation is caused by reorientation of the magnetization vector inside the nanoparticle, when the thermal energy is sufficient to overcome the magnetic anisotropy energy barrier. The time constant of this process is given by [78]

$$\tau_N = \tau_0 \exp\left(\frac{\Delta E}{kT}\right) \tag{5.1}$$

where the energy barrier $\Delta E = KV$ is proportional to the volume of the magnetic particle V and an anisotropy constant K accounting for the magnetic anisotropy within the particle. The material characteristic attempt time τ_0 is usually taken to be a constant on the order of $\tau_0 = 1 \times 10^{-13}$–$1 \times 10^{-9}$ s, but the actual expression for τ_0 is also dependent on V and K [74]. An applied field and magnetic interactions will modify the energy barrier, affecting τ_N in a complex manner [79].

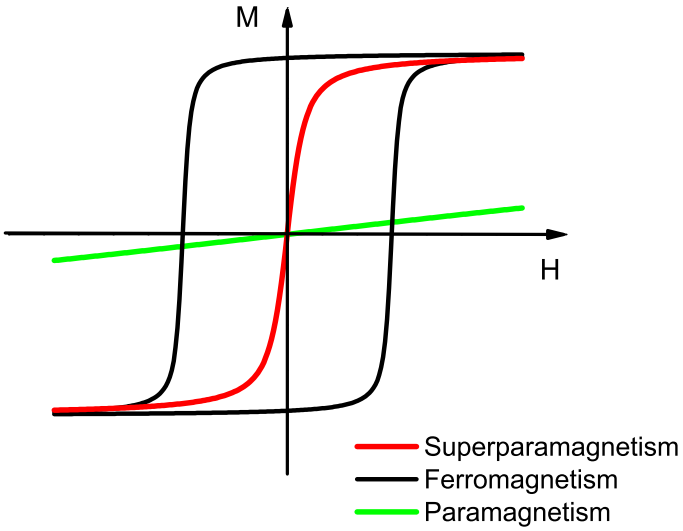

Figure 5.1: Magnetization behaviour of different materials.

Magnetic anisotropy describes the direction dependence of the anisotropy energy of the total moment μ within a single-domain magnetic nanoparticle. The most important source of magnetic anisotropy in magnetic nanoparticles is the magnetocrystalline anisotropy due to the dependence of the spin-orbit coupling on the crystallographic structure. Other relevant sources can be shape anisotropy if the nanoparticle is non-spherical, as well as surface anisotropy due to atomic spins at a surface having different symmetries to those in bulk. The directions of internal magnetization in zero field with the lowest anisotropy energy are called easy axes. For a uniaxial particle there is only one easy axis, with two directions equally likely. In this case, the anisotropy energy E_A depends on the angle α between the magnetization and the easy axis according to

$$E_A = -KV \cos^2 \alpha \tag{5.2}$$

Brownian relaxation is caused by the spin reorienting through rotational diffusion of the nanoparticle in the carrier liquid with a time constant τ_B. Assuming that hydrodynamic and dipole-dipole interactions between the particles are negligible, which will be the case for sufficiently low nanoparticle concentrations in solution, τ_B is given by

$$\tau_B = \frac{3V_H\eta}{kT} \tag{5.3}$$

where V_H is the hydrodynamic volume of the particle and η is the dynamic viscosity of the carrier liquid. The effective relaxation time constant τ_{eff} is given by

$$\frac{1}{\tau_{eff}} = \frac{1}{\tau_N} + \frac{1}{\tau_B} \tag{5.4}$$

where τ_N and τ_B are the Néel and Brownian relaxation times respectively. Due to the exponential term in the expression for τ_N, Néel relaxation will be the dominant mechanism for particles with a core below $\sim$ 10–15 nm in diameter [77]. Figure 5.2 shows both Néel and Brownian relaxation times as a function of particle diameter for a given set of particle parameters.

Whether superparamagnetic behaviour is observed depends on the measurement time τ_m of the experimental technique used. A particle is said to be thermally blocked if its thermal energy is insufficient to overcome the magnetic anisotropy energy barrier. Consequently, if $\tau_{eff} \gg \tau_m$ and the nanoparticle moment remains confined in one energy minimum during the measurement time, then the particle appears thermally blocked. The blocking volume V_b is the required magnetic core volume for a nanoparticle to appear thermally blocked and is given by

$$V_b = \frac{kT \ln(\tau_m/\tau_0)}{K} \tag{5.5}$$

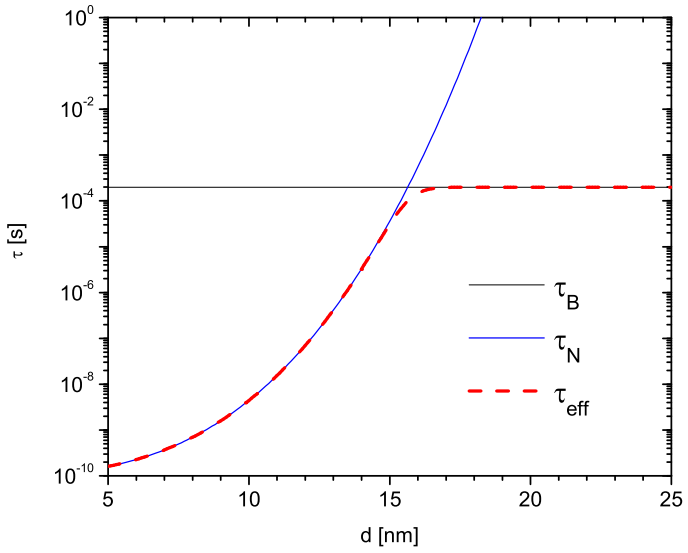

Figure 5.2: τ_N, τ_B and τ_{eff} for a magnetite nanoparticle with core diameter d and a hydrodynamic diameter of 65 nm, assuming the following parameters: anisotropy constant $K = 3 \times 10^4\,\mathrm{J/m^3}$ [80], viscosity of water $\eta = 0.001\,\mathrm{Pa\,s}$ and attempt time $\tau_0 = 1 \times 10^{-10}\,\mathrm{s}$.

5.1.2 Magnetization Behaviour of Magnetic Nanoparticles in Solution

To describe the equilibrium magnetic properties of a collection of magnetic nanoparticles in solution, we assume each particle to have a moment $\boldsymbol{\mu}$ that fluctuates in time, but whose magnitude μ remains fixed [76]. Whether $\boldsymbol{\mu}$ fluctuates as a result of Brownian or Néel relaxation, does not influence the equilibrium magnetic properties of the ferrofluid, but only its dynamics.

The magnetization behaviour of non-interacting single-domain magnetic nanoparticles in the superparamagnetic regime is described by the dipole-field interaction energy [81]

$$E_B = -\boldsymbol{\mu} \cdot \mathbf{B} \tag{5.6}$$

which yields the Langevin model, such that for a collection of N nanoparticles, the total magnetization M as a function of magnetic field B is given by

$$M = N\mu L\left(\frac{\mu B}{kT}\right) \tag{5.7}$$

where L is the Langevin function given by

$$L(x) = \coth(x) - \frac{1}{x} \tag{5.8}$$

For $x \ll 1$, $L(x) = \frac{1}{3}x$, so that in small fields, or for high temperatures, we have

$$M = \frac{N\mu^2 B}{3kT} \tag{5.9}$$

For $x \to \infty$, $L(x) = 1$ and therefore the saturation magnetization is given by

$$M = N\mu \tag{5.10}$$

The Langevin model assumes monodispersity, such that all the nanoparticles have the same diameter. SEM measurements of particle size distribution parameters in ferrofluids have found size ranges of real particles to be well described by a log-normal distribution [80]. A size distribution can be included in the Langevin model by summing Langevin functions for particles with different diameters.

5.2 Magnetic Nanoparticles as Low-Field NMR Contrast Agents

In this section we outline a number of theories of proton relaxation in aqueous solutions of magnetic nanoparticles. Of particular interest is the frequency/field dependence of the longitudinal and transverse relaxation rates $1/T_1$ and $1/T_2$. Measurements of the field dependence of NMR relaxation rates are known as nuclear magnetic relaxation dispersion (NMRD) profiles [82]. As well as being important in determining the effectiveness of magnetic nanoparticles as contrast agents in magnetic resonance imaging (MRI), these profiles can in principle give information on the nanoparticles themselves. In many cases the theories are extensions of theories developed to describe the relaxation of solvent protons in the presence of paramagnetic ions [82], that allow for the much higher moments of the nanoparticles.

In general the changes in the transverse and the longitudinal relaxation rates observed as a result of adding the nanoparticles to the solution are proportional to the nanoparticle concentration. As is common in the literature, see for example [83], we quote relaxivities R_1 and R_2 as rates per mM of iron.

In the main we will consider ultra-small iron oxide particles (USPIO) containing only one ferrite crystal. A number of parameters affect both the longitudinal and transverse relaxivities, such as the particle size, the particle magnetization, the anisotropy energy and the spread in mean particle sizes. In addition, the time τ_D for the water proton to diffuse a typical particle dimension and the NMR Larmor frequency are also important. In general the nanoparticles are coated with a biocompatible polymer coating. It will be seen that both the size of the magnetic core and the hydrodynamic volume are important in determining the relaxation properties of the nanoparticles.

We will make a number of simplifying assumptions in order to enable analysis and to obtain an understanding of the system:

1. The particles have a spherical magnetic core and a spherical polymer coating
2. The magnetic radius r_M and the hydrodynamic radius r_H are each considered to be the same for all particles, *i.e.* there is no distribution of sizes
3. The magnetization and hence the magnetic moment μ is the same for all particles
4. The magnetic anisotropy is characterized by uniaxial symmetry

These assumptions are clearly approximate, but they allow some insight into the problem. In most situations we are concerned with the theory of motional narrowing, introduced by Bloembergen, Purcell and Pound in their seminal work [84] and described in detail by Abragam [39]. Here the motion of the water protons averages the local magnetic fields caused by the nanoparticles and proton spins must make many visits to the nanoparticles before they relax.

The NMR relaxation rates T_1^{-1} and T_2^{-1} in pure water are determined by the magnetic dipolar interactions between the water protons, with intrinsic relaxation times of the order of seconds, as discussed in Chapter 4. Adding magnetic nanoparticles gives rise to an additional source of local magnetic fields that can be seen by the protons and that can increase the relaxation rates. These local magnetic fields are a source of line broadening even in the absence of motion as spins dephase as a result of local field inhomogeneity. Fluctuating local fields that give rise to longitudinal relaxation can result from Néel or Brownian relaxation of the nanoparticles, or from the diffusion of protons past the nanoparticles. Both processes must be considered and they result in different spectral densities.

All equations in this section are written in S.I. units, unlike many of those in the original references.

5.2.1 The Condition for Motional Narrowing

We first consider the limit for motional narrowing. It is related to the strength of the local field seen by the proton as it moves close to the nanoparticle. We assume that the nanoparticle is a sphere with a constant magnetization M. The field at the equator is given by [85]

$$B_{eq} = \frac{\mu_0 M}{3}\left(\frac{r_M}{r_H}\right)^3 \tag{5.11}$$

where μ_0 is the permeability of free space, r_M is the radius of the magnetic core and r_H is the distance of closest approach, which is given by the size of the coating, *i.e.* the hydrodynamic radius, if the proton cannot penetrate the coating. It is instructive to write Equation 5.11 in terms of the magnitude of the magnetic moment μ of the nanoparticle

$$\mu = \frac{4}{3}\pi r_M^3 M \tag{5.12}$$

to give

$$B_{eq} = \frac{\mu_0}{4\pi}\,\frac{\mu}{r_H^3} \tag{5.13}$$

The proton spin will see this field for a time of the order of τ_D, which will also depend on the hydrodynamic radius. The spin will dephase immediately if

$$\Delta\omega\ \tau_D > 1 \tag{5.14}$$

where

$$\Delta\omega = \gamma B_{eq} = \frac{\mu_0 M \gamma}{3}\left(\frac{r_M}{r_H}\right)^3 \tag{5.15}$$

or alternatively

$$\Delta\omega = \frac{\mu_0}{4\pi}\,\frac{\mu}{r_H^3}\,\gamma \tag{5.16}$$

is the difference between the angular Larmor frequencies when the proton is close to the nanoparticle and when it is in the bulk liquid. Furthermore

$$\tau_D = r_H^2/D \tag{5.17}$$

is the time for the proton to diffuse past the nanoparticle. Combining these two equations we obtain the condition for motional narrowing as

$$\Delta\omega\ \tau_D = \frac{\mu_0 M\gamma}{3}\left(\frac{r_M}{r_H}\right)^3\left(\frac{r_H^2}{D}\right) < 1 \tag{5.18}$$

which can be simplified to

$$\frac{\mu_0 M r_M^2\gamma}{3D}\,\frac{r_M}{r_H} < 1 \tag{5.19}$$

If we have a situation where the hydrodynamic radius is equal to the radius of the magnetic core then the limit becomes

$$\frac{\mu_0 M r_M^2\gamma}{3D} < 1 \tag{5.20}$$

which occurs at a core radius of

$$r_M < \sqrt{\frac{3D}{\mu_0 M\gamma}} \tag{5.21}$$

It is instructive to see when this second limit occurs for magnetite nanoparticles in water. Using a value of $M = 3.5 \times 10^5\,\mathrm{Am}^{-1}$ [80], $D = 2.14 \times 10^{-9}\,\mathrm{m}^2\mathrm{s}^{-1}$ [86] for the diffusion coefficient of water at room temperature and $\gamma/2\pi = 42.576\,\mathrm{MHzT}^{-1}$ for protons, we obtain a limiting core radius of 7.4 nm. This limiting core radius will be larger if $r_H > r_M$, since the distance of closest approach is increased.

5.2.2 The Static Dephasing Regime

For larger nanoparticles, where r_M is big enough such that the condition given in Equation 5.19 is no longer fulfilled and motional averaging does not apply, the NMR linewidth is determined by a) how quickly the protons dephase when they are close to a nanoparticle and b) the fraction of time an average proton spends close to a nanoparticle. The static dephasing case has been studied in detail by Brown [87]. He considers a fluid with a large number of magnetic particles dispersed in it. These particles are considered to be fixed magnetic dipoles which are compact enough to be thought of as point dipoles. A magnetic particle is equally likely to be in any volume element of the sample. This simple model can describe an aqueous solution of magnetic nanoparticles. Each proton sees the static magnetic field $\mathbf{B}_0$ plus a perturbing field resulting from the sum of all the dipole fields due to the nanoparticles in the sample. These local fields cause spins to dephase, resulting in transverse relaxation. The simplest situation to study is when all the nanoparticles are pointing in the same direction, either parallel or perpendicular to $\mathbf{B}_0$.

The envelope of the proton free induction decay resulting from this model is found by integrating the contributions of all the protons in the sample. It is shown in [87] that the decay is exponential in time with transverse relaxation rates

$$\left(\frac{1}{T_2}\right)_{\parallel} = \frac{8\pi^2}{9\sqrt{3}} \frac{\mu_0 M_{aq} \gamma}{4\pi} \tag{5.22}$$

and

$$\left(\frac{1}{T_2}\right)_{\perp} = \frac{4\pi}{3} \frac{\mu_0 M_{aq} \gamma}{4\pi} \tag{5.23}$$

where

$$M_{aq} = \frac{\sum \mu}{V_s} \tag{5.24}$$

is the dipole moment per unit volume, which in this case is the saturation magnetization of the aqueous solution, since the moments are all pointing in the same direction. Note that these equations depend on M_{aq} rather than μ and are correct even for a distribution of nanoparticle sizes, so long as the nanoparticle moments are all pointing in the same direction.

In the general case, by averaging these two results, it can be said that the expression

$$\frac{1}{T_2} \approx 4.6 \, \frac{\mu_0 M_{aq} \gamma}{4\pi} \tag{5.25}$$

is within 10% of the correct value, whatever the orientation of the nanoparticles with respect to $\mathbf{B}_0$.

We can now express this in terms of the angular Larmor frequency $\Delta\omega$ corresponding to the equatorial field of the nanoparticle as given in Equation 5.15 and the volume fraction occupied by the nanoparticles f_a. Assuming that all nanoparticles have the same core radius r_M, the magnetic moment of an individual nanoparticle is given by

$$\mu = \frac{4}{3}\pi r_M^3 M = \frac{4}{3}\pi r_H^3 M \left(\frac{r_M}{r_H}\right)^3 = M V_H \left(\frac{r_M}{r_H}\right)^3 \tag{5.26}$$

where V_H is the hydrodynamic volume of the nanoparticle and M is the saturation magnetization of the nanoparticle. If we have N nanoparticles per unit volume then the volume fraction of nanoparticles is

$$f_a = N V_H \tag{5.27}$$

Therefore in this case we have from Equation 5.24

$$M_{aq} = N\mu = N M V_H \left(\frac{r_M}{r_H}\right)^3 = M f_a \left(\frac{r_M}{r_H}\right)^3 \tag{5.28}$$

using Equations 5.26 and 5.27. Substituting this into Equation 5.22 we obtain

$$\left(\frac{1}{T_2}\right)_{\parallel} = \frac{8\pi^2}{9\sqrt{3}} \left(\frac{r_M}{r_D}\right)^3 \frac{\mu_0 M f_a \gamma}{4\pi} \tag{5.29}$$

which, using Equation 5.15, can be written as

$$\left(\frac{1}{T_2}\right)_{\parallel} = \frac{2\pi\sqrt{3}}{9}\, \Delta\omega f_a \approx 1.2\, \Delta\omega f_a \tag{5.30}$$

where the volume fraction f_a is determined by the hydrodynamic volume of the nanoparticles and $\Delta\omega$ is the difference in Larmor frequency between a spin close to a nanoparticle and one in the bulk. This result is as quoted in Roch *et al.* [88]. A physical understanding of the magnitude of this equation can be gained by considering the proton spins that are close to the nanoparticles, *i.e.* within a volume $\sim V_H$, to have an effective T_2 given by

$$\left(\frac{1}{T_2}\right)_{eff} = \Delta\omega \tag{5.31}$$

The relaxation time measured in the bulk solution is then just $(T_2)_{eff}$ multiplied by the ratio of time spent in the bulk liquid to that spent close to the sample. This ratio is simply f_a^{-1} resulting in a measured relaxation rate of

$$\frac{1}{T_2} = \left(\frac{1}{T_2}\right)_{eff} f_a = \Delta\omega f_a \tag{5.32}$$

which is close to Equation 5.30.

5.2.3 The Motional Narrowing Regime

In the motional narrowing regime proton spins in the region close to the nanoparticle see averaged, weaker magnetic fields and they need to make many visits to the nanoparticle before they dephase or flip. The spins see fluctuating local fields as they diffuse past the magnetic nanoparticles. The motion of the protons averages the local magnetic fields and the spins dephase via a random walk. This averaging results in a narrowing of the NMR line. If we assume that protons close to the nanoparticles see a strong local field which gives rise to a frequency shift $\Delta\omega$ for a time τ_D, then an order of magnitude estimate of the resultant effective relaxation time will be given by [89, 37]

$$\left(\frac{1}{T_2}\right)_{eff} = (\Delta\omega)^2 \tau_D \tag{5.33}$$

which should be compared with Equation 5.31, appropriate for the static regime. The relaxation time measured in the bulk solution will again be given by multiplying this time by the ratio of protons in the bulk liquid to those close to the nanoparticle:

$$\frac{1}{T_2} = (\Delta\omega)^2 \tau_D f_a \tag{5.34}$$

Substituting for $\Delta\omega$ and f_a using Equations 5.16, 5.17 and 5.27 gives the full expression:

$$\frac{1}{T_2} = \left(\frac{\mu_0}{4\pi}\right)^2 \left(\frac{4\pi}{3}\right) \left(\frac{\mu^2\gamma^2 N}{D r_H}\right) \tag{5.35}$$

5.3 Proton Relaxation Rates T_1^{-1} and T_2^{-1} in the Motional Narrowing Regime

We now consider a more rigorous treatment of both the longitudinal relaxation rate T_1^{-1} and the transverse relaxation rate T_2^{-1} in the motional narrowing regime, for protons in aqueous solutions of magnetic nanoparticles. Since longitudinal relaxation involves the change of spin populations, it is essential that there is spectral power in the local magnetic fields at the Larmor frequency. For this reason static local magnetic fields cannot cause longitudinal relaxation, although they can cause dephasing and therefore transverse relaxation as we have described above.

There are two mechanisms for longitudinal relaxation within this model. Firstly as protons diffuse past stationary nanoparticles they will see fluctuating magnetic fields for times of the order of $\tau_D = (r_H^2/D)$ and there will be maximum power at the Larmor frequency ω_0 when

$$\tau_D = \frac{1}{\omega_0} \tag{5.36}$$

Therefore if the longitudinal relaxation rate is measured as a function of frequency, one might expect it to be zero at high and low frequencies but to peak at a frequency given by

$$\omega_{max} = \frac{D}{r_H^2} \tag{5.37}$$

However the nanoparticles themselves also fluctuate at rates determined by the Néel or Brownian relaxation times. This results in finite spectral power at low frequencies and finite longitudinal relaxation rates at low frequencies.

The relative amount of static and fluctuating nanoparticles is actually determined by the static magnetic field $\mathbf{B}_0$ since more nanoparticles will align with the static field as it increases. This results in a shift of the peak in the relaxation rate from that given by Equation 5.37. A theory of the longitudinal relaxation rate of protons in aqueous solutions of magnetic nanoparticles was first proposed by Roch and Muller [90]. This was later improved upon by Koenig and Kellar [83]. The original approach [90] had a few incorrect assumptions that were later incorportated into the approach used by Koenig and Kellar [83], as pointed out by Gillis *et al.* [91]. In the following analysis, equations similar to those in [83] are derived but corrected following Gillis *et al.* [91]. Further analysis by Roch *et al.* [92] suggested that the anisotropy energy of the nanoparticles needs to be considered more carefully.

5.3.1 Curie Spin Theory of the Frequency Dependence of T_1^{-1} and T_2^{-1}

The analysis in this section follows the work of Gillis *et al.* [91] and is an extension to superparamagnetic particles of the concept of the "Curie spin" originally introduced by Gueron [93] in a theory of nuclear magnetic relaxation of macromolecules by paramagnetic ions. In the case of magnetic nanoparticle solutions the interaction of importance is the dipole-dipole interaction between the proton spin and the nanoparticle spin, which we denote S. For the case of an idealized spherical nanoparticle of magnetic moment μ, S can be very large. We assume that S is the same for each nanoparticle. We choose a co-ordinate system such that the static magnetic field, of magnitude B_0, is applied along the z-axis. As the static magnetic field increases, so does the number of nanoparticle spins aligned along the field, due to a competition between magnetic and thermal energy.

One can consider the z-component of the spin to be decomposed into two subcomponents, a time-averaged component

$$\langle S_z \rangle = S_C \tag{5.38}$$

and a fluctuating component s_z. S_C is known as the "Curie" spin. We can write

$$S_z = S_C + s_z \tag{5.39}$$

and since by definition

$$\langle s_z \rangle = 0 \tag{5.40}$$

we have

$$\left\langle S_z^2 \right\rangle = S_C^2 + \left\langle s_z^2 \right\rangle \tag{5.41}$$

The effect of these two subcomponents on the proton relaxation can by found by modifying the standard relaxation equations. For superparamagnetic nanoparticles the "Curie" spin is determined by the Brillouin function B_S. Explicitly, we have [91]

$$S_C = \langle S_z \rangle = \frac{1}{Z} \sum_{m=-S}^{S} m \exp\left(mx/S\right) \tag{5.42}$$

where the partition function Z is given by

$$Z = \sum_{m=-S}^{S} \exp\left(mx/S\right) \tag{5.43}$$

and

$$x = \frac{S\hbar\gamma_S B_0}{k_B T} \tag{5.44}$$

Here γ_S is the gyromagnetic ratio of the electron. Carrying out the sums results in

$$S_C = \langle S_z \rangle = S B_S(x), \tag{5.45}$$

where

$$B_S(x) = \left(\frac{2S+1}{2S}\right) \coth\left(\frac{(2S+1)x}{2S}\right) - \left(\frac{1}{2S}\right) \coth\left(\frac{x}{2S}\right). \tag{5.46}$$

We can determine the fluctuating term $\langle s_z^2 \rangle$ in Equation 5.41 by working out $\langle S_z^2 \rangle$ explicitly. Furthermore

$$\left\langle S_z^2 \right\rangle = \frac{1}{Z} \sum_{m=-S}^{S} m^2 \exp(mx/S) \tag{5.47}$$

is shown in [91] to be given by

$$\left\langle S_z^2 \right\rangle = S(S+1) - S_C \coth\left(\frac{x}{2S}\right) \tag{5.48}$$

and therefore the mean-square fluctuating component can be written as

$$\left\langle s_z^2 \right\rangle = \left\langle S_z^2 \right\rangle - S_C^2 = S(S+1) - S_C \coth\left(\frac{x}{2S}\right) - S_C^2 \tag{5.49}$$

It is important to look at the limits of these equations. As $x \to \infty$, $B_S(x) \to 1$ so that in the high frequency limit the "Curie spin" $S_C \to S$. In the low frequency limit $B_S(x) \to x(S+1)/3S$ and S_C is given by

$$\langle S_z \rangle = S_C = \frac{\gamma_S \hbar S(S+1) B_0}{3 k_B T} \tag{5.50}$$

Equation 5.50 is the expression originally used by Gueron [93] for paramagnetic ions, which needs to be modified as described above for superparamagnetic nanoparticles.

We now look at the limits for $\langle S_z^2 \rangle$. We know that as $x \to \infty$, $\coth(x/2S) \to 1$ and using Equation 5.48 we see that for high fields $\langle S_z^2 \rangle \to S_C^2$. As $x \to 0$, $\coth(x/2S) \to (2S/x) - (x/6S)$ and substituting into Equation 5.48 we obtain

$$\left\langle S_z^2 \right\rangle = \frac{S(S+1)}{3} \tag{5.51}$$

5.3.2 The Large S Limit

We now look at the limit of these equations when $S \gg 1$. This will apply for the case of superparamagnetic single domain nanoparticles, which are objects of large spin. In this case the Brillouin function $B_S(x)$ reduces to the Langevin function $L(x)$ given by

$$L(x) = \coth(x) - \frac{1}{x} \tag{5.52}$$

Changing the parameters from the spin S to the magnetic moment μ, related by

$$\mu = \hbar \gamma_S S \tag{5.53}$$

and using Equation 5.44, gives

$$x = \frac{\mu B_0}{k_B T} \tag{5.54}$$

We can then speak of a "Curie" moment, rather than a "Curie" spin and reformulate Equation 5.45 as

$$\mu_C = \mu L(x) \tag{5.55}$$

Also we can re-express Equation 5.48 in terms of the mean-square z-component of the magnetic moment to give [91]

$$\left\langle \mu_z^2 \right\rangle = \mu^2 \left[1 - 2L\left(x\right)/x\right] \tag{5.56}$$

Note that to derive this, the property $\lim_{y\to 0}\left[y\coth\left(y\right)\right] = 1$ was used, where $y = (x/2S)$. Therefore this applies only for $x \ll S$, which is true so long as $\hbar\gamma_S B_0 \ll 2k_B T$, such that for a sample at room temperature $B_0 \ll 446\,\mathrm{T}$, which is always the case. We can therefore write for the mean-square fluctuating z-component of μ_z

$$\left\langle \mu_z^2 \right\rangle - \mu_C^2 = \mu^2 \left[1 - 2L\left(x\right)/x - L^2\left(x\right)\right] \tag{5.57}$$

In order to calculate both T_1 and T_2 for aqueous systems of nanoparticles we also need the mean-square values of the transverse components of the fluctuating moment. These can be calculated in a similar manner and are given in [91] as

$$\left\langle \mu_x^2 \right\rangle + \left\langle \mu_y^2 \right\rangle = 2\mu^2 L(x)/x \tag{5.58}$$

5.3.3 Correlation Functions and Spectral Densities

In a liquid spins diffuse rapidly in the local magnetic fields of other spins and these time varying fields cause both longitudinal and transverse relaxation. If we consider a set of protons diffusing randomly in the local magnetic fields of a set of nanoparticles, then each proton will see a random local field that can be characterized by a field strength and a time for the random field to change significantly. The random nature of the time dependent local dipolar magnetic fields are described by correlation functions and their associated spectral density functions. In general NMR relaxation rates are proportional to a sum of spectral densities, therefore the frequency dependence of the spectral densities will determine the frequency dependence of the relaxation times. A simple form of correlation function is an exponential, leading to Lorentzian spectral densities [84, 37].

Various authors have made calculations of the spectral densities for random diffusion of spins. Torrey [94] considered point spins diffusing by a random walk and Harmon and Muller [95] took into account the finite size of particles by using the pair correlation functions. This work was extended by Hwang and Freed [96] and independently by Ayant *et al.* [97], who both correctly took account of the finite size of the particles by using the correct boundary conditions when calculating diffusion of the spins. Hwang and Freed also allowed for the fact that one of the spins can be relaxing rapidly. Therefore their spectral density is particularly useful in the case where Néel or Brownian relaxation of the nanoparticles is important. The normalized spectral density $J_F(\omega, \tau_D, \tau_N)$ they calculate is given in [96, 98] to be

$$J_F(\omega, \tau_D, \tau_N) = \mathrm{Re}\left[\frac{1 + \left(\Omega^{1/2}/4\right)}{1 + \Omega^{1/2} + (4\Omega/9) + (\Omega^{3/2}/9)}\right] \tag{5.59}$$

where

$$\Omega = \left(i\omega + \frac{1}{\tau_N}\right)\tau_D \tag{5.60}$$

Ayant *et al.* obtain a spectral density $J_A(z)$ given by [97]

$$J_A(z) = \frac{1 + (5z/8) + (z^2/8)}{1 + z + (z^2/2) + (z^3/6) + (4z^4/81) + (z^5/81) + (z^6/648)} \tag{5.61}$$

J_A is the limit of J_F when the correlation time characterizing the fluctuation of the nanoparticle spin becomes infinitely long. While J_A accounts for the random diffusion of protons through a non-uniform static field, J_F also allows for the flipping of the nanoparticles spins. Therefore J_F becomes more important in low magnetic fields, where the static part is not so strong and fluctuations of the nanoparticle spins make a more significant contribution to the overall time-dependent fields that the protons experience.

5.3.4 Theoretical Model for T_1^{-1} and T_2^{-1}

In order to model the data we use the relaxation equations given by Koenig and Kellar [83], correcting them as described by Gillis *et al.* [91] using Equations 5.55, 5.57 and 5.58. This leads to the following equations [99]

$$\begin{aligned} T_1^{-1} = 9A \left\{ L^2(x) J_A\left(\sqrt{2\omega_I \tau_D}\right) + \left[1 - 2\left(L(x)/x\right) - L^2(x)\right] J_F(\omega_I, \tau_D, \tau_{N1}) \right\} \\ + 3A\left(L(x)/x\right)\left\{ J_F(\omega_I - \omega_S, \tau_D, \tau_{N2}) + 6J_F(\omega_I + \omega_S, \tau_D, \tau_{N2}) \right\} \end{aligned} \tag{5.62}$$

and

$$\begin{aligned} T_2^{-1} = (3/2)\, A \left\{ L^2(x) \left[3J_A\left(\sqrt{2\omega_I \tau_D}\right) + 4J_A(0) \right] \right. \\ + \left[1 - 2\left(L(x)/x\right) - L^2(x)\right] \left[3J_F(\omega_I, \tau_D, \tau_{N1}) + 4J_F(0, \tau_D, \tau_{N1}) \right] \Big\} \\ + 3A\left(L(x)/x\right)\left\{ (1/2)\, J_F(\omega_I - \omega_S, \tau_D, \tau_{N2}) \right. \\ \left. + 3J_F(\omega_S, \tau_D, \tau_{N2}) + 3J_F(\omega_I + \omega_S, \tau_D, \tau_{N2}) \right\} \end{aligned} \tag{5.63}$$

where ω_I and ω_S denote the Larmor frequencies of the proton and electron spins respectively. τ_{N1} and τ_{N2} correspond to the longitudinal and transverse Néel times. The coefficient A is given by

$$A = \left(\frac{\mu_0}{4\pi}\right)^2 \left(\frac{32\pi}{405}\right) \left(\frac{\mu^2 \gamma^2 N}{D r_H}\right) \tag{5.64}$$

Apart from the difference in the numerical factor, Equation 5.64 is identical to Equation 5.35 in Section 5.2.3, which gives an expression for T_2^{-1} in the motional narrowing regime. Equations 5.62 and 5.63 were used to generate the theoretical curves in Section 6.3.

Chapter 6

NMR on Aqueous Magnetic Nanoparticle Solutions

The work presented in this chapter was undertaken as part of the EU funded sixth framework Biodiagnostics research project and measured the frequency dependence of the NMR relaxation times of protons in aqueous solutions of coated superparamagnetic nanoparticles in order to evaluate their effectiveness as contrast agents for low-field MRI. Using the broadband DC SQUID spectrometer allowed for direct measurements of this frequency dependence to be extended down to much lower frequencies than was hitherto possible, since in the past such measurements were only achieved using field cycling relaxometry, as described by Kimmich and Anoardo [100].

The first two sections in this chapter summarize all the results obtained for two samples of aqueous dispersions of superparamagnetic iron-oxide nanoparticles in the Néel regime. These are followed by a comparison of the data to the theoretical model established in the previous chapter. Finally, the penultimate section presents results for thermally blocked cobalt-ferrite nanoparticles undergoing Brownian relaxation.

6.1 NMR on fluidMAG-HEAS Fe_3O_4 Nanoparticle Solutions

6.1.1 Characterization of fluidMAG-HEAS Sample

The first sample studied was an aqueous dispersion of fluidMAG-HEAS magnetic nanoparticles, lot number 1500/06, provided by Chemicell [101]. The particles consist of a magnetite (Fe_3O_4) core, see Goya *et al.* [102] for a description of the crystallographic structure of magnetite, with a hydrophilic hydroxyethyl-starch polymer coating. They are suspended in double-distilled water. The properties of this suspension, as quoted by the manufacturer, are given in Table 6.1. The original sample concentration with a total iron content of 34 mg/ml corresponds to 610 milliMolars (mM) of iron. Based on an estimated core diameter of around 8–10 nm, the magnetization behaviour of the particles is expected to be superparamagnetic with Néel relaxation being the dominant relaxation mechanism.

Weight of volume*	100	mg/ml
Total iron content	34	mg/ml
Number of particles	1.3×10^{16}	g^{-1}
Density	1.25	g/cm^3
Hydrodynamic diameter	65	nm
Estimated core size	8–10	nm

Table 6.1: Properties for fluidMAG-HEAS 1500/06. *Weight of volume corresponds to the weight of dried nanoparticles diluted in a millilitre of solution.

A sample of this batch of fluidMAG-HEAS was sent to Imego for further characterization. The Photon Correlation Spectroscopy (PCS) measurements they provided us with are shown in Figure 6.1 and were obtained with a Zeta Sizer Nanoseries from Malvern Instruments. They determine the mean hydrodynamic size of these

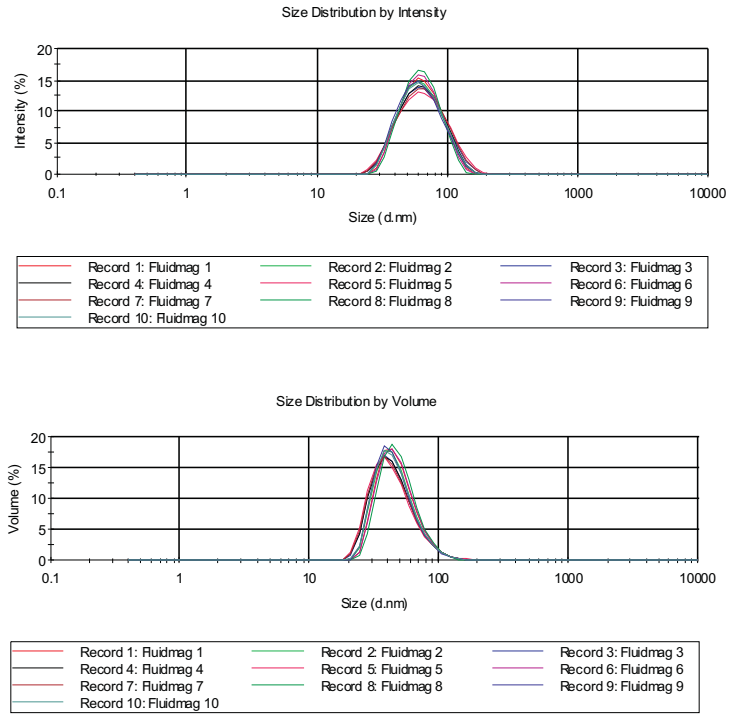

Figure 6.1: Photon Correlation Spectroscopy measurements for fluidMAG-HEAS.

fluidMAG-HEAS particles to be $66.6 \pm 2.0\,\text{nm}$. According to Imego, the size distribution does not appear to be very broad and there is no indication that the particles have agglomerated.

The dynamic magnetic measurements performed using AC susceptometry give information about the rotational Brownian motion of the particles if their Néel relaxation is blocked. In our case, the dominant relaxation mechanism is Néel and the AC susceptibility measurement is thus unsuitable for accurately measuring the core size distribution. The imaginary susceptibility peak would be in the GHz range and the range of the Imego DynoMag AC Susceptometer only extends to 250 kHz. The conclusion drawn by Imego from their AC susceptibility data, shown in Figure 6.2, was that the core size distribution is quite broad and that a large fraction of the particles undergoes Néel relaxation, since the real part of the susceptibility never reaches zero within the available frequency range. For magnetite this equates to a prevalence of single domain cores with a diameter of less than $\sim 12\,\text{nm}$ [103].

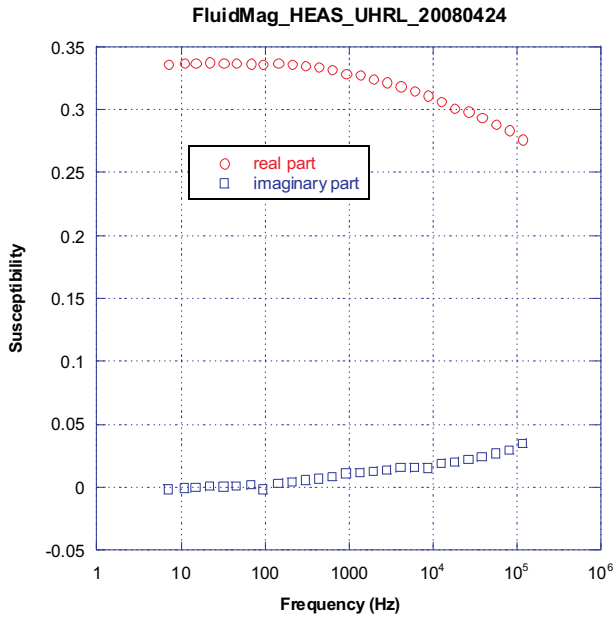

Figure 6.2: AC susceptibility measurements for fluidMAG-HEAS.

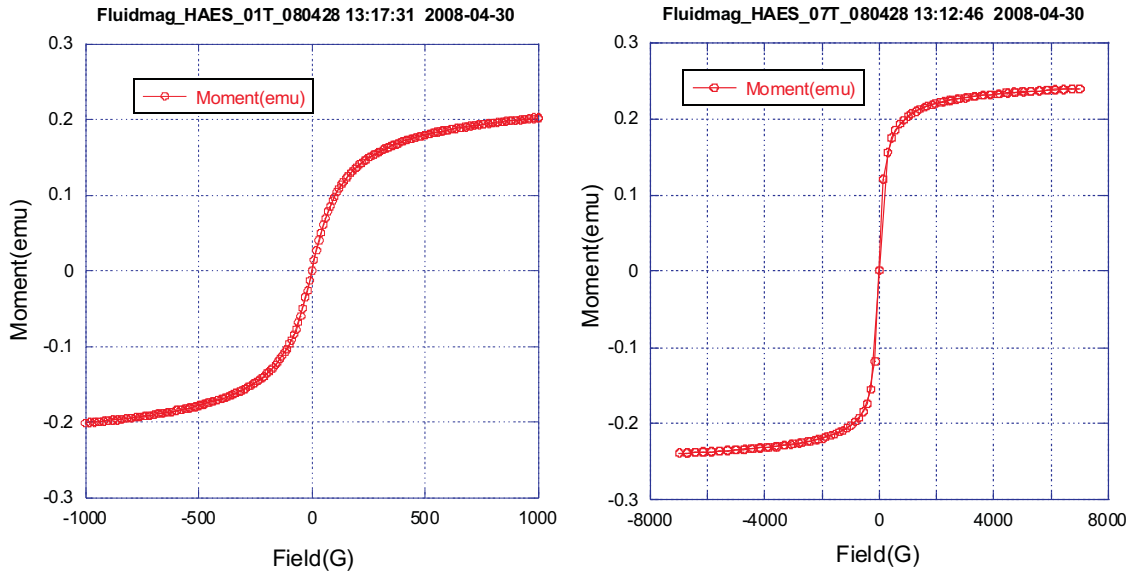

Figure 6.3: Vibrating Sample Magnetometer hysteresis curves of fluidMAG-HEAS with an iron content of 34 mg/ml, for two different magnetic field ranges.

The static magnetic measurements obtained using a Vibrating Sample Magnetometer (VSM), also show that the particles are superparamagnetic, since the hysteresis curves exhibit no remanence or coercivity. From the hysteresis curves shown in Figure 6.3, the saturation magnetization is measured to be 0.24 emu, corresponding to $M_S = 2.4 \times 10^{-4}\,\mathrm{Am}^2$. To obtain the average magnetic moment of a single nanoparticle, it is necessary to know the total number of particles in the measured sample. The weight of volume of the undiluted solution is given as 100 mg/ml and the volume used to measure the curve was $\sim 50\,\mu\mathrm{l}$, giving about 5 mg of nanoparticle material. Furthermore the number of particles per weight of dried nanoparticles being $1.3 \times 10^{16}\,\mathrm{g}^{-1}$, gives the total number of particles in the measurement sample as $N = 6.5 \times 10^{13}$. Therefore the average nanoparticle moment for fluidMAG-HEAS is

$$\mu = \frac{M_S}{N} = \frac{2.4 \times 10^{-4}\,\mathrm{Am}^2}{6.5 \times 10^{13}} = 3.7 \times 10^{-18}\,\mathrm{Am}^2$$

The expected average magnetic moment of a 10 nm diameter magnetite nanoparticle can be estimated by assuming a value for M. Here we use $M = 3.5 \times 10^5\,\mathrm{Am}^{-1}$, which is quoted as a typical value for the intrinsic magnetization of small magnetite single domains in Schaller *et al.* [104]. The volume of a 10 nm diameter particle is $V = \frac{4}{3}\pi(5 \times 10^{-9}\,\mathrm{m})^3 = 5.2 \times 10^{-25}\,\mathrm{m}^3$ and therefore the calculated magnetic moment of such a particle is:

$$\mu_{calc} = (5.2 \times 10^{-25}\,\mathrm{m}^3)(3.5 \times 10^5\,\mathrm{Am}^{-1}) = 1.8 \times 10^{-19}\,\mathrm{Am}^2$$

The calculated magnetic moment per particle is about 20 times smaller than the measured moment, which in this case would correspond to an average nanoparticle diameter of ~ 27.3 nm.

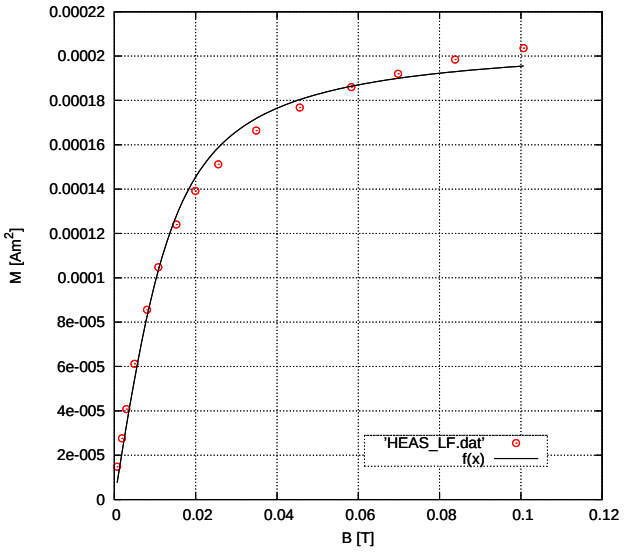

Figure 6.4: Simple Langevin function fit to VSM data for the fuidMAG-HEAS.

The positive lower field range magnetization data was converted from emu versus Gauss into units of Am^2 versus Tesla, in order to fit to it a simple Langevin function of the form

$$f(x) = P_1 \left[\coth\left(\frac{P_2\ x}{kT}\right) - \frac{kT}{P_2\ x} \right] \tag{6.1}$$

where the two parameters to be fitted, $P_1 = M_S$ and $P_2 = \langle\mu\rangle$, will be given in units of Am^2. kT is taken to be 4.1×10^{-21} J for 297–300 K.

The best fit to the data is shown in Figure 6.4 and gives the total saturation magnetization of the sample as $M_S = 2.08 \times 10^{-4}\,Am^2$, which is lower than the apparent value for M_S of $2.4 \times 10^{-4}\,Am^2$. This is due to the Langevin model not accounting for the polydispersity of the magnetic core sizes found in the solution. The fit also gives the average magnetic moment as $\langle\mu\rangle = 6.76 \times 10^{-19}\,Am^2$, corresponding to an average diameter of 15.4 nm. These values would put the total number of particles in the sample at

$$N = \frac{M_S}{\langle\mu\rangle} = \frac{2.08 \times 10^{-4}\,Am^2}{6.76 \times 10^{-19}\,Am^2} = 3.08 \times 10^{14}$$

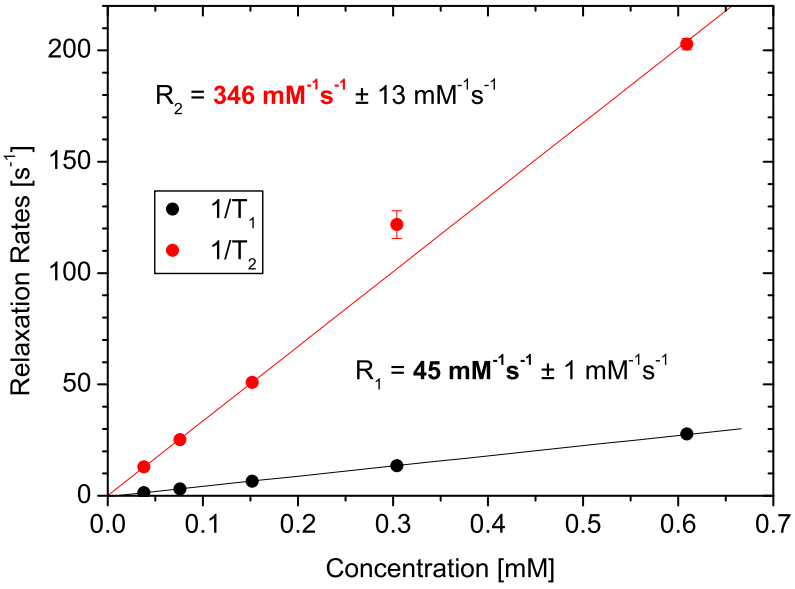

Figure 6.5: Relaxation rates as a function of concentration for fluidMAG-HEAS at $B_0 = 0.5\,\mathrm{T}$.

In addition to these three characterization measurements, for iron-oxide nanoparticle solutions it is usual to quantify their effectiveness at providing NMR contrast at a given measurement frequency in terms of their relaxivities R_1 and R_2 given by

$$R_{1,2} = \frac{d\,(1/T_{1,2})}{dc} \tag{6.2}$$

where c is the iron concentration in mM, such that R_1 and R_2 have units of $\mathrm{mM}^{-1}\mathrm{s}^{-1}$.

Before proceeding with the low-field experiment, we therefore measured proton relaxation times for different iron concentrations in two higher fields, with proton Larmor frequencies corresponding to 15 and 21 MHz, using two conventional tuned pulsed RF NMR spectrometers from Teachspin [105], that were available in the teaching laboratory of the Royal Holloway Physics department. We first diluted some of the original solution by a factor of 1000 to obtain an iron content of 34 µg/ml or 0.61 mM. From this a series of four consecutive factor 2 dilutions were produced, the solution with the lowest concentration having an iron content of 2.125 µg/ml or 0.0375 mM. Plotting the measured relaxation rates T_1^{-1} and T_2^{-1} versus the iron

concentration in mM and fitting a linear function to determine the slope, gives R_1 and R_2 as shown in Figure 6.5 for measurements taken at 21 MHz. Results for both frequencies are summarized in Table 6.2.

f_0 [MHz]	B_0 [T]	T_1 [ms]	T_2 [ms]	R_1 [$\mathrm{mM^{-1}s^{-1}}$]	R_2 [$\mathrm{mM^{-1}s^{-1}}$]
15	0.35	24.5 ± 0.3	4.7 ± 0.1	53 ± 3	299 ± 8
21	0.50	36.0 ± 0.3	4.9 ± 0.1	45 ± 1	346 ± 13

Table 6.2: Summary of high field NMR measurements for fluidMAG-HEAS.

6.1.2 Longterm Stability of fluidMAG-HEAS Solutions

Effect of Stycast Containers on Sample Stability

In preparation of the first low-field experiment some of the original fluidMAG-HEAS solution was again diluted in deionized water by a factor of 1000 to obtain a solution with a total iron content of 34 µg/ml. Approximately 140 µl of this solution was filled into one of our standard sample cells made from Stycast 1266. The low-field experiment using the SQUID NMR dipper probe was not conducted until two months after the sample cell had been filled, at which point we measured low-field relaxation times of $T_1 \sim 2.6\,\mathrm{s}$ in the prepolarizing field $B_p \approx 2.56\,\mathrm{mT}$ (where $f_0 \sim 109\,\mathrm{kHz}$) and $T_2 \sim 450\,\mathrm{ms}$.

Using the conventional 15 MHz NMR spectrometer, both the remaining solution mixed two months earlier and the sample in the Stycast cell were checked to see if they still exhibited the same relaxation rates at high fields, thus determining whether or not the solution in the experimental cell had deteriorated and if this diluted nanoparticle suspension was intrinsically unstable over time. It was found that T_1 and T_2 of the Stycast cell sample had become much longer, while those of its source solution were still around 30 ms and 5 ms respectively, as had been measured consistently earlier on at this frequency and concentration.

A second Stycast cell was filled with some more of the 34 µg/ml solution and monitored over time. We found that after only 24 hours the relaxation times measured at 15 MHz had increased to $T_1 = 1.41\,\mathrm{s}$ and $T_2 = 130\,\mathrm{ms}$ compared to the previous values, shown in Table 6.2 of about 25 ms and 5 ms respectively. We assumed that this increase in relaxation times was due to an effective reduction in concentration of the nanoparticles in the solution. Multiplying the increased relaxation times with the corresponding relaxivities given in Table 6.2 and taking the inverse, gives an effective nanoparticle concentration of $13 \times 10^{-3}\,\mathrm{mM}$ for T_1 and $26 \times 10^{-3}\,\mathrm{mM}$ for T_2. The difference in the effective concentrations obtained from T_1 and T_2 could be an indication that aggregated nanoparticles, subjected to magnetic dipole-dipole interactions between each other and also to attractive Van-der-Waals forces towards each other and the container walls, will appear thermally blocked and immobile to the protons diffusing around them, resulting in reduced spectral power available at the Larmor frequency, while at the same time the aggregates still provide a source of additional static local field variations to a greater degree. It was hypothesized that the nanoparticles must stick irreversibly to the walls of the Stycast container, possibly by chemically bonding to unsaturated bonds in the Stycast resin. Stycast was therefore deemed to be an unsuitable material for storing these particular nanoparticles.

Sample Stability in Redesigned Kel-F Sample Cell

As described in Section 3.4.3, the sample cell was subsequently redesigned and made out of Kel-F (PCTFE), a material that was chosen for its non-stick properties and since it doesn't contain protons in its chemical structure that could otherwise give rise to spurious NMR signals. The cell is closed with a screw-thread seal and can be made sufficiently leaktight by the insertion of a Teflon disc and by wrapping some PTFE tape on the thread.

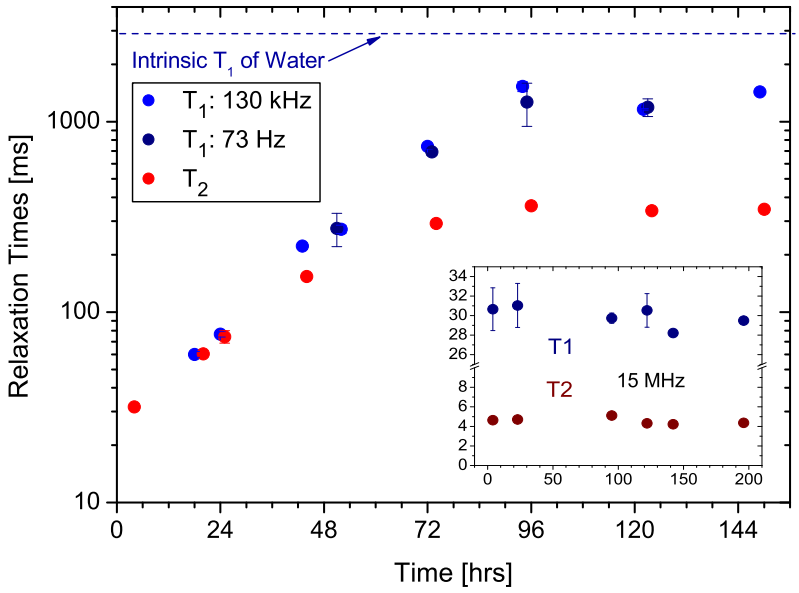

Figure 6.6: Time evolution of T_1 and T_2 during the low-field experiment and on the bench (inset).

Before using it on the low-field probe, the new cell was tested on the bench. A fresh batch of fluidMAG-HEAS 34 µg/ml solution was prepared and immediately filled into a Kel-F test cell and a small glass NMR sample container for reference. Regular monitoring of the relaxation times at 15 MHz show that the sample is stable in the Kel-F test cell over at least a month.

Encouraged by the initial test results for the Kel-F sample container, a second low-field experiment was conducted with a 100 µl sample of the second batch of 34 µg/ml solution prepared the week before, in a Kel-F sample cell. Unfortunately the nanoparticle solution was not stable under experimental conditions and we observed a permanent increase in relaxation times over a few days, as shown in Figure 6.6. When opening up the sample cell, a rust-coloured residue could be seen on the Kel-F walls and the Teflon lid disc, an indication that the nanoparticles stuck to the surfaces of the container.

Since this time, unlike in the Stycast cell case, the solution was stable in the cell on the bench, it was suspected that the lack of stability under experimental conditions might be somehow related to the operation of the heater and diode, needed to keep the cell at room temperature. Two further Kel-F cells were therefore filled for testing on the bench: one with a heater wound onto it, the other with a diode glued to it. Both were operated continuously and the samples in both cells exhibited an increase in relaxation times, even though the effect was not as pronounced as in the actual experiment. The diode operation resulted in an increase of T_1 from 30 ms to 50 ms over the course of $\sim$ 40 hours, while operating the heater, albeit with a considerably lower current than under experimental conditions, had the same effect in only $\sim$ 24 hours. These tests showed that the operation of the heater and/or diode does result in a slow aggregation of the nanoparticles at the sample cell wall. But it remains unclear exactly what the mechanism underlying the aggregation process is or why it is irreversible.

Sample Stability in Final Experimental Conditions

In all our testing, the heater and diode were operated without any filtering, so we investigated the possibility of AC interference being a problem. We found that we were able to stabilize the sample in experimental conditions, simply by increasing the filtering for the heater operation. As described in Section 3.4.2, passive filtering components are used in between the diode and heater power supplies and the probe to cut out any high frequency current noise. The cut-off frequency of the original low-pass filtering circuit for the heater was measured to be around 500 Hz. Assuming that there might be a considerable 50 Hz mains component getting through, we replaced the 3.3 µF capacitor across the heater leads with two 220 µF ones, shifting the circuit's cut-off frequency down to below 10 Hz. Figure 6.7 shows the measured frequency responses for the original and modified heater filtering circuits.

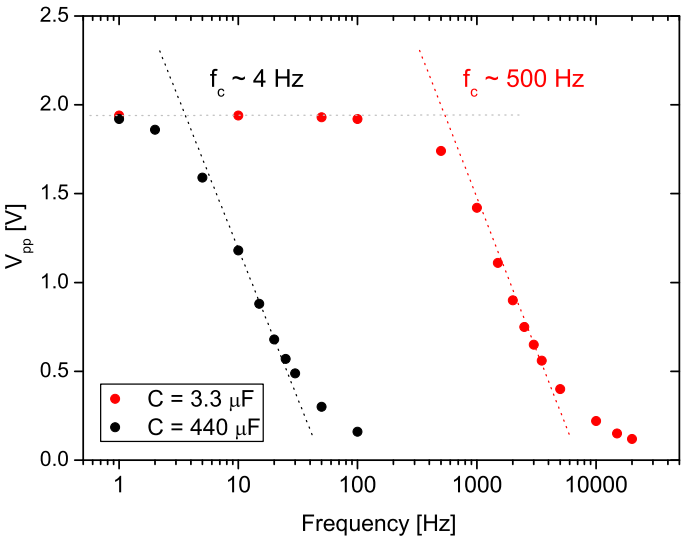

Figure 6.7: Comparison of frequency response of heater filter circuits with different capacitances.

Subjecting the sample to extensive testing on the bench under experimental conditions, we observed that it was practically stable for a period of at least two weeks. The only detrimental effect was a slight but constant drift in T_1 during the entire test. In total it went up from $\sim 27\,\text{ms}$ to $\sim 33\,\text{ms}$.

6.1.3 Low Field NMR on fluidMAG-HEAS

Low Field Measurements

Once the sample was sufficiently stable under experimental conditions, a final set of low-field measurements was taken with the 0.61 mM fluidMAG-HEAS solution. We measured T_2^* as a function of frequency to determine the intrinsic T_2 of the solution in zero field. We observed $T_2^* \sim 13$–$14\,\text{ms}$, corresponding to signal linewidths of 22–25 Hz, as shown in Figure 6.8. The slope of the linear fit equals the magnet inhomogeneity and assuming T_2 to be constant over the measurement range of 1–30 kHz, the y-intercept will give $T_2^*(0) = T_2$. We cannot measure T_2 directly using a Spin-Echo sequence, because the effect of the nanoparticles dominates over the magnet inhomogeneity.

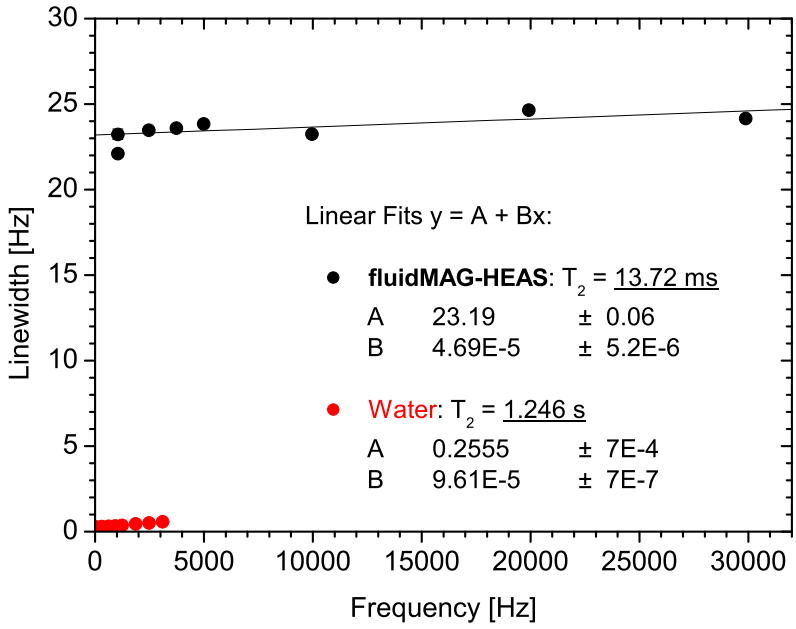

Figure 6.8: Linewidth as a function of frequency for the 0.61 mM fluidMAG-HEAS solution (black) and deionized water (red).

We used the previously established adiabatic turn-off and 1/4-turn techniques, detailed in Section 4.2.1, to measure T_1 in low and ultralow fields respectively. These techniques are necessary in order to transfer enough magnetization into the longitudinal direction, since the sample polarization at such low fields is too small to provide adequate signal sizes. T_1 fits for different measurement techniques are shown in Figures 6.9 and 6.10.

At intermediate fields, on the order of a few tens of kHz, a conventional RF inversion-recovery sequence was used. The upper limit for this method is dictated by the maximum static background field that can be persisted in the magnet. Beyond that, T_1 was measured in the prepolarizing field by varying the length of the prepolarizing pulse. The usual prepolarizing pulse corresponds to a field of $B_p \sim 2.3\,\mathrm{mT}$, where $\omega_0/2\pi \sim 100\,\mathrm{kHz}$. But we can generate fields of up to 15 mT, for which $\omega_0/2\pi \sim 640\,\mathrm{kHz}$, in the transmitter coil. Unfortunately measuring T_1 in higher prepolarizing fields than $B_p \sim 2.5\,\mathrm{mT}$ destroys the field homogeneity across the sample area because of flux trapping in the inner niobium shield and is therefore

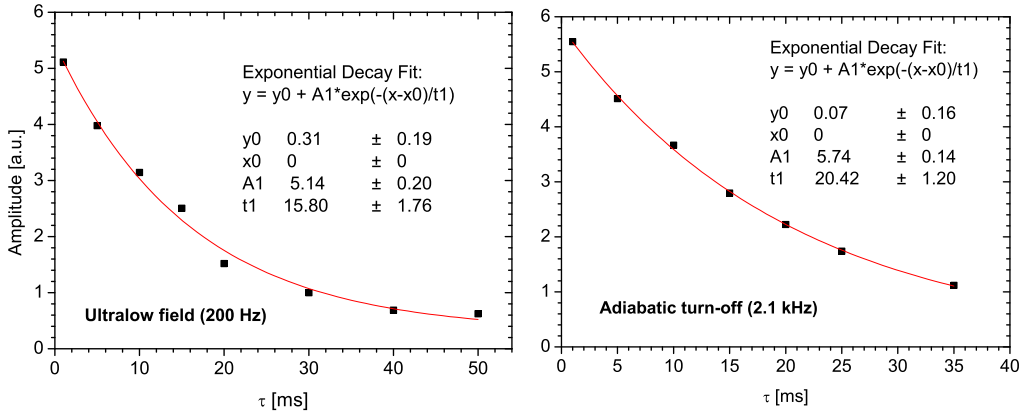

Figure 6.9: T_1 at low - 2.1 kHz (right) and ultralow - 200 Hz (left) fields.

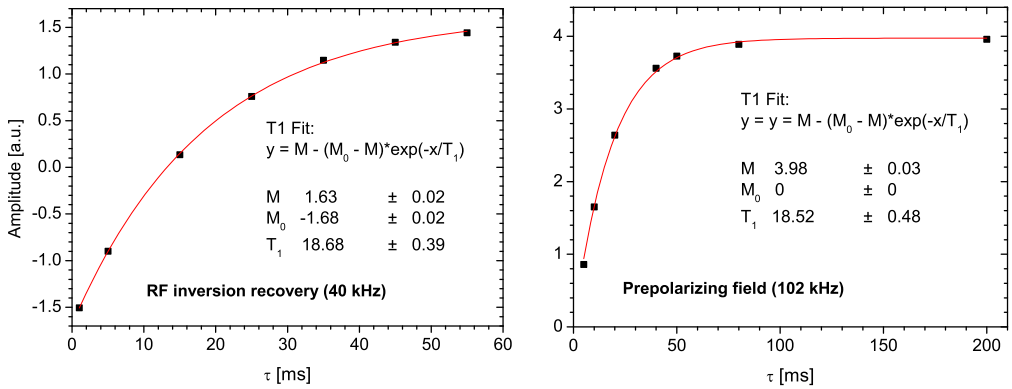

Figure 6.10: T_1 at intermediate - 40 kHz (left) and high - 100 kHz (right) fields.

the last measurement taken before having to warm up the probe.

Because the whole experiment extended over the course of several days, we re-measured T_2 and T_1 in the prepolarizing field to determine their drift rates, which we assumed to be linear. The resulting calibration, shown in Figure 6.11, enabled us to apply a relative correction to our results to adjust for changes in the relaxation times over time.

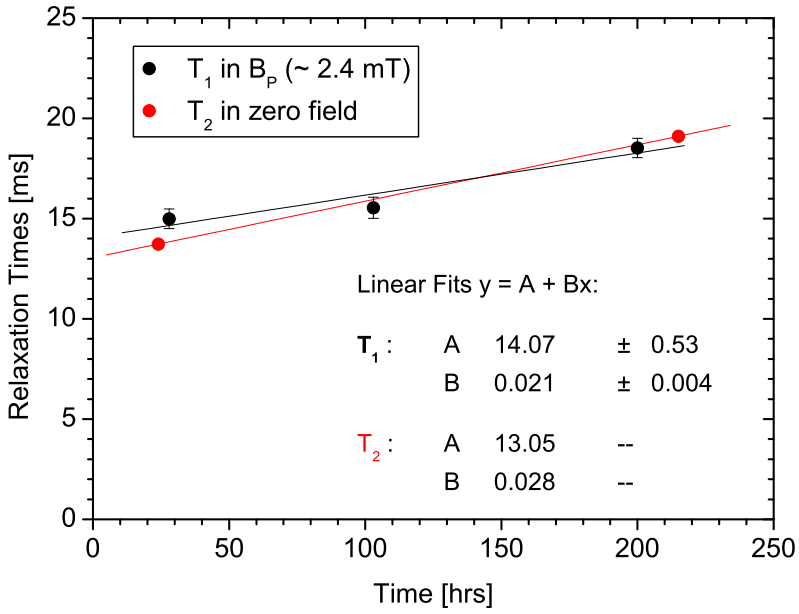

Figure 6.11: Drift in T_1 and T_2 over time.

Calculation of Predicted T_2 for fluidMAG-HEAS

In the motional narrowing regime T_2 is given by Equation 5.34

$$\frac{1}{T_2} = (\Delta\omega)^2 \tau_D f_a$$

where from Equations 5.16 and 5.27 we have

$$\Delta\omega = \frac{\mu_0}{4\pi}\frac{\mu}{r_H^3}\gamma \quad \text{and} \quad f_a = NV_H.$$

The number of particles per unit volume of the fluidMAG-HEAS solution was determined from the Langevin fit to the magnetization data to be $N = 6.2 \times 10^{21}\,\mathrm{m}^{-3}$. The measured hydrodynamic volume is $V_H = \frac{4}{3}\pi\,(33.3 \times 10^{-9}\,\mathrm{m})^3 = 1.55 \times 10^{-22}\,\mathrm{m}^3$, giving the nanoparticle volume fraction as $f_a = 0.96$. The sample solution used in our experiments was a factor of 1000 more dilute than the source solution, therefore we have $f_a = 9.6 \times 10^{-4}$. Using the magnetic moment determined by the Langevin fit, $\mu = 6.76 \times 10^{-19}\,\mathrm{Am}^2$, then gives $\Delta\omega = 4.9 \times 10^5\,\mathrm{s}^{-1}$. Taking the diffusion co-

efficient D for water at room temperature to be $D = 2.14 \times 10^{-9}\,\mathrm{m^2 s^{-1}}$ [86], we also have $\tau_D = r_H^2/D = 5.18 \times 10^{-7}\,\mathrm{s}$. Substituting these values gives an estimated relaxation time of

$$\frac{1}{T_2} = (\Delta\omega)^2\,\tau_D f_a = (4.9 \times 10^5\,\mathrm{s^{-1}})^2(5.187 \times 10^{-7}\,\mathrm{s})(9.6 \times 10^{-4}) = 120\,\mathrm{s^{-1}}$$

This corresponds to $T_2 = 8.4\,\mathrm{ms}$.

In the static dephasing regime, T_2 is given by Equation 5.32, such that

$$\frac{1}{T_2} = \Delta\omega f_a = (4.9 \times 10^5\,\mathrm{s^{-1}})(9.6 \times 10^{-4}) = 470\,\mathrm{s^{-1}}$$

This corresponds to $T_2 = 2.1\,\mathrm{ms}$.

The static dephasing regime calculation gives the shortest T_2 possible for any given nanoparticle solution, describing the situation where protons in the vicinity of the nanoparticles dephase immediately. If the diffusion time τ_D is such that the protons make many visits to different nanoparticles while they dephase, the local field variations that the protons see are averaged and T_2 becomes longer. The T_2 values that we measured in the high field limit were around 5 ms, which is between the predicted values of 2 ms for the static regime and 8 ms for the motional narrowing regime. This could be an indication that the protons are subject to some degree of motional narrowing, but also probably undergo more rapid dephasing when close to nanoparticles with larger cores or smaller hydrodynamic sizes, thus providing more evidence of the polydisperse nature of the fluidMAG-HEAS nanoparticles.

Summary of Relaxivity versus Frequency Data for fluidMAG-HEAS

While the high field relaxivities were determined directly by measuring relaxation times as a function of iron concentration, at low fields we assumed that for deionized water $T_1 = T_2 \sim 3\,\mathrm{s}$, such that:

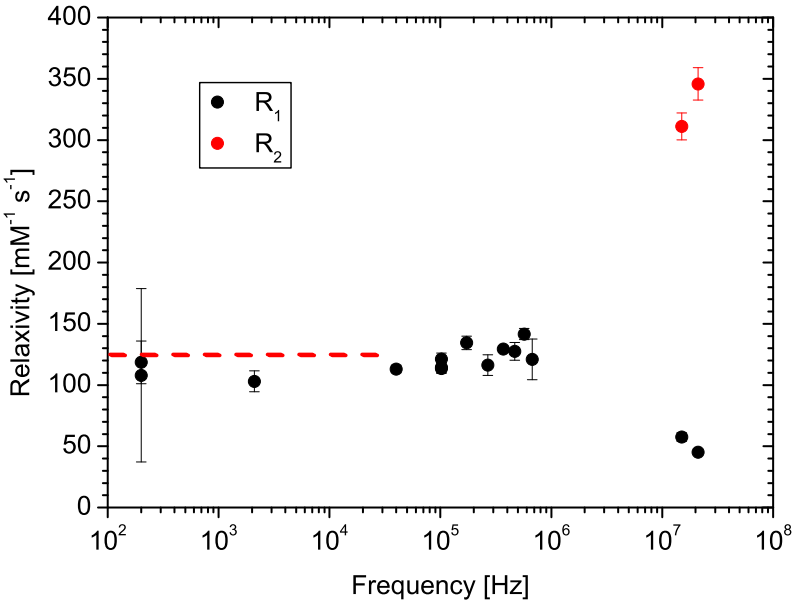

Figure 6.12: Overview of relaxivities measured to date for the fluidMAG-HEAS nanoparticles.

$$R_{1,2} = \frac{1}{c}\left(\frac{1}{T'_{1,2}} - \frac{1}{3}\right) \tag{6.3}$$

where T'_1 and T'_2 are the measured relaxation times.

As expected, R_1 is higher at low fields than at high fields, while R_2 is reduced at low fields, such that $R_1 \approx R_2$. There could also potentially be a peak in the relaxivities around a few MHz (refer to Section 6.3 for more details), but unfortunately that range is not accessible to us at the moment. The T_1 data between 200–700 kHz were taken just before ending the experiment, by sequentially increasing the prepolarizing field. After applying the highest possible prepolarizing field, for which we had a current of 7 A in the transmitter coil, the field homogeneity had worsened to such a degree that T_2^* shortened to ~ 3 ms.

Figure 6.12 is a summary of all the relaxivity measurements that have been made to date for the fluidMAG-HEAS sample. As mentioned in the previous section, we assume T_2 to be constant at low fields and have therefore used $T_2^*(0)$ to calculate R_2 and depicted it as a line extending across the range of our T_2^* measurements.

6.2 NMR on POA@SPION Solutions

The Royal Institute of Technology in Sweden, KTH [106], provided us with another sample of superparamagnetic iron-oxide nanoparticles (SPION). Their particles have a 7 nm core with a PF127/oleic acid (POA) coating and were delivered in aqueous solution with an iron content of 5 mg/ml, corresponding to 90 mM of iron. These two parameters were the only information given by KTH about their POA@SPION sample, of which they only provided a 0.5 ml volume. More than half of that was sent to Imego for characterization. Unfortunately they did not measure the sample in the VSM at the time, so there are no magnetization measurements available for this sample.

The AC susceptibility measurements, see Figure 6.13, indicate that POA@SPION consists of particles in the Néel regime and that the iron content is indeed smaller than that of the fluidMAG-HEAS source solution. From the PCS measurements, shown in figure 6.14, the average hydrodynamic diameter of these particles is determined to be $d_H \sim 100\,\text{nm}$.

We diluted 68 µl of the original sample in 10 ml of deionized water to get a solution with a concentration of 0.61 mM of iron for direct comparison with fluidMAG-HEAS. From this, we also performed the same series of factor 2 dilutions to measure the relaxivities at 15 and 21 MHz directly. For a 0.61 mM concentration, we measured $T_1 = 290\,\text{ms}$ and $T_2 = 14\,\text{ms}$ at 15 MHz, compared to $T_1 = 26\,\text{ms}$ and $T_2 = 5\,\text{ms}$ for the fluidMAG-HEAS sample.

A 0.61 mM solution of POA@SPION was then measured using the low-field SQUID NMR spectrometer. The relatively long relaxation times measured, see Figure 6.15, are possibly a result of the particular coating used, rather than the result of an inherent instability, as was originally thought. It was not possible to do a detailed stability study or to check whether the measured low-field relaxation times were reproducible due to the insufficient amount of source material available.

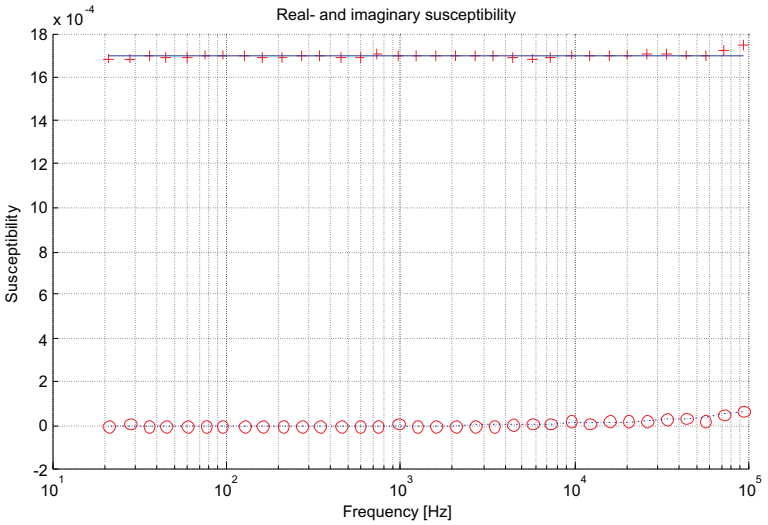

Figure 6.13: AC susceptibility measurements for POA@SPION.

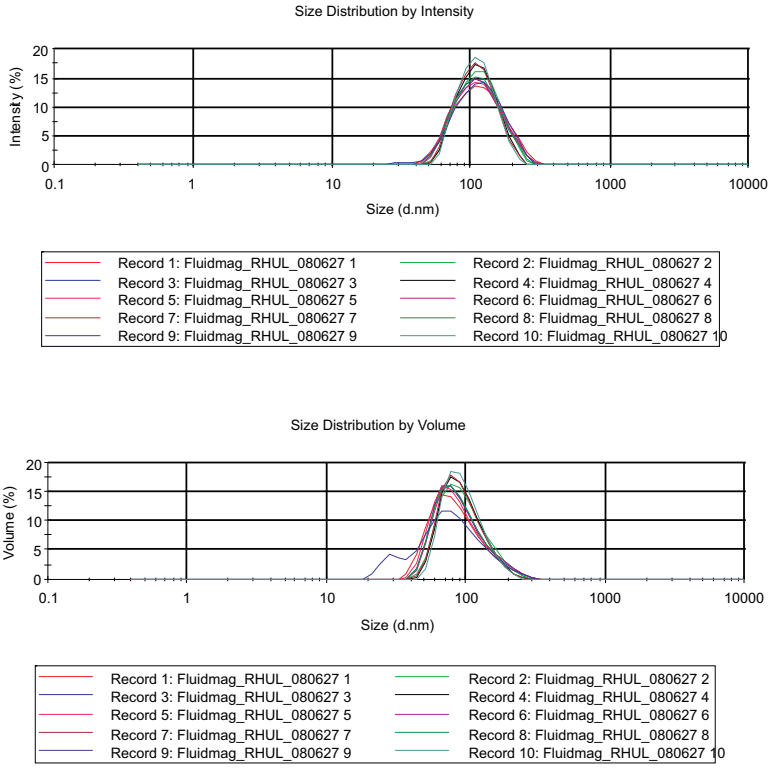

Figure 6.14: PCS measurements for POA@SPION.

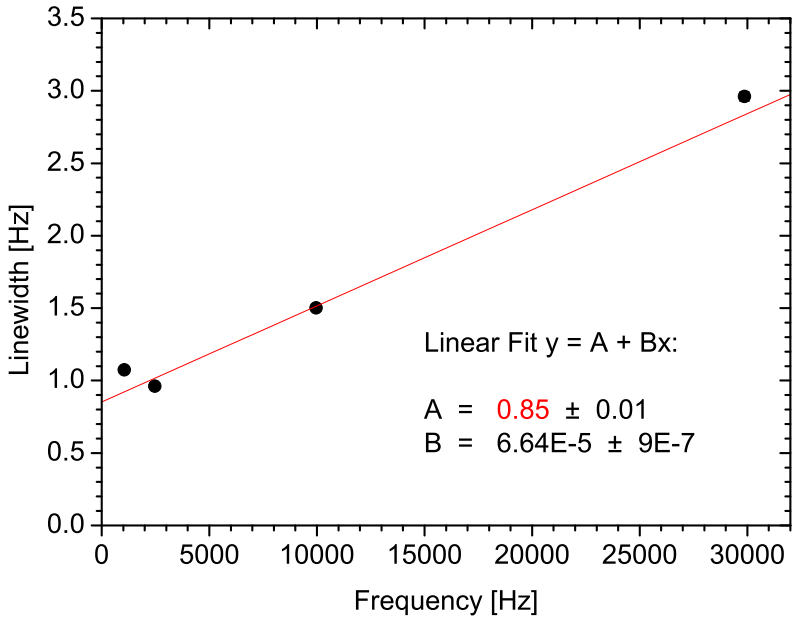

Figure 6.15: Linewidth as a function of frequency for the 0.61 mM POA@SPION solution.

Details of the POA coating are given in an article by J. Qin *et al.* [107] from KTH. The Pluronic F127 (PF127) is an ABA-type triblock copolymer consisting of polypropylene oxide (PPO) and polyethylene oxide (PEO). While the PPO block in the middle of the PF127 molecule associates with the alkyl tail of the oleic acid through the hydrophobic interaction, the hydrophilic PEO end blocks solubilize the particles in aqueous media. In this article it is hypothesized that the structure of the POA coating is responsible for a decreased R_1 while at the same providing an R_2 that is comparable to similar sized nanoparticles with simple permeable polymer coatings. For one, water molecules diffusing among the hydrophilic PEO ends will hydrogen bond to these and their reduced mobility should result in an additional shortening of T_2. But also, since there is a compact hydrophobic layer comprised of intercalated PPO blocks and oleic acid molecules surrounding the magnetic core, the water molecules cannot get close to the core, which is seen as a requirement for effective T_1 shortening.

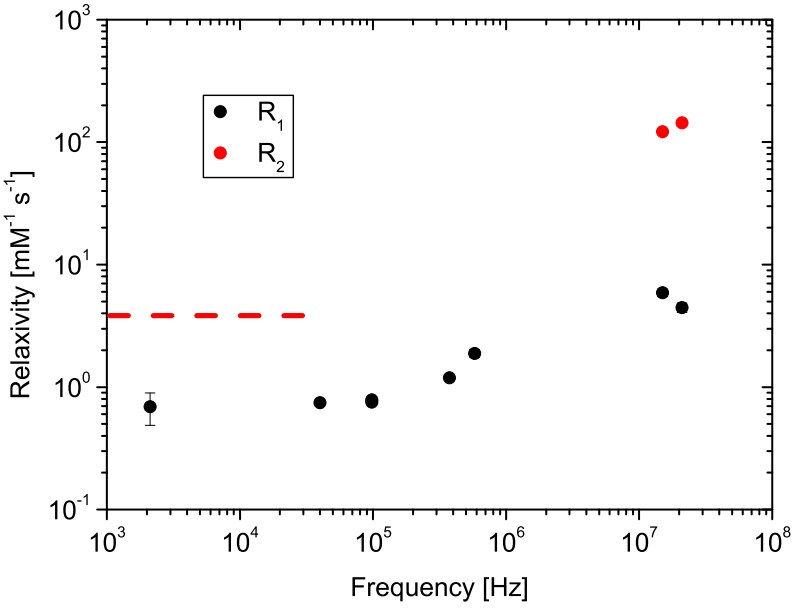

Figure 6.16: Overview of relaxivities measured to date for the KTH nanoparticles.

Figure 6.16 shows all the measured relaxivities for the KTH particles. There is an increase in R_1 above $\sim 200\,\mathrm{kHz}$, which could be an indication of a peak in R_1 between 600 kHz and 15 MHz.

The model described by J. Qin *et al.* could qualitatively explain why R_1 is roughly ten times smaller for the KTH particles than for the fluidMAG-HEAS particles, while R_2 is only smaller by a factor of approximately 3. Maybe this is also the reason why we don't observe $R_1 = R_2$ at low fields.

6.3 Comparison of Theory with Data

We compared the measured relaxation rates for our two samples with theoretical Nuclear Magnetic Relaxation Dispersion (NMRD) curves based on the model outlined in Section 5.2. A good fit of the theoretical equations to the data is unobtainable with the measured/quoted nanoparticle parameters. The best fits in each case were obtained with the parameters listed in Tables 6.3 and 6.4 and are shown in Figures 6.17 and 6.18 for fluidMAG-HEAS and POA@SPION respectively. In both cases, we used $D = 2.14 \times 10^{-9}\,\mathrm{m^2 s^{-1}}$ for the diffusion coefficient of water at room temperature, giving a proton diffusion time τ_D on the order of $1 \times 10^{-7}\,\mathrm{s}$ for the hydrodynamic dimensions used in the fits. We also used the same iron content of 0.61 mM for both samples and consequently the calculated saturation magetization $M = \mu N$ is the same for both sets of parameters. Here, an iron content of 0.61 mM gives $\mu N = 3.66\,\mathrm{Am^{-1}}$ for magnetite particles.

There is some qualitative agreement between theory and measurement. But discrepancies are to be expected given that this simple model ignores possible anisotropy related changes in the Néel relaxation time that could become important especially at low fields and also does not fully take into account any influence that different types of coatings could have on the proton relaxation times.

The curve for fluidMAG-HEAS requires a magnetic diameter that is bigger than both the quoted core size and the average magnetic diameter obtained from the Langevin fit to the magnetization curve. This suggests that similar to the static magnetization measurements, the contribution of a few larger particles has a disproportionate effect on the proton relaxation times, due to the magnetic moment of a particle increasing as the cube of the magnetic radius.

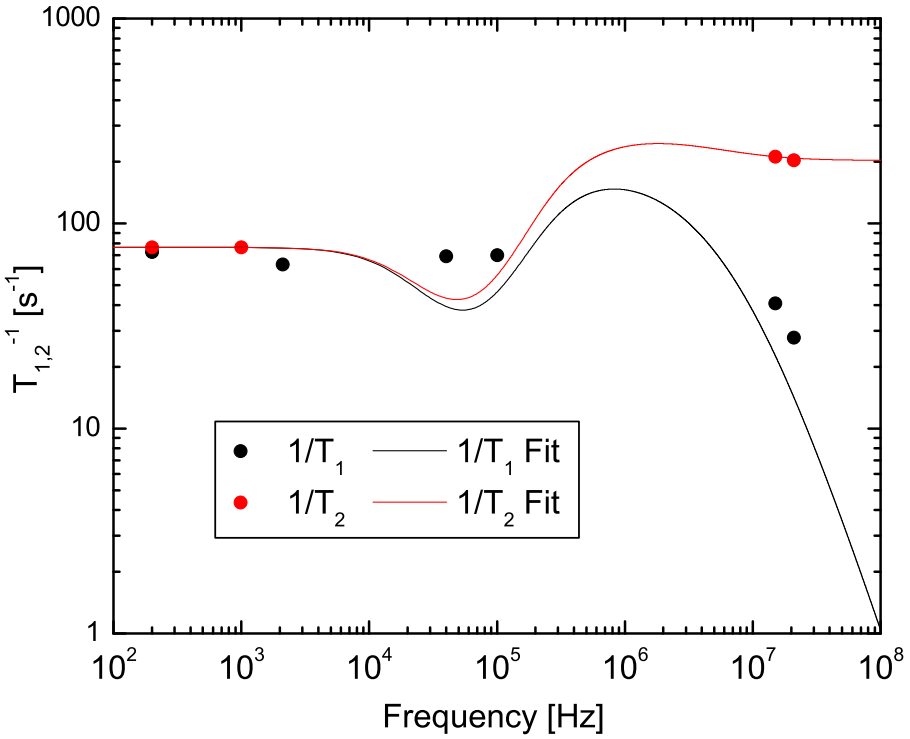

Figure 6.17: Theoretical NMRD curves and measured relaxation rates for fluidMAG-HEAS.

Core diameter, d_M	20	nm
Hydrodynamic diameter, d_H	30	nm
Magnetic moment, μ	1.68×10^{-18}	Am^2
Néel time, τ_N	2×10^{-8}	s
Number density of particles, N	2.18×10^{18}	m^{-3}

Table 6.3: Fitting parameters for the fluidMAG-HEAS curves.

Furthermore, the required hydrodynamic diameter is much smaller than the quoted one confirmed by the PCS measurements. This could be an indication that the proton permeability of the coating might give rise to an additional relaxation mechanism that is not included in the theory. Nevertheless, reasonable curves for both T_1^{-1} and T_2^{-1} can be obtained with one set of parameters.

In the case of the POA@SPION nanoparticles on the other hand, two different hydrodynamic diameters are needed to obtain similar results, since the theoretical curves will always give $T_1^{-1} = T_2^{-1}$ at low fields for a given set of parameters. As mentioned before, this might be due to the properties of the part hydrophobic, part hydrophilic coating. If this is a real effect, then these particular nanoparticles would lend themselves to low-field MRI applications because of the increased R_2/R_1 ratio even at low fields. As a general observation, the measured proton relaxation rates for POA@SPION are smaller than those for the same concentration of fluidMAG-HEAS, which is consistent with what one would expect given that the POA@SPION nanoparticles are thought to have a smaller core size combined with a larger hydrodynamic diameter. This is also reflected by the theoretical curves, where the magnetic moment used for the fluidMAG-HEAS curve is a factor of ten larger than that used for POA@SPION.

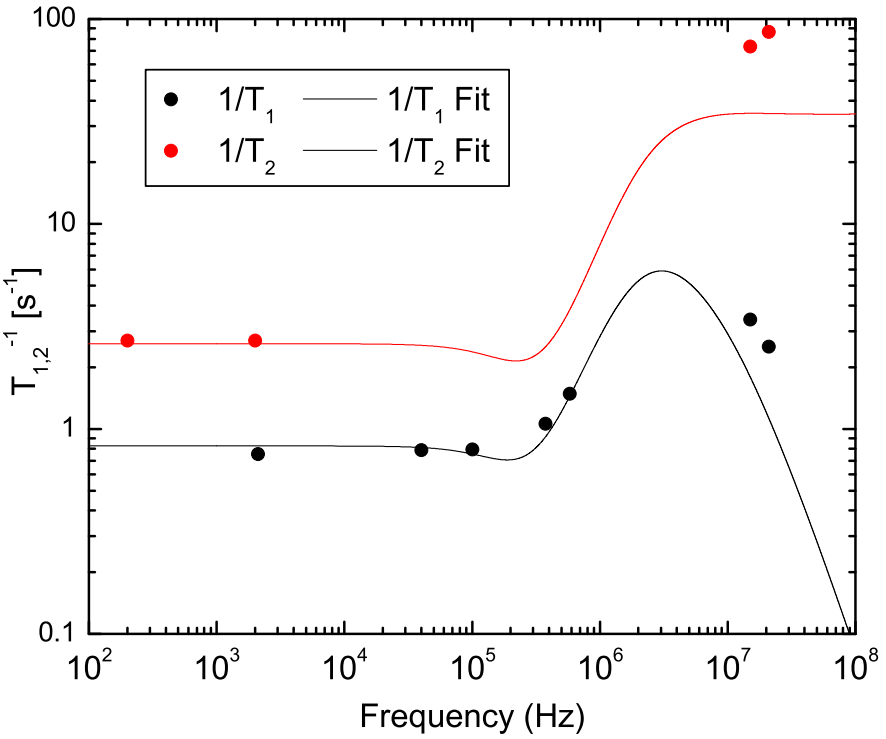

Figure 6.18: Theoretical NMRD curves and measured relaxation rates for POA@SPION.

Core diameter, d_M	10	nm
Hydrodynamic diameter for T_1^{-1}, d_H	33	nm
Hydrodynamic diameter for T_2^{-1}, d_H	22	nm
Magnetic moment, μ	2.09×10^{-19}	Am^2
Néel time, τ_N	1.3×10^{-9}	s
Number density of particles, N	1.75×10^{19}	m^{-3}

Table 6.4: Fitting parameters for POA@SPION curves.

6.4 NMR on Thermally Blocked Cobalt-Ferrite Nanoparticle Solutions

6.4.1 Characterization of fluidMAG-HS/CF Samples

Chemicell provided us with two fluidMAG-HS/CF nanoparticle samples with lot numbers 2607/08 and 2507/08. They consist of cobalt-ferrite ($CoFe_2O_4$) cores with the same hydroxyethyl-starch coating as fluidMAG-HEAS and quoted hydrodynamic diameters of 60 nm and 100 nm respectively. Their core sizes are not specified by the manufacturer, but they have a larger magnetic moment and are thermally blocked at room temperature, so that they undergo Brownian relaxation. As can be seen from the VSM data shown in Figure 6.19, their magnetization behaviour is still superparamagnetic. They are of interest because they exhibit a peak in the imaginary magnetic susceptibility below 1 kHz, see Figure 6.20, which lies within our low-field measurement range. Due to issues with the stability of the fluidMAG-HS/CF solutions when diluted, we were only able to use those nanoparticles with a quoted hydrodynamic size of 60 nm. The properties of fluidMAG-HS/CF lot number 2607/08, as quoted by Chemicell, are given in Table 6.5.

Weight of volume*	125	mg/ml
Number of particles	8×10^{15}	g^{-1}
Density	1.25	g/cm^3
Hydrodynamic diameter	60	nm

Table 6.5: Properties for fluidMAG-HS/CF 2607/08. *Weight of volume corresponds to the weight of dried nanoparticles diluted in a millilitre of solution.

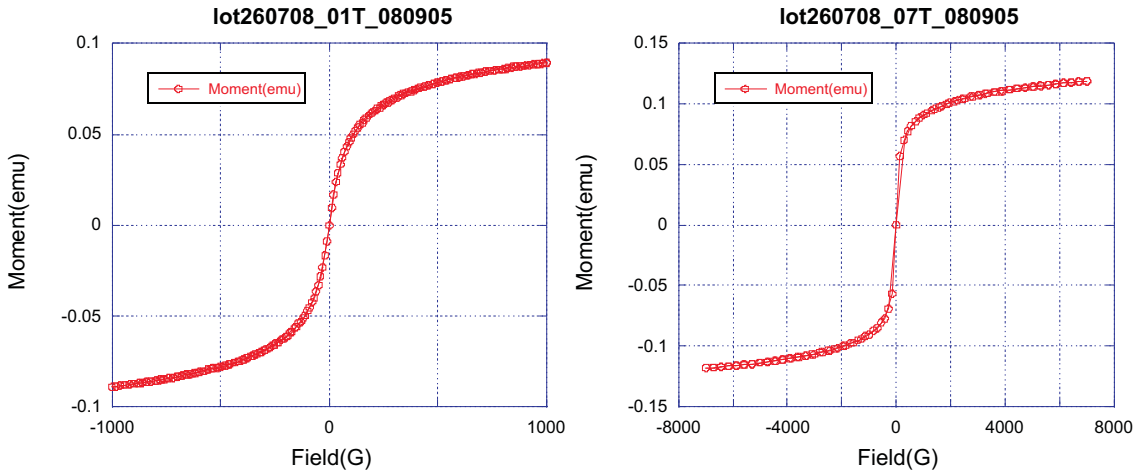

Figure 6.19: Vibrating Sample Magnetometer hysteresis curves of fluidMAG-HS/CF lot number 2607/08 for two different magnetic field ranges.

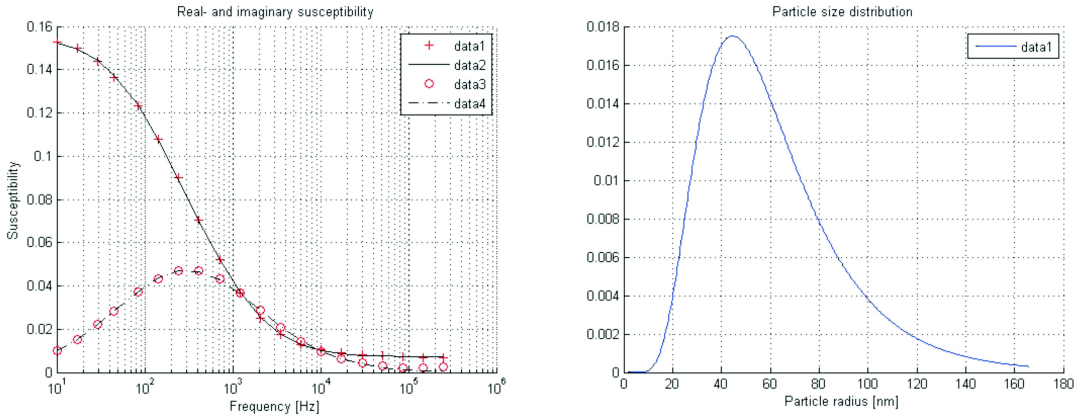

Figure 6.20: AC susceptibility measurements for 60 nm fluidMAG-HS/CF.

6.4.2 Low Field NMR on fluidMAG-HS/CF Sample

We wanted to investigate whether the imaginary susceptibility peak would result in an effect on the proton relaxation times around that frequency. Unfortunately once diluted, the cobalt ferrite particle solutions were not as stable as the previous superparamagnetic samples, even outside of experimental conditions. Furthermore, they became less stable the more dilute the solution. However we were able to measure some relaxation times for higher concentrations. Generally, we found the sample with a hydrodynamic diameter of 60 nm to be more stable than the sample with a hydrodynamic diameter of 100 nm. Measurements of linewidth versus frequency for different averages are shown in Figure 6.21 for a dilution of a factor of 1000 of the 60 nm fluidMAG-HS/CF solution, having a weight of volume of 125 µg/ml. As can be seen in Figure 6.22, no variations of the relaxation times were observed in the vicinity of the peak.

It is possible that no effect is observed, because the nanoparticles are large enough that the system is not in the motionally narrowing regime, meaning that a proton will relax as soon as it moves into the region of strong local field created by the particle, independent of the motion of the nanoparticle's moment. Another possibility is that the susceptibility peak could have shifted to a lower frequency due to agglomeration of the nanoparticles. Because these particles relax via Brownian relaxation, which is dependent on their hydrodynamic volume, their AC susceptiblilty profile can be used to determine their hydrodynamic diameter. As can be seen in Figure 6.20, it exhibits a peak in the imaginary susceptibility at ~ 300 Hz. Using a fitting program on the AC susceptibility measurements to obtain the particle size distribution also shown in Figure 6.20, the mean hydrodynamic diameter is determined to be 94 nm, which is approximately one and a half times the quoted value of 60 nm. If this discrepancy was due to sample deterioration over time, it is conceivable that by the time we performed experiments on this sample it could have agglomerated further.

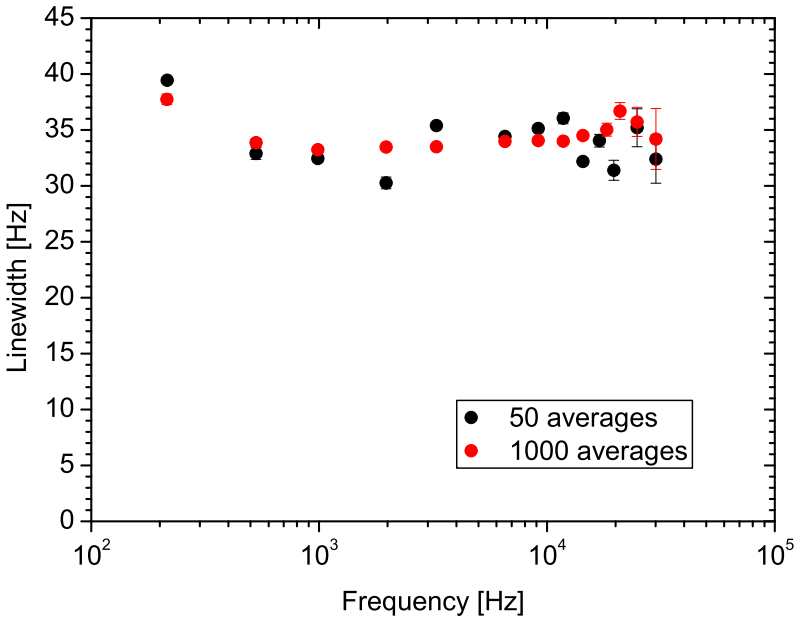

Figure 6.21: Measurements of signal linewidth vs. frequency for 125 µg/ml 60 nm fluidMAG-HS/CF.

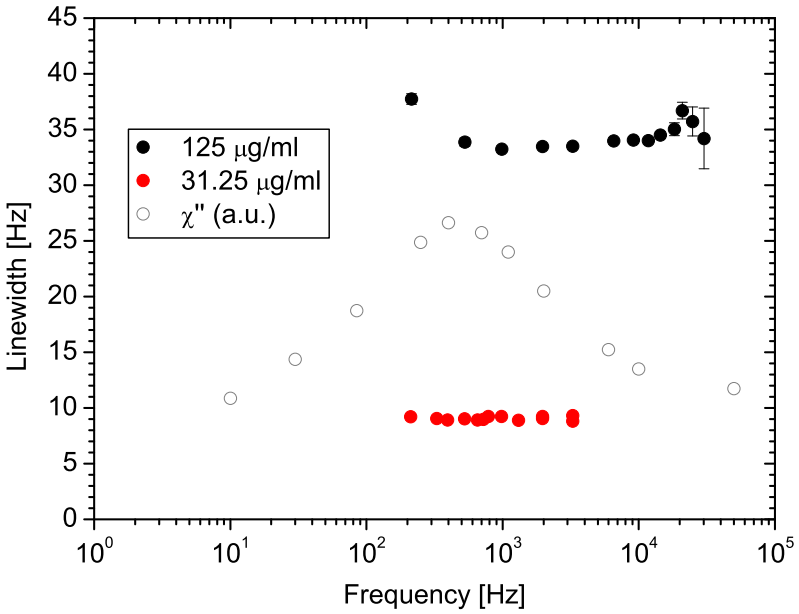

Figure 6.22: Measurements of signal linewidth vs. frequency for two different concentrations with the imaginary susceptibility shown for comparison.

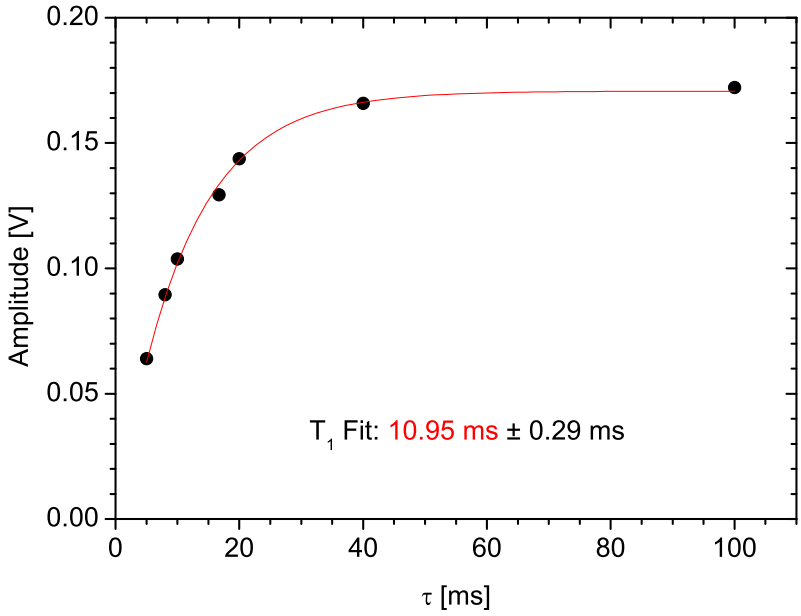

Figure 6.23: 60 nm fluidMAG-HS/CF, 125 µg/ml: T_1 in B_p ($f_0 = 119.3$ kHz).

Because the sample stability deteriorated with decreasing concentration, it was not possible to measure T_1. The signals were broadened too much at the higher concentrations, resulting in T_2s that become too short for our low field measurement techniques, while reducing the concentration to obtain longer T_2s meant that the sample deteriorated too quickly to complete a set of measurements. We nevertheless managed to measure T_1 in the prepolarizing field for the 125 µg/ml concentration solution, see Figure 6.23.

A summary of all the measurements taken for the 125 µg/ml 60 nm fluidMAG-HS/CF solution is shown in Figure 6.24. As for fluidMAG-HEAS, which had the same hydroxyethyl-starch coating, we observe $T_1 \sim T_2$ at low fields.

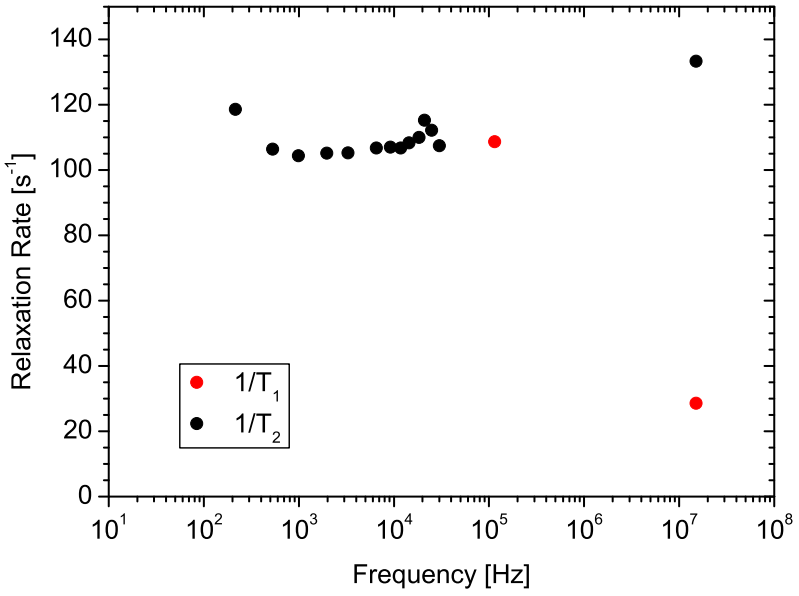

Figure 6.24: 60 nm fluidMAG-HS/CF, 125 µg/ml: Summary of measured relaxation rates.

6.4.3 Predicted T_2 Relaxation Time for fluidMAG-HS/CF

We were looking for a maximum in the relaxation rate at the frequency of the peak in the imaginary susceptibility. As mentioned previously, no such peak was observed in the transverse relaxation rate. A possible reason could be that the system is not in the motional narrowing regime, if the strength of the local magnetic fields is so large that an average proton will flip its spin on a single visit to the vicinity of a nanoparticle. We can test this hypothesis by using the magnetization curves measured by Imego, see Figure 6.19, to calculate the predicted transverse relaxation time T_2 for the static dephasing regime and then comparing it to the measured T_2 at low fields.

But first, let us look at the condition for motional narrowing. We see from Equation 5.14 that the static dephasing limit occurs when $\Delta\omega\tau_D > 1$. We can express $\Delta\omega\tau_D$ as

$$\Delta\omega\tau_D = \frac{\mu_0}{4\pi}\frac{\mu}{r_H D}\gamma \tag{6.4}$$

The quoted parameters of the $CoFe_2O_4$ nanoparticles are given Table 6.5, where the weight of volume of the nanoparticles in solution is given as 125 mg/ml and the number of nanoparticles per gram of dried material is quoted as 8×10^{15}, giving 1×10^{15} nanoparticles per ml or $N = 1 \times 10^{21}\,\mathrm{m}^{-3}$. The average moment μ of a single nanoparticle can be obtained from the saturation moment M_S of the sample, which is measured to be 0.12 emu, equivalent to $1.2 \times 10^{-4}\,\mathrm{Am}^2$ in S.I. units. Since the 50 µl VSM sample contains 5×10^{13} nanoparticles, the average moment per nanoparticle is $\mu = 2.4 \times 10^{-18}\,\mathrm{Am}^2$. Using this value for μ together with the measured hydrodynamic radius $r_H = 47\,\mathrm{nm}$ and $D = 2.14 \times 10^{-9}\,\mathrm{m}^2\mathrm{s}^{-1}$, we obtain $\Delta\omega\tau_D = 0.64$. We are clearly quite close to the static dephasing limit.

We will therefore estimate the expected transverse relaxation rate in this limit. In the static dephasing limit T_2 is given approximately by Equation 5.30

$$\frac{1}{T_2^*} \approx 1.2\Delta\omega f_a$$

where from Equations 5.16 and 5.27 we have

$$\Delta\omega = \frac{\mu_0}{4\pi}\frac{\mu}{r_H^3}\gamma \quad \text{and} \quad f_a = NV_H$$

and therefore $\Delta\omega = 6.18 \times 10^5\,\mathrm{s}^{-1}$. The hydrodynamic volume of the nanoparticles is $V_H = 4.35 \times 10^{-22}\,\mathrm{m}^3$. The original sample of fluidMAG-HS/CF was diluted by a factor of 1000 for the NMR measurements shown in Figure 6.24, such that $N = 1 \times 10^{18}\,\mathrm{m}^{-3}$, which then gives $f_a = 4.35 \times 10^{-4}$.

Substituting everything into Equation 5.30

$$\frac{1}{T_2} \approx 1.2(6.18 \times 10^5\,\mathrm{s}^{-1})(4.35 \times 10^{-4}) = 323\,\mathrm{s}^{-1}$$

we obtain $T_2 = 3.1\,\mathrm{ms}$ in the static dephasing limit. From Figure 6.24 we see that we measured a value of T_2 of 7.5 ms at $f_0 = 15\,\mathrm{MHz}$, with $T_1 \sim 36\,\mathrm{ms}$. Here the measured T_2 is slightly longer than the calculated value in the static dephasing limit and there is very little spectral power at the Larmor frequency available to flip spins. At low frequencies $T_1 \approx T_2 = 9.4\,\mathrm{ms}$ and while we were unable to undertake the necessary measurements as far as the longitudinal relaxation times are concerned, there was no evidence for a change in transverse relaxation times in the region of the peak in the imaginary susceptibility. Despite having determined that we are not quite in the static dephasing regime, this is possibly not surprising since the time taken for a proton to diffuse past a nanoparticle is on the order of $\tau_D = 1.03 \times 10^{-6}\,\mathrm{s}$, whereas the typical time for the nanoparticle to change its spin orientation, which is the inverse of the angular frequency at the peak, corresponds to a Brownian relaxation time $\tau_B = 5.3 \times 10^{-4}\,\mathrm{s}$ for a peak frequency of 300 Hz.

6.5 Summary

Three different types of aqueous solutions of magnetic nanoparticles were investigated by means of proton NMR. These were fluidMAG-HEAS and fluidMAG-HS/CF provided by Chemicell and POA@SPION provided by KTH. The results obtained for each of these samples are summarized below together with their relevant physical properties.

fluidMAG-HEAS consists of magnetite cores with a quoted diameter of 8–10 nm inside a hydroxyethyl-starch polymer coating. Their mean hydrodynamic diameter is measured as 66 ± 2 nm and their magnetization curves confirm that the particles are superparamagnetic, while a Langevin fit to the curves gives an average magnetic moment of $6.76 \times 10^{-19}\,\mathrm{Am}^2$ per nanoparticle, corresponding to a core size of 15.4 nm. This larger than expected average core size together with the poorness of the Langevin fit are evidence of the polydispersity of the magnetic cores in the sample. AC susceptibility measurements show a large proportion of Néel relaxation, but also indicate a broad core size distribution. Initially there were problems with the temporal stability of the sample under low-field experimental conditions, but we eventually managed to keep the sample sufficiently stable with only a slight residual drift in the relaxation times over time that was monitored and compensated for. We see significant broadening of the proton signal linewidth in the presence of the nanoparticles, with T_2s of around 13–14 ms for a diluted sample with an iron content of 0.61 mM. We observed the usual linear behaviour of linewidth vs. frequency due to the magnet inhomogeneity, indicating that T_2 remains constant over the measured range of 1 to 30 kHz. We therefore used the fitted value for $T_2^*(0)$ to calculate R_2 for this low-field range. It is clear that the transverse relaxation rates are much higher than the longitudinal rates at higher fields, but in low fields (< 100 kHz) R_1 increases and R_2 is reduced, such that $R_1 \approx R_2$.

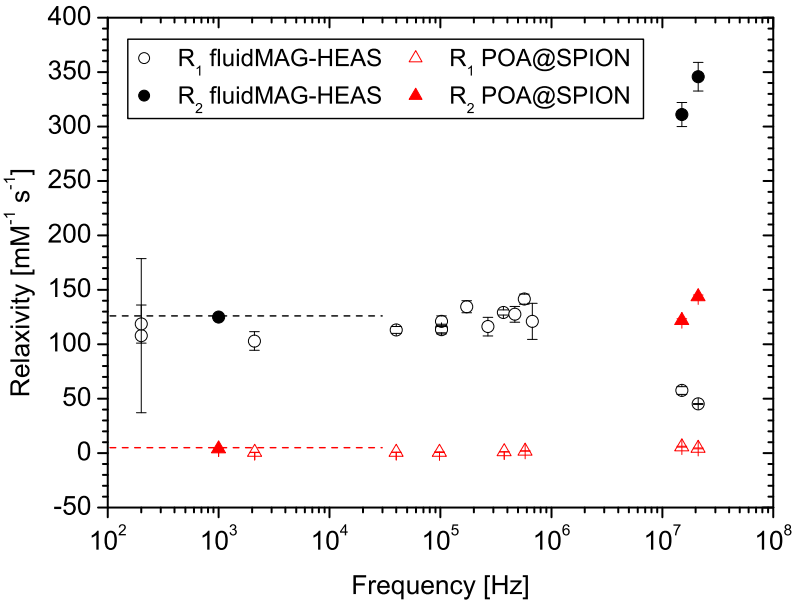

Figure 6.25: Overview of relaxivities for magnetite nanoparticles at an iron concentration of 0.61 mM.

POA@SPION, consists of 7 nm diameter superparamagnetic iron-oxide nanoparticles (SPION) with a PF127/Oleic Acid (POA) polymer coating. PCS gives their mean hydrodynamic diameter as 100 nm. AC susceptibility measurements were similar to those for fluidMAG-HEAS. For a diluted sample with an iron content of 0.61 mM, we measured T_1s on the order of 1.2 s, while the linear T_2^* frequency dependence gave $T_2 = T_2^*(0) = 375$ ms.

Figure 6.25 gives a comparison of all the relaxivities measured for fluidMAG-HEAS and POA@SPION. The relaxivities in general and R_1 in particular are not as high as for fluidMAG-HEAS and also $R_1 \neq R_2$ at low fields. This could possibly be due to the particular polymer coating, as detailed by J. Qin et al. [107]. Since R_2/R_1 is increased, POA@SPION could be of special interest as a contrast agent in low fields. There is also an indication of a peak in the longitudinal relaxivity around a few MHz, which unfortunately lies outside our accessible measurement range.

The relaxation rates measured as a function of frequency for the 0.61 mM iron content solutions of both fluidMAG-HEAS and POA@SPION, were compared to Nuclear Magnetic Relaxation Dispersion (NMRD) profiles based on the theoretical model established in Chapter 5. The nanoparticle parameters that needed to be input into the model in order to give reasonable fits to the data gave further indication of the polydispersity of these nanoparticles and their hydrodynamic sizes.

fluidMAG-HS/CF consists of cobalt-ferrite cores with a measured average magnetic moment of $2.4 \times 10^{-18}\,\mathrm{Am}^2$ inside a hydroxyethyl-starch polymer coating. Compared to the quoted value of 60 nm, fitting to the AC susceptibility measurements determines the mean hydrodynamic diameter to be 94 nm, which is 1.5 times bigger. The imaginary susceptibility part also exhibits a peak at around 300 Hz, due to the Brownian relaxation of the fluidMAG-HS/CF particles. We measure $T_2 \approx 9.4\,\mathrm{ms}$ for a $125\,\mu\mathrm{g/ml}$ weight of volume solution. We did not observe any noticeable effect on the transverse relaxation times near the frequency of the peak in the imaginary susceptibility. A bigger effect might have been expected in the longitudinal relaxation times in the same frequency region. But due to stability issues with the more dilute solutions of this sample, that would have been necessary to measure T_1 at lower fields, we were only able to measure T_1 in the prepolarizing field, where we observed $T_1 \approx 11\,\mathrm{ms}$. Given a more stable sample of Brownian nanoparticles, it should be possible to investigate whether there is a relation between longitudinal relaxation times and the imaginary susceptibility peak.

Chapter 7

Development of Low-Field MRI System

7.1 Introduction

Our next target is to develop a low-field SQUID-NMR imaging system that will allow for larger samples, which can remain directly accessible in the room temperature environment, as previously demonstrated by Seton *et al.* [12] and McDermott *et al.* [18]. This system will use room temperature coils for prepolarizing the sample and for generating the magnetic background field in which the sample is placed. For eventual imaging experiments there will also be room temperature gradient coils. The SQUID sensor and superconducting receiver coil will sit inside a small low-noise Dewar, see Figure 7.12, that will be positioned above the sample. The whole set-up is designed to be operated inside a $1.2 \times 2 \times 2\,\mathrm{m}$ Magnetically Shielded Room (MSR) in order to screen any extraneous fields, including the Earth's magnetic field.

7.2 Magnetic Background Field and Room Temperature Coils

7.2.1 Magnetically Screened Enclosure

Figure 7.1 shows our Magnetically Screened Room (MSR), sold and installed by Amuneal Manufacturing Corporation [108]. It consists of a two layer mu-metal enclosure. Mu-metal is a high magnetic permeability nickel-iron alloy that consists of approximately 75% nickel.

Figure 7.1: Photograph showing the rebuilt magnetically shielded enclosure.

After the MSR was constructed, initial characterization measurements showed the performance of the magnetically screened enclosure to be substantially worse than the expected performance specified by the manufacturer.

One of the possible reasons considered was that the individual panels of the room had not been fitted together well enough, resulting in poor electrical contact between panels. Similarly the door closing mechanism was not only too flimsy, but also ill-fitting, which could explain why the DC field gradients inside the room were worst near the door. Furthermore, the manufacturer purported that some of the mu-metal panels might have been bent or have suffered mechanical shock during their shipment over from the United States, which potentially could have lead to them having decreased magnetic permeability.

The solution offered by Amuneal was to redesign some of the components of the MSR while it was disassembled and the panels were sent to Magnetic Shields Ltd. [109] to be hydrogen annealed once more. After the improved version of the MSR was rebuilt, the same characterization measurements were repeated, the details of which are presented in this section.

We used a triple-axis low T_C SQUID magnetometer from Magnicon [46] and a 3-axis MAG-03MSL100 fluxgate magnetometer from Bartington [43] to characterize the performance of the MSR. The SQUID magnetometer has a quoted system noise of $\sim 30\,\mathrm{fTHz}^{-1/2}$ at 1 Hz and was necessary because the noise floor of the fluxgate is too high to measure the background noise in the MSR, see Figure 7.2. The fluxgate magnetometer, with a quoted system noise of $< 6\,\mathrm{pTHz}^{-1/2}$ at 1 Hz, was used for calibration measurements outside the MSR, where the unshielded SQUIDs in the fibreglass Dewar could not be operated. Figure 7.3 shows a comparison of the noise background in the lab inside and outside the MSR.

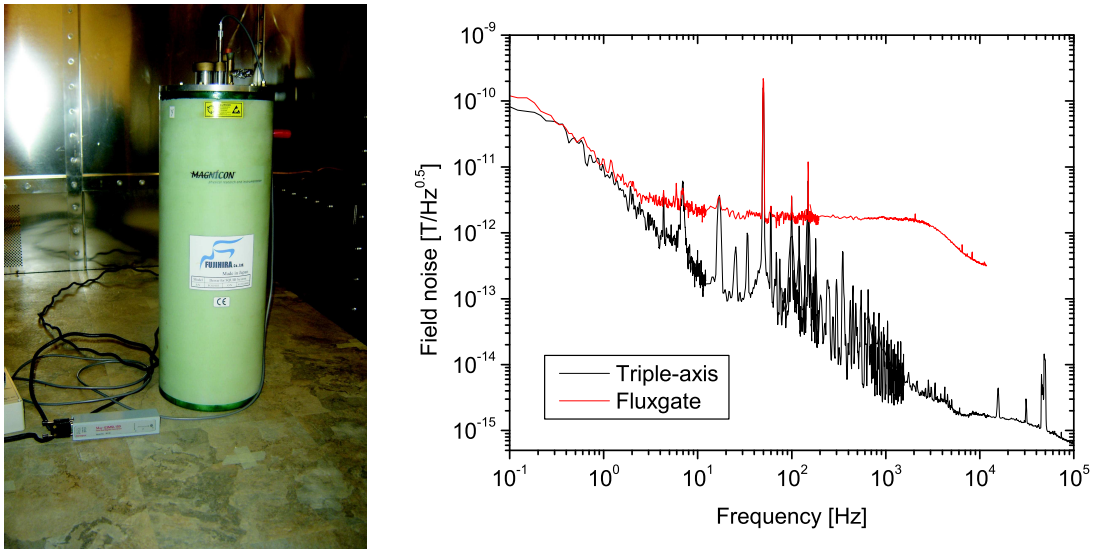

Figure 7.2: Left: Picture of Magnicon Triple-axis SQUID magnetometer inside low-noise Fujihira fibreglass Dewar and Bartington fluxgate magnetometer; Right: Field noise measured in the vertical direction by both instruments at the centre of the MSR, before it was rebuilt.

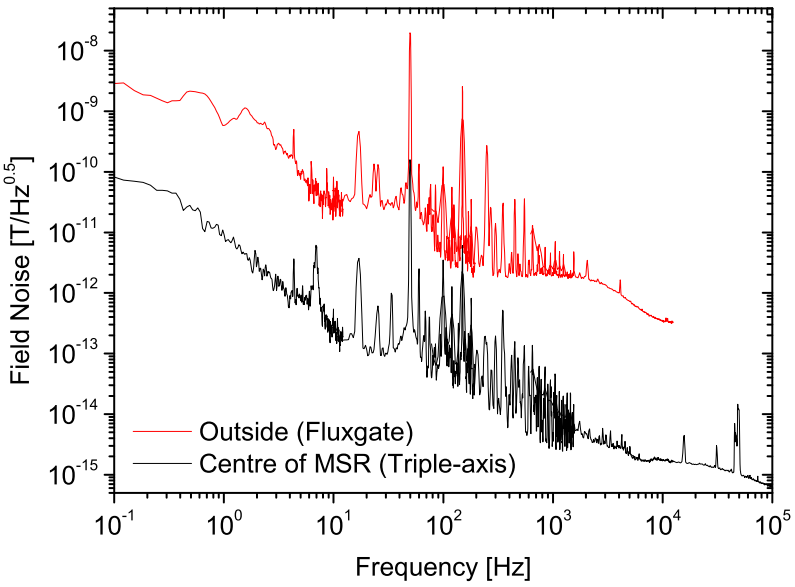

Figure 7.3: Field noise in the vertical direction measured in the W157 laboratory in the centre of the MSR and outside of it, before the MSR rebuild.

Noise Floor and DC Field Gradients

The field noise was measured at the centre of the MSR with the triple-axis SQUID magnetometer, which has a noise floor on the order of 1 fTHz$^{-1/2}$. The results shown in Figure 7.4 are the field magnitudes calculated from the noise spectra measured in all three directions.

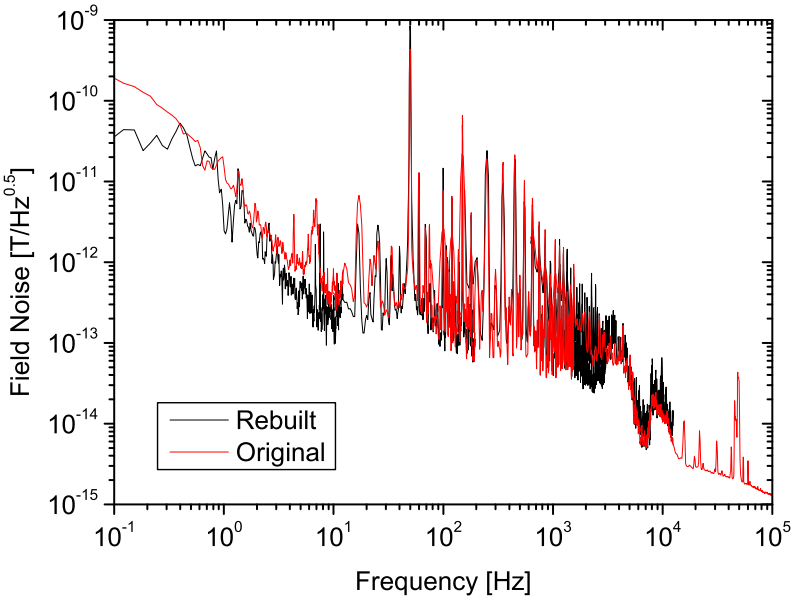

Figure 7.4: Comparison of magnetic field noise in the centre of the MSR, initially and after it was rebuilt.

Even though the triple-axis magnetometer was not cooled down under optimal conditions, the noise spectrum appears to be very similar to that taken before the reassembly of the MSR. The field noise is slightly lower at very low fields ($\lesssim$ 20 Hz). But it still ranges from a few hundred pTHz$^{-1/2}$ to tens of pTHz$^{-1/2}$ in the 100 Hz to 10 kHz range and the pick-up noise is also comparable.

A DC field map of a central 60 × 80 × 80 cm region was made, based on a 3-D grid of fluxgate measurements with a distance between points of 20 cm, the results of which are represented graphically in Figure 7.5.

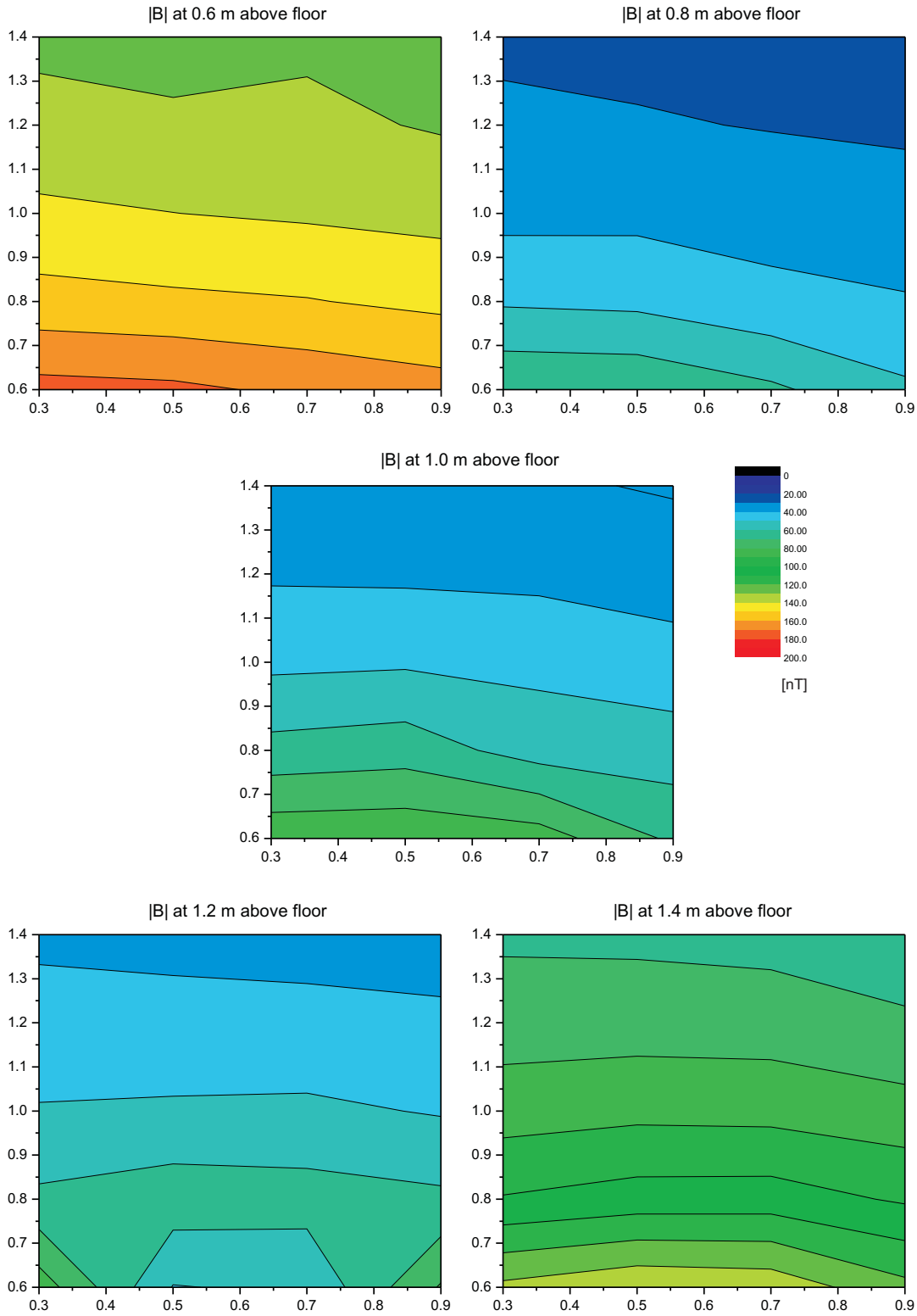

Figure 7.5: DC magnetic field profile slice of central region of MSR as viewed from top. x and y axes are in meters, the origin being the corner with the door lock. The colour scale is in nanoTesla.

The total number of measurements for all three directions was thus 3×100. The magnetic field magnitude was calculated for each point and the resulting field profile was illustrated in the form of 2-D contour plots as viewed from the top of the MSR for different heights above the floor of the room (with the x-axis corresponding to the direction of the door). Previously measured field magnitudes in a central 40 cm cube area ranged from $\sim$ 350–650 nT, whereas they now stay below 100 nT. The colour scale used for the contour plots extends from 0–200 nT, compared with a scale of 100–2000 nT needed previously.

The field-gradients calculated from the data are smallest in the x-direction (across the width of the box), where they can be as low as 60 $\mathrm{pTcm^{-1}}$ at the centre of the MSR, a factor of nearly 12 better than the previously measured field gradients at this position ($\sim$ 750 $\mathrm{pTcm^{-1}}$). Field gradients in the y and z directions (length and height) at the centre are about 550 $\mathrm{pTcm^{-1}}$ and 370 $\mathrm{pTcm^{-1}}$ respectively.

Shielding Performance

The shielding factor of the MSR was determined by pointing a 10-turn, 60 cm diameter copper coil outside the MSR towards its centre and driving the coil at different frequencies to measure the signal getting through to the centre, using either the fluxgate magnetometer or the triple-axis SQUID magnetometer. The measured residual signals were then compared with the corresponding reference signals taken with the fluxgate outside the MSR.

Figure 7.6 shows the best possible shielding performance obtained before the re-annealing of the mu-metal panels (using the SQUID magnetometer) compared with the latest shielding measurements (using the fluxgate magnetometer) and the expected values. For the recent measurements a higher excitation field was used.

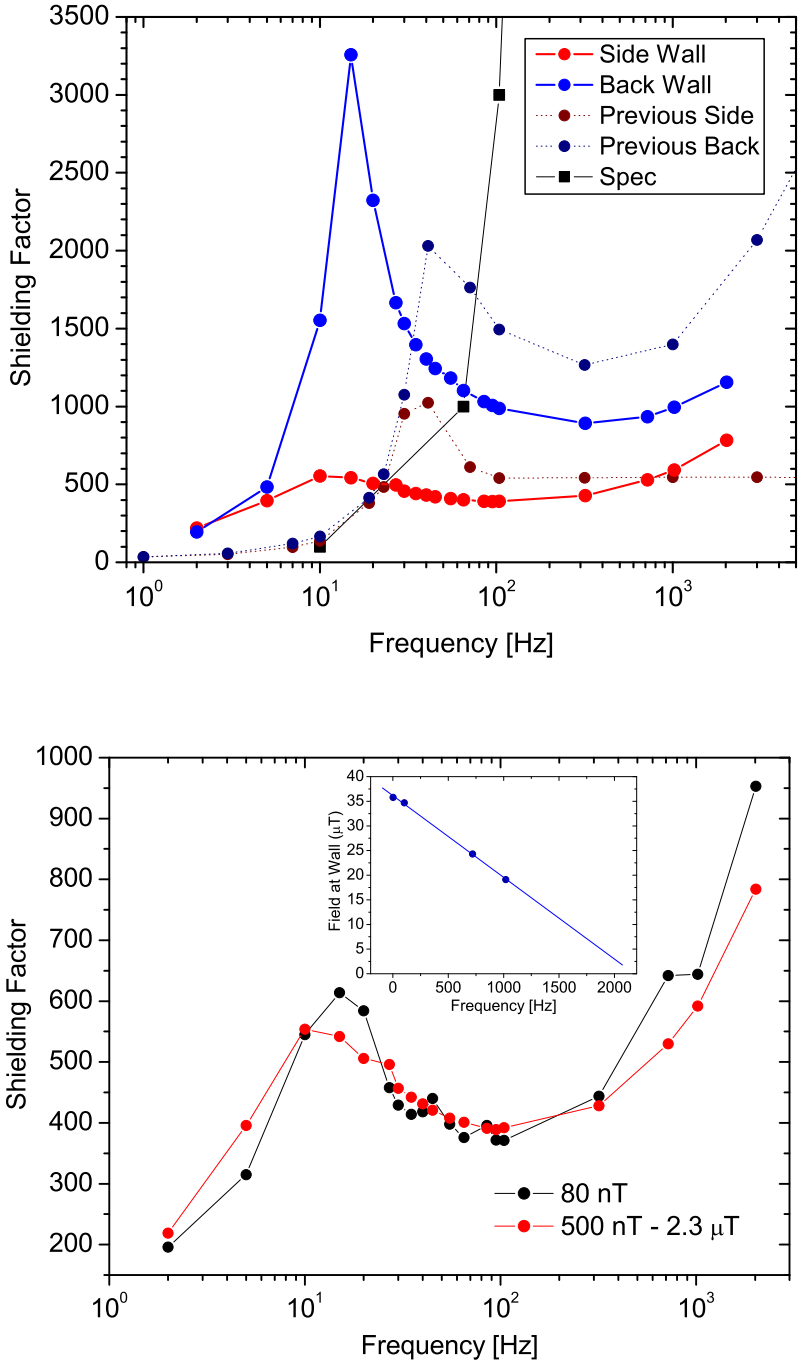

Figure 7.6: Top: Previous shielding performance compared to that of the rebuilt room; Bottom: Shielding measurements at the side wall, 1. SQUID in centre with field of $\sim$ 80 nT at 45.25 inches from coil 2. Fluxgate in centre with fields of 500 nT - 2.3 mT at 45.25 inches. Inset: Field generated by 10-turn coil at a distance of 14.5 inches, *i.e.* the distance between coil and mu-metal wall, as a function of frequency.

There is a substantial improvement at very low frequencies (below 20–30 Hz) where the MSR had already been performing up to, or even exceeding expectations. But in the critical region of a few kHz not much improvement can be seen.

The expected shielding factor at 1 kHz is $\sim$ 30000, while the measured value varies from less than 500 to a little over 1000 at best. A shielding factor of 30000 is only attained at frequencies as high as $\sim$ 100 kHz.

Requirements and Conclusions

It was originally determined that the environmental noise would need to be attenuated by at least a factor of 1000 above 100 Hz to drop below the SQUID noise level. But actually, our laboratory noise levels are quite high and intrinsic SQUID noise levels have become lower, such that the shielding performance of the MSR is insufficient for the intended goal. WL9 SQUID magnetometers have a field noise of 1.2 fTHz$^{-1/2}$ and Fujihira Dewar noise is around 2 fTHz$^{-1/2}$. But we only reach that noise level inside the room at the highest frequencies. The field gradients across the room are much better than before, but this might at least partly be due to the degaussing of the walls. Together with a second-order gradiometer setup connected to the input coil of the SQUID, we should achieve the desired noise levels. With the magnet homogeneity expected to be around 100 ppm, the DC field gradients inside the MSR will be of the same order of magnitude as the background field inhomogeneities at Larmor frequencies around a few kHz. Therefore the DC gradients will set a limit on the achievable signal linewidth at sub-kHz frequencies. This is a rough estimate for a 10 cm wide sample across the width of the MSR, such that the magnet inhomogeneity at the edge of the sample is about 100 ppm (*i.e.* 0.1 Hz at 1 kHz) and the total DC gradient across the sample in that direction is approximately 5 nT.

The smaller the sample size, the higher the frequency at which the DC gradients will start to dominate over the magnet inhomogeneity. The actual sample size and magnet homogeneity, discussed in the following sections, are different.

One possibility to improve the performance of the MSR is to add a third layer made of aluminium. Since we might need to be careful about RF interference, an additional Faraday cage is probably required anyway. The MSR already sits on a 12 mm thick aluminium base plate. Aluminium is more effective at screening higher frequency signals than mu-metal and could therefore bring an improvement in the kHz frequency range. Figure 7.7 shows a simple estimate of the total shielding of the MSR with the addition of an aluminium layer, based on the skin depth as a function of frequency of aluminium. A signal in a conductor will decay exponentially as $e^{-z/\delta}$, where z is the thickness of the plate and the parameter δ is the skin-depth. The skin-depth varies as a function of frequency according to

$$\delta = \left(\frac{2\rho}{\omega\mu_0}\right)^{1/2} = \left(\frac{\rho}{\pi\mu_0}\right)^{1/2} \frac{1}{\sqrt{f}} \tag{7.1}$$

where ρ is the resistivity. For aluminium, take $\rho = 28\,\mathrm{n\Omega\,m}$ [110], such that $\delta(f) = 0.0842 f^{-1/2}[\mathrm{m}]$.

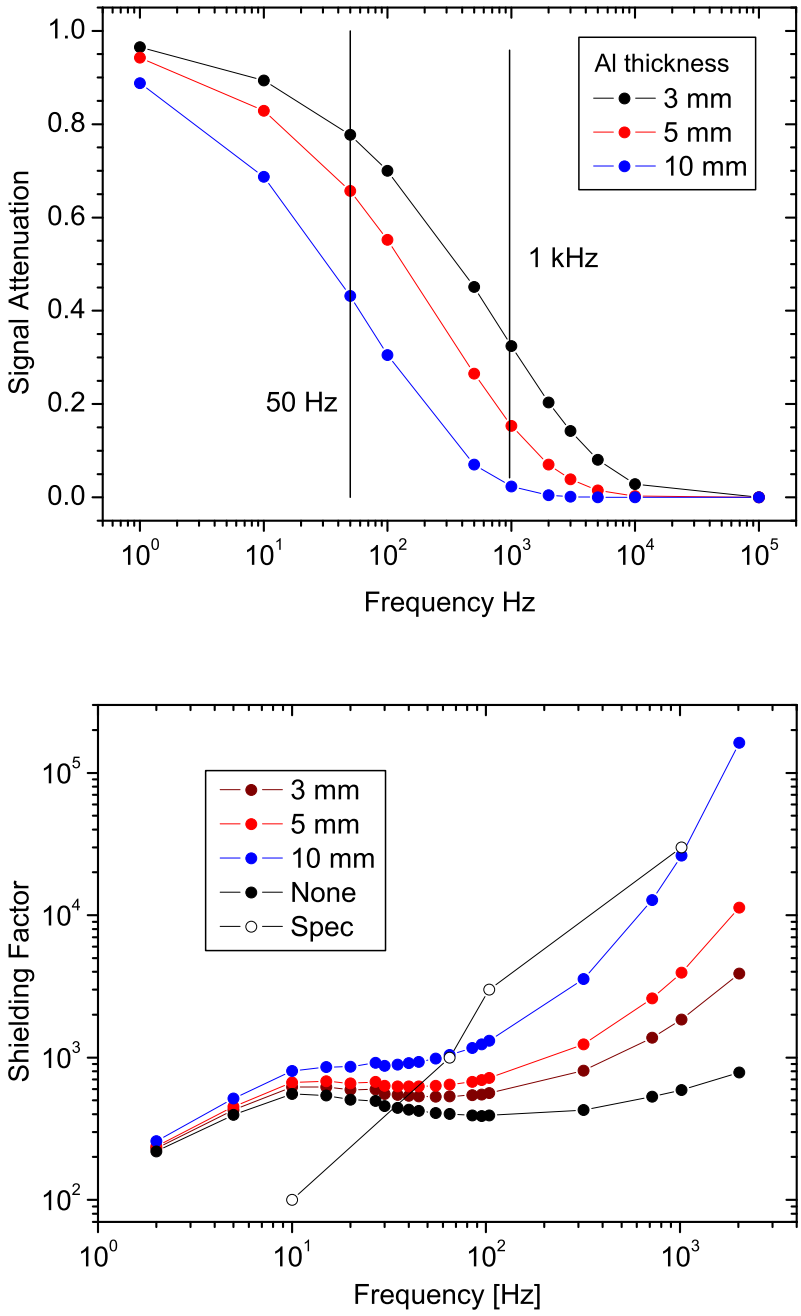

Figure 7.7: Top: Attenuation of electromagnetic signals through aluminium plates of varying thicknesses; Bottom: Effect of additional aluminium screen on MSR shielding performance.

7.2.2 Magnetic Background Field

Two different coil designs were considered for generating B_0 in the new system; a conventional Helmholtz pair and a 4-coil corrected Helmholtz coil system which should offer improved field homogeneity.

Helmholtz-type Four-coil

The axial component of magnetic induction produced by a circular loop of radius a and carrying a current I is given by the Biot-Savart law

$$B_x = \frac{\mu_0 I}{2} \frac{a^2}{(a^2 + x^2)^{3/2}} \tag{7.2}$$

For two identical coaxial loops carrying the same current, optimal field homogeneity is achieved with the Helmholtz configuration, where the distance between the loops is equal to the coil radius $\Delta x = r$. As described in Guendouz *et al.*, for a higher number of loops, there is a general expression to calculate the on-axis field [111], such that for a four-coil system

$$B_x = \sum_{l=1}^{4} \left\{ \frac{\mu_0 I_l}{2 r_l} \sum_{n=0}^{\infty} \left\{ (n+1) \left(\frac{x}{r_l} \right)^n \left(P_n(\cos \alpha_l) - \cos \alpha_l P_{n+1}(\cos \alpha_l) \right) \right\} \right\} \tag{7.3}$$

Here $P_n(\cos \alpha_l)$ are the Legendre polynomials and r and α are given by a line drawn from the centre of the coil system to the edges of the loops, with r being the length of the line and α being the angle between the line and the and the common axis of the coils. For a symmetric configuration, *i.e.* identical inner and outer coil pairs, $\alpha_1 = \alpha_3$, $r_1 = r_3$, $\alpha_2 = \alpha_4$ and $r_2 = r_4$. Even symmetry means that odd-order field derivatives are absent at the centre of the coil system.

If all coils are carrying the same current, *i.e.* $I_l = I$ and defining $X_l = \cos^2 \alpha_l$ (for l = 1,2), the coefficients of the even-order terms (2, 4, 6) are given by the following expressions [111]

$$\frac{3\mu_0 I}{2} \frac{(-1 + 6X_l - 5X_l^2)}{r_l^3} \tag{7.4}$$

$$\frac{15\mu_0 I}{8} \frac{(1 - 15X_l - 35X_l^2 - 21X_l^3)}{r_l^5} \tag{7.5}$$

$$\frac{7\mu_0 I}{16} \frac{(-5 + 140X_l - 630X_l^2 + 924X_l^3 - 429X_l^4)}{r_l^7} \tag{7.6}$$

Setting the 2nd and 4th order derivatives to zero for improved homogeneity and substituting $r = r_2/r_1$, for a spherically symmetric arrangement, *i.e.* $r = 1$, Equations 7.4 and 7.5 simplify to

$$(1 - 6X_1 + 5X_1^2) + (1 - 6X_2 + 5X_2^2) = 0 \tag{7.7}$$

$$(1 - 15X_1 - 35X_1^2 - 21X_1^3) + (1 - 15X_2 - 35X_2^2 - 21X_2^3) = 0 \tag{7.8}$$

Solving these two simultaneous equations for X_1 and X_2 gives: $X_1 = 0.49376$ and $X_2 = 0.04438$. This is equal to an angle $\alpha_1 = 77.84°$ for the inner coil pair and $\alpha_2 = 45.36°$ for the outer coil pair. Note that Equations 7.3 to 7.6 give the on-axis field and its derivatives for a single turn per coil, with every coil carrying the same current. If considering a more sophisticated four-coil set, two additional degrees of freedom can be obtained by varying the current and the number of turns between the two coil pairs, which could potentially result in a further improved homogeneity profile.

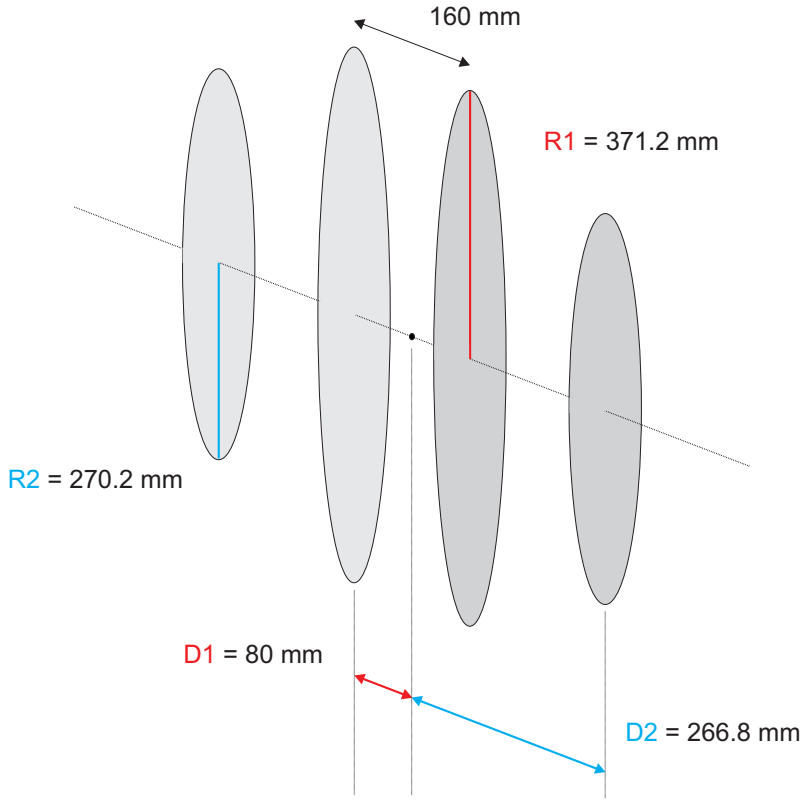

Figure 7.8: Schematic of the compensated Helmholtz test coil.

Because such a coil would be operated inside a shielded enclosure, its dimensions should be as compact as possible in order to minimise the effect of the MSR on the coil. But due to the Dewar dimensions, the distance between the two inner coils needs to be at least 160 mm. Given this minimum distance and the required angles for the two coil pairs, we used the dimensions given in Table 7.1 and illustrated in Figure 7.8.

Coil Pair	Position [mm]	Radius [mm]
Inner	± 80	371.2
Outer	± 266.8	270.2

Table 7.1: Dimensions of test coil.

Calculating the field-current ratio B/I using

$$\frac{B}{I} = \mu_0 N \left\{ \frac{r_1^2}{(r_1^2 + x_1^2)^{3/2}} + \frac{r_2^2}{(r_2^2 + x_2^2)^{3/2}} \right\} \tag{7.9}$$

with the dimensions from Table 7.1 gives $B/I = 4.8542 \times 10^{-6} N$, where N is the number of turns. Winding a coil of 15 layers with 15 turns each, equalling a total of 225 loops, gives a more practical field-current ratio $B/I = 1.09\,\mathrm{mT/A}$. We simulated the resulting field homogeneity of the 4-coil set-up using a solenoid field simulation program [49] and compared it with the homogeneity profile for a simple Helmholtz coil, as shown in Figure 7.9.

We also tried to simulate how the field homogeneity would be affected if the 4-coil was placed inside the MSR. This was done by including counter-current mirror coils on the opposite side and equidistant from the MSR walls, to get the field generated by each coil down to zero at the walls. Since the distance between the side walls and that between the front and back walls is not the same, how much the field homogeneity is affected depends on how the axis of the coil system is oriented with respect to the MSR, as can be seen from Figure 7.10 and Table 7.2.

Simulation	Field in Centre [G]	Hom. @ 5cm [ppm]	Hom. @ 10cm [ppm]
Ideal Four-coil	10.917583	1	-350
Across Width	10.458091	-500	-2500
Across Length	10.827788	-30	-500

Table 7.2: Comparison of field homogeneities for coil system inside or outside of the MSR.

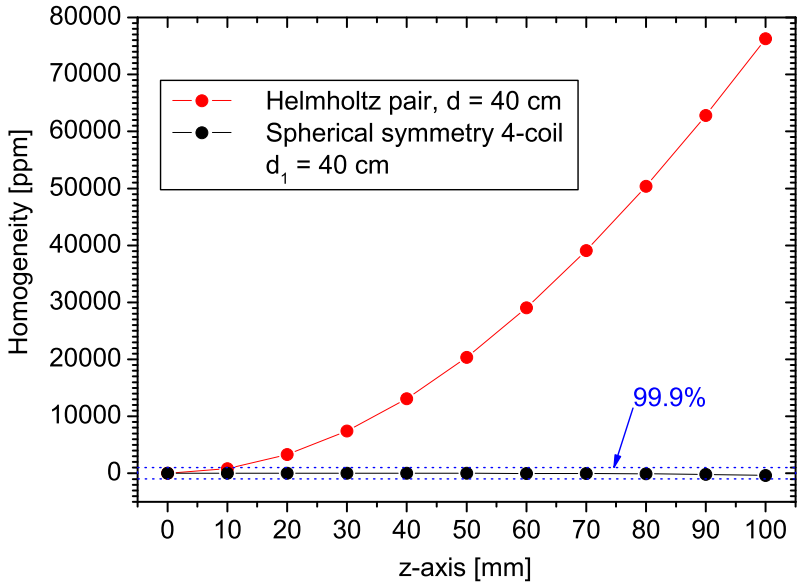

Figure 7.9: Comparison of a simple Helmholtz coil with a similar 4-coil system.

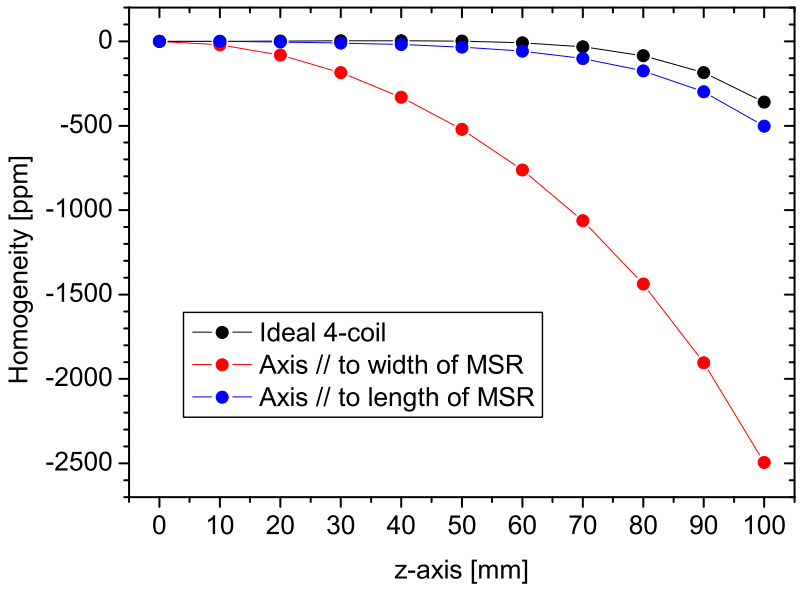

Figure 7.10: Effect on field homogeneity when 4-coil system is placed inside MSR.

Final Design and Parameters of Magnet Coil

Having investigated more practical coil designs for achieving a similar improvement in homogeneity, one possibility is to have the smaller radius correction coil pair at the same position as the Helmholtz-type pair. Since the current in the correction coils would have to be opposite to that in the other pair, this configuration has a lower field-current ratio, but is more compact, which is advantageous for operation inside the MSR. Given that we intend to use a Maxwell pair of the same radius as the Helmholtz-type pair for generating a field gradient in the z-direction, another option is to have the correcton coils at the position of the Maxwell pair. Both alternatives would be more straightforward to build than the original 4-coil test system.

But it will not be necessary to incorporate any corrective coils at this stage, since even for the relatively poor homogeneity of a simple Helmholtz magnet, the limiting factor at low fields turns out to be the higher than anticipated field gradients inside the MSR. The ideal Helmholtz coil performance is achievable if the ratio of the number of turns per layer and the number of layers, for rectangular cross-section dimensions, consists of relatively small integers [112]. Therefore the magnet design that has been decided on is a simple Helmholtz pair with $r = 160\,\mathrm{mm}$, which makes it just wide enough for the fibreglass Dewar, with an outer diameter of 150 mm, to be positioned inside it. It will have 20 windings on each side consisting of 10 turns in 2 layers, resulting in a field-current ratio at the centre of the coil of $B/I = 112.4\,\mu\mathrm{T/A}$. The on-axis homogeneity across a 2 cm sample was calculated to be about 50 ppm using the solenoid simulation program. The magnet former discs will be machined out of Nylon 66, the same material as the supporting frame that will hold the Dewar above the sample. They will be held together at the right distance from one another with tapped fibreglass rods. The part of the support structure directly underneath the low-noise Dewar, holding the sample and polarizing coil, will be made out of Teflon (PTFE), so that it will not give rise to spurious proton signals.

7.2.3 Polarizing Coil

The polarizing coil former will also be machined out of Teflon. The initial polarizing coil will be a split solenoid, as illustrated in Figure 7.11, with 20 turns of 1 mm diameter copper wire per layer and 4 layers on each side, giving a total of 160 turns with an average radius of $\approx 12\,\mathrm{mm}$. This coil has an inductance of $\approx 300\,\mu\mathrm{H}$, giving a time constant of around $200\,\mu\mathrm{s}$ for a coil resistance of $R = 1\text{–}2\,\Omega$. This coil would have a field-current ratio of $B/I \approx 1.2\,\mathrm{mT}$, which when operated with 10 A will provide a prepolarizing field of $B_p = 12\,\mathrm{mT}$. This is only a factor of 3–6 bigger than the polarizing pulses achievable in the previous spectrometer, but here the sample is also about 100 times larger. Therefore this type of polarizing coil should be sufficient for initial testing.

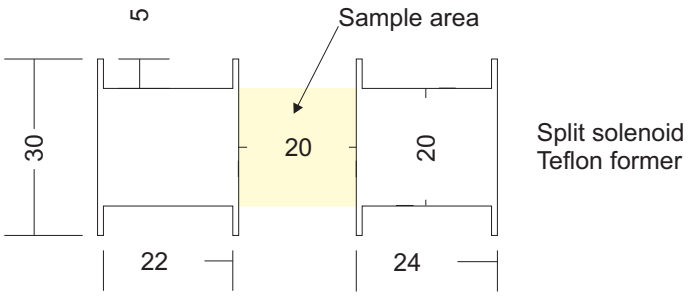

Figure 7.11: Room temperature polarizing coil. Dimensions are in mm.

7.3 Low Noise Dewar and Insert

7.3.1 Low Noise Dewar Construction

Dewar Design

The general design for the low-noise fibreglass Dewar that we were aiming to construct, was originally put forward by Seton *et. al* [113, 13]. The two main innovations in this design were the construction of the vapour shield and the choice of material for the superinsulation surrounding it. Figure 7.12 gives a schematic overview of our Dewar design and the materials used to construct it.

In Dewars that do not use a liquid nitrogen jacket to screen the liquid helium bath from the surrounding room temperature thermal radiation, a vapour shield made from a thermally conductive material is connected to the neck of the Dewar at a position where the evaporating cold helium gas cools it to a temperature somewhere near that of liquid nitrogen. Since these shields are usually made from electrically conductive materials, currents can flow in them and they are therefore a source of noise. In the Seton design the ceramic material alumina is used to construct the bottom of the vapour shield, the bottom being the part surrounding the superconducting receiver coil. Alumina has good thermal conductivity, but is an electrical insulator.

The superinsulation of choice in cryogenic applications is aluminized mylar, which in the Seton design is replaced by aluminized polyester. Again this is to prevent currents from flowing in the thin aluminium layer of the insulating material. Normal aluminized mylar incorporates a more or less unbroken aluminium film, while the fine weave pattern of the polyester textile creates natural breaks in the aluminium layer. The noise due to aluminized mylar can be greatly reduced by crumpling it to break up the aluminium film on the mylar.

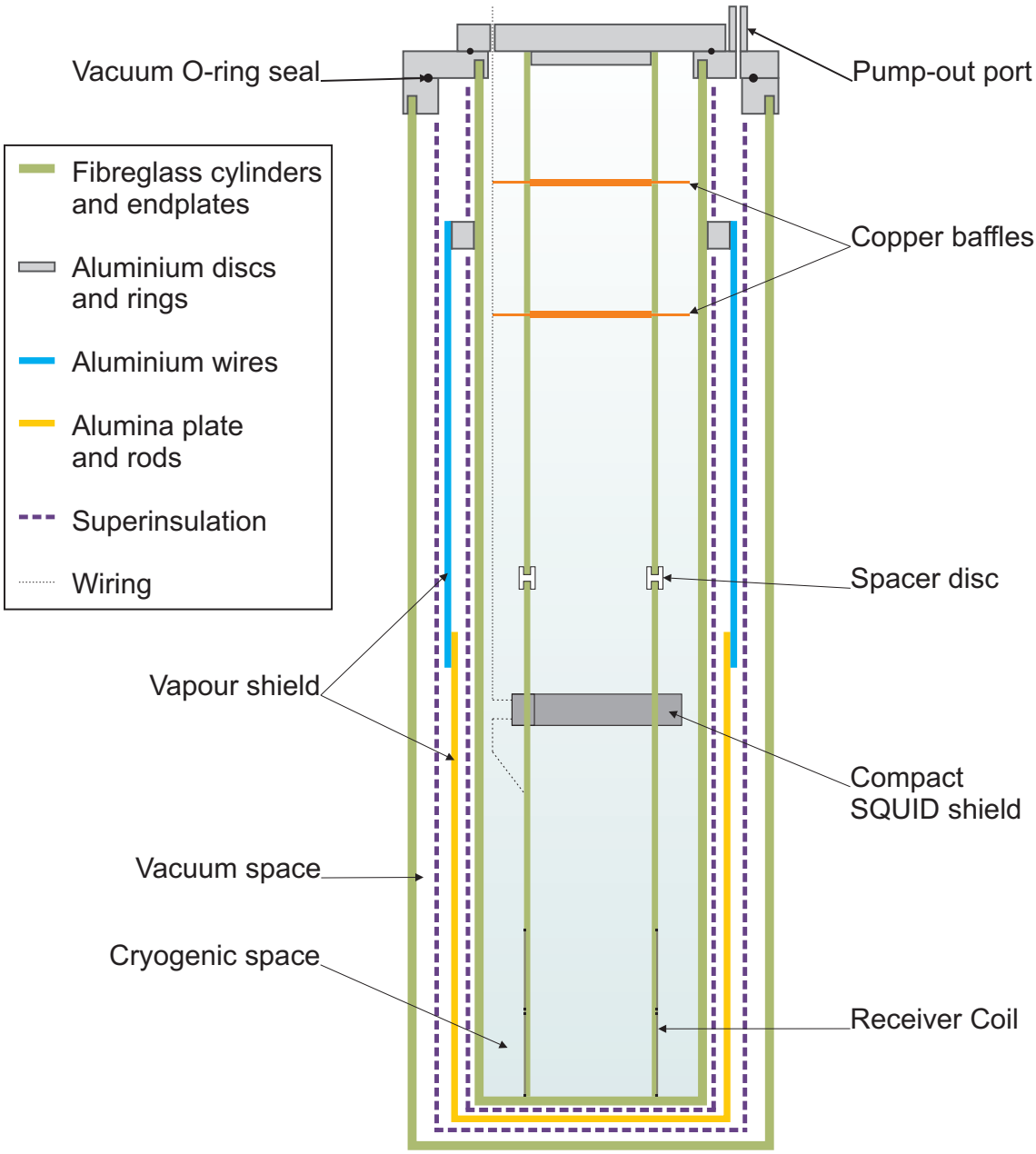

Figure 7.12: Schematic overview of the fibreglass Dewar and the experimental insert.

Figure 7.13 shows SQUID noise measurements for different superinsulation samples that were taken using our low-field dipper probe inside the mu-metal shielded Dewar. The aluminized mylar used was NRC-2, obtained from OIDirect Cryospares [114], which was coated with a 250 Å thick layer of aluminium on one side only. While the white noise level is elevated by a factor of two for the aluminized mylar sample, it drops back down to the baseline noise level for the crumpled aluminized mylar sample. Given that the improvement in the environmental noise inside the MSR is probably not substantial enough to observe a difference in noise, it was decided to use crumpled aluminized mylar as superinsulation, because it was easier to procure.

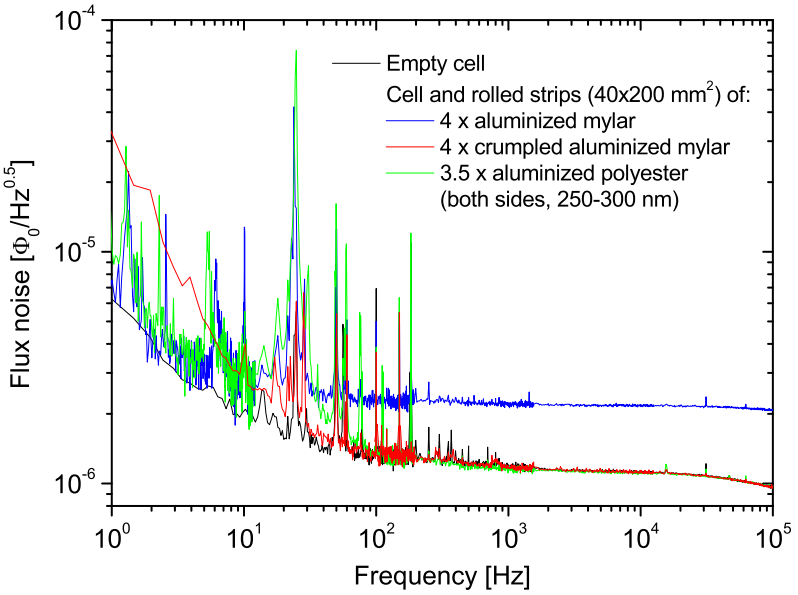

Figure 7.13: SQUID noise with different insulating materials at 4.2 K in pick-up coil measured inside the mu-metal shielded Dewar. The aluminized polyester tested here was taken from sample material provided by Hugh Seton.

The bucket style design of the Dewar is based around two G10 fibreglass cylinders aquired from Langtec [115] as grade LTG475. The smaller one has an inner diameter of 100 mm with a wall thickness of 3 mm and serves as the inner vessel, *i.e.* the cryogen storage space of the Dewar. The bigger cylinder with an outer diameter of 150 mm and a wall thickness of 5 mm, provides the outer surface. The cylinders are capped at the bottom with two custom made fibreglass endcaps, also provided and machined by Langtec. They are made from G10CR, a fibreglass grade that is proven for use in a cryogenic environment, in order to ensure that the discs do not delaminate at low temperatures. The drawings for the endcaps are shown in Figure 7.14. They were designed with the forces put on the fibreglass joints by the vacuum in between the two vessels in mind.

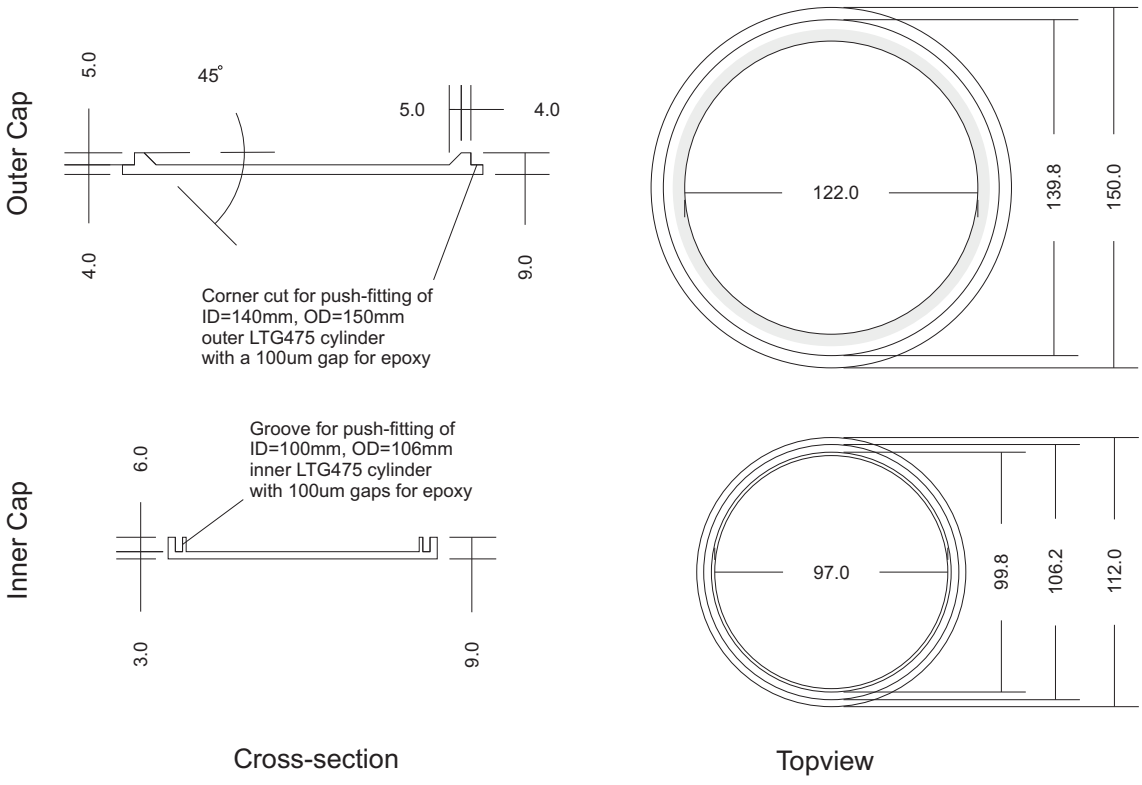

Figure 7.14: Technical drawing of the G10CR fibreglass endcaps.

The top of the Dewar, comprising the vacuum jacket seals, consists of two aluminium rings with an outer diameter of 165 mm that each have a groove to take one of the two fibreglass cylinders. These two rings sit concentrically on top of each other and have the main O-ring seal to the vacuum jacket in between them. The O-ring groove is cut into the bottom ring and designed to take an O-ring with an inner diameter of ID = 5.484 in and a cross-section of d = 0.139 in. The thickness of the rings and the depths of their cylinder grooves are such that the gap between the two fibreglass buckets at the bottom will be as small as possible. The bottom ring is about 12 mm thick and the top ring is about 10 mm thick. The pump port for the Dewar jacket is fitted into the top aluminium ring by means of a screw joint that is sealed with Stycast 2850. The aluminium pump port is sealed via a simple push plug with two O-rings.

The cryogen containing space of the Dewar is closed off by a 10 mm thick aluminium plate that is 130 mm across and sits on the top aluminium ring that also holds the inner fibreglass bucket. The seal between the top plate and ring below is again made with an O-ring that sits in a groove at the bottom of the top plate and has dimensions of ID = 3.987 in and d = 0.103 in. The top plate has a circular recess at one point to allow space for the pump port set into the ring below. This top plate also provides the base plate onto which the NMR detection insert is screwed and has all the necessary feedthrough holes and ports, see Figure 7.15. The design of the insert support structure is based around a third LTG475 fibreglass cylinder, also from Langtec, having an outer diameter of 65 mm and a wall thickness of slightly over 3 mm. The adaptors designed to screw into the top plate are all machined from aluminium. They include a recovery port with two connectors, including one for safety, a fill line and a level meter port, as well as two KF-16 flanges, one for the SQUID electronics connection box and a spare one for an additional Fischer connector if needed. All five adaptors can be seen in Figure 7.17 (a).

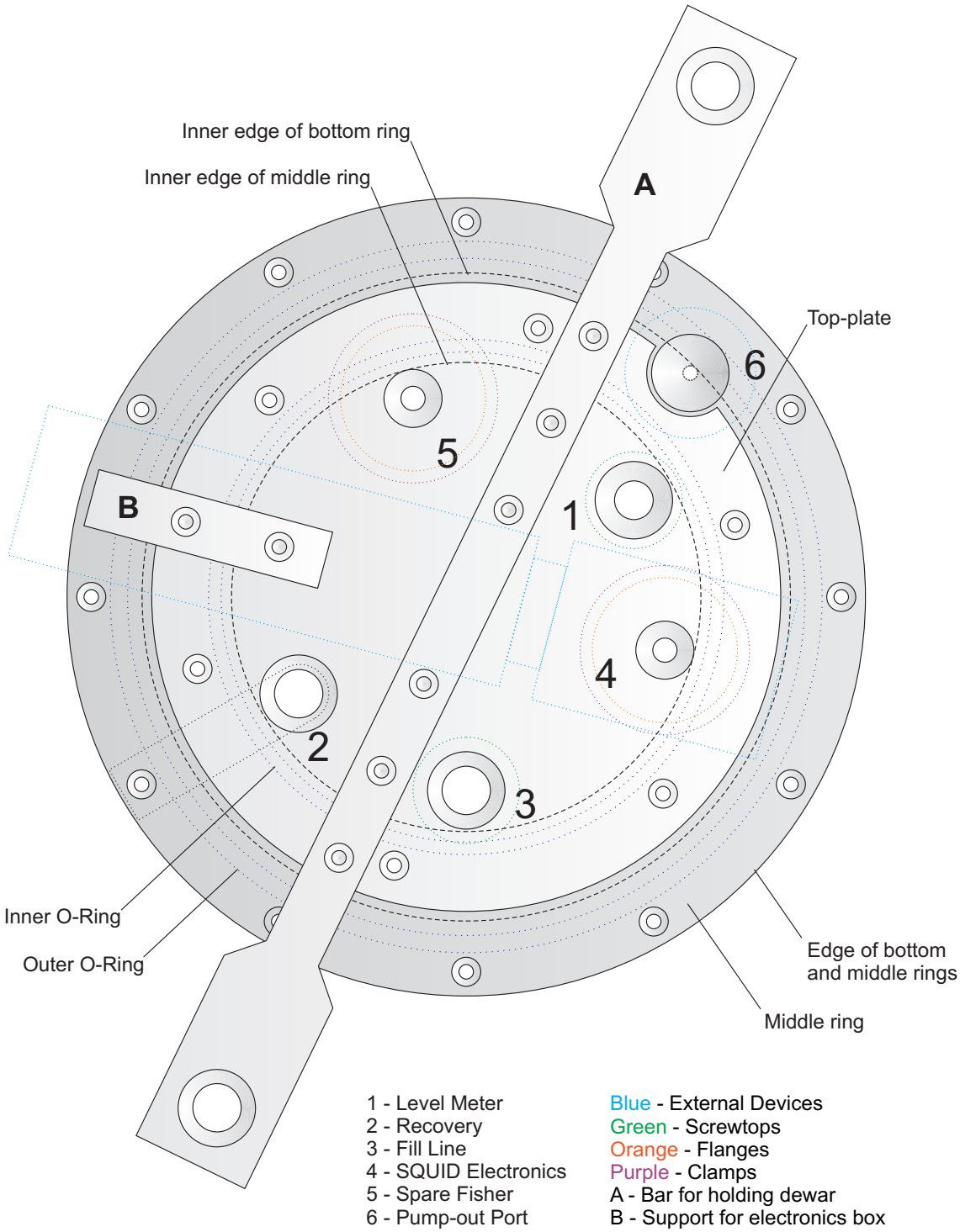

Figure 7.15: Schematic of the top of the Dewar, showing the three aluminium plates.

Dewar Assembly

Stycast 1266 was used for the fibreglass to fibreglass joints between the two fibreglass cylinders and their endcaps. The fibreglass surfaces were prepared by first cleaning them with ethanol and then scratching them with a needle file for better adhesion. The epoxy was subsequently painted on the surfaces after having been pumped on for 30 minutes. After pushing the cylinders onto the endcaps, the assembled buckets were left to cure over night. Stycast 2850 was used for the fibreglass to aluminium joints at the top of the Dewar. The procedure in this case was the same as for the fibreglass to fibreglass seals. The fibreglass buckets with their aluminium tops are shown in Figure 7.17 (c).

Before using the epoxy resins to glue together the actual Dewar parts, a small test piece was machined to check whether the performance of these seals would be sufficient for use in a cryogenic environment. This test piece consisted of two 20 mm long pieces of the fibreglass cylinder material with an outer diameter of 65 mm and two 10 mm thick aluminium plates with a diameter of 70 mm. The plates each have a 5 mm deep groove to fit the cylindrical fibreglass pieces into and one of the plates also has a 1 mm clearance hole into which a pumping line is set with Stycast 2850. The four pieces are glued together, with Stycast 2850 used between the fibreglass and aluminium plate pairs and Stycast 1266 connecting the two fibreglass pieces on their free edges, to form a leaktight cylindrical space that can be pumped out via the fill line in the top aluminium plate, as shown in Figure 7.16. The test piece was pumped out with a leak detector and then exposed to helium gas to check for leaks. No observable increase in the helium background was observed, not even a diffusive response. The same check was repeated after immersing the test piece in liquid nitrogen with equal results. Finally the test piece was lowered into liquid helium and the leak rate still remained unchanged. Having completed the testing of the Stycast seals successfully, the glueing of the Dewar went ahead.

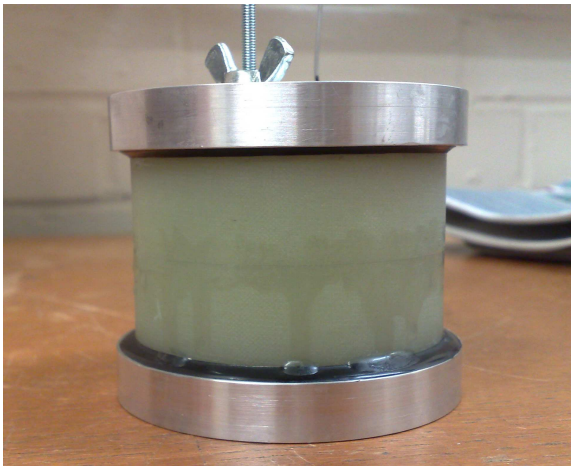

Figure 7.16: Photograph showing the fibreglass and aluminium cell used for testing the strength of the stycast seals.

The aluminium components that make up the top of the Dewar are pictured in Figure 7.17 (a). They were all hard-anodized at Jackson Plating Ltd. [116] to prevent oxidation and corrosion of the aluminium due to the stainless steel screws and thermal cycling. Figure 7.17 (b) shows the fully assembled and anodized top plate with the SQUID electronics connected to a shielded room temperature connection box that is fitted onto the designated flange adaptor. The top plate adaptors are simply screwed in with PTFE tape on their threads. Some silicone sealant around the top of the screw seals serves to keep the PTFE tape from peeling away. Figures 7.18 (e) and (f) show the finished Dewar, with the vapour shield (described further below) in place and the vacuum space closed off, being pumped on and during one of the first liquid helium transfers respectively.

Vapour shield

Originally, a third fibreglass cylinder was going to be used as a former for the alumina-aluminium vapour cooled radiation shield, but Langtec had none available in a suitable size, *i.e.* having the right diameter and a sufficiently small wall thickness. Instead the vapour shield components were set to be self-supporting.

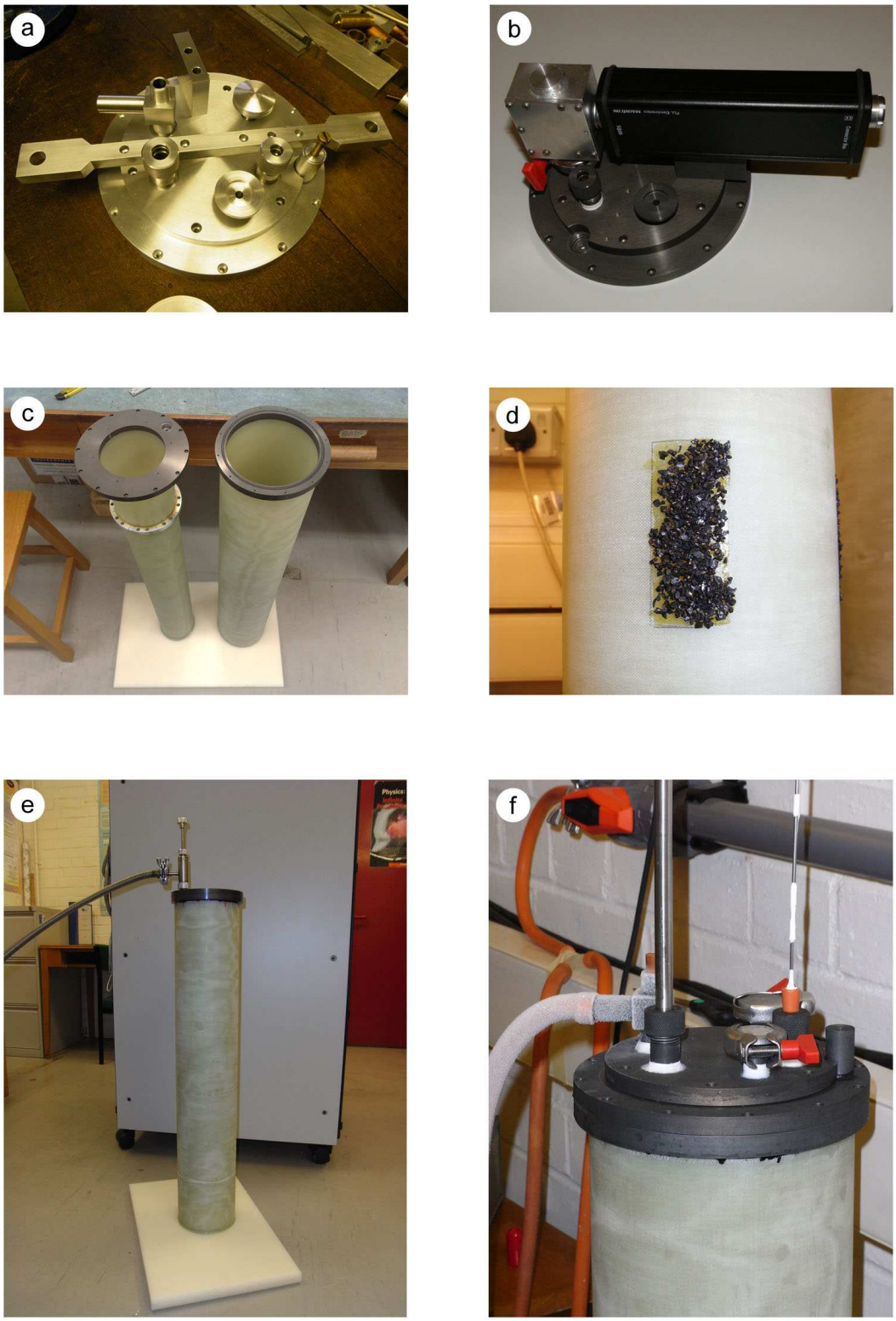

Figure 7.17: Low noise Dewar parts. (a) Un-anodized aluminium components, (b) anodized top plate with SQUID electronics fitted, (c) inner and outer fibreglass buckets with aluminium rings glued on, (d) charcoal granules on inner fibreglass bucket, (e) pumping on Dewar jacket and (f) transferring liquid helium into the finished Dewar.

The bottom part of the shield consists of approximately 370 alumina rods having a diameter and length of about 1 mm and 30 cm respectively. They were arranged with their ends aligned and perpendicular to the edge of sheets of A4 paper and held in place using double-sided tape, such that they formed a sheet that was then rolled up into a cylinder with an outer diameter of $\sim$ 128 mm. This cylinder was glued together and onto a 1 mm thick alumina disc, measuring 128 mm across and serving as the vapour shield baseplate, with Stycast 1266 epoxy resin. The finished bottom part is shown in Figure 7.18 (a). For the top part of the vapour shield, around 360 pieces of 45 cm long aluminium wire were used. Each single one was straightened by hand and stuck down onto pieces of paper with double-sided tape to form sheets that were then assembled on a former into a cylinder with a diameter of $\sim$ 130 mm and set using Stycast 1266. The top and the bottom of the vapour shield were then glued together, again using Stycast 1266, with an overlap of 3–5 cm.

A 10 mm thick aluminium ring with an outer diameter of 125 mm was varnished onto the inner fibreglass cylinder (prior to attaching the aluminium top) at roughly 12 cm from the top, see Figure 7.17 (c), to act as a heat exchanger and anchoring point for the vapour shield. Its inner diameter was such that it gave a tight fit to the fibreglass cylinder (with an outer diameter of 106 mm) and it had 16×6 mm holes machined through it, in order to make it easier to pump on the internal vacuum space later on. After varnishing some charcoal onto the inner cylinder, see Figure 7.17 (d), as a cryo-pump for exchange gas in the vacuum jacket, the inner vessel was wrapped in approximately 14 layers of aluminized mylar superinsulation, with plain polyester in between, as shown in Figures 7.18 (b) and (c). The previously completed vapour shield was then varnished to the aluminium ring at the neck of the Dewar, as pictured in Figure 7.18 (d). Figure 7.18 (e) shows the vapour shield in place with some additional superinsulation wrapped around the top of the inner fibreglass vessel. Finally, the outer superinsulation layers were put on, as shown in Figure 7.18 (f), before inserting the whole construct into the outer fibreglass vessel.

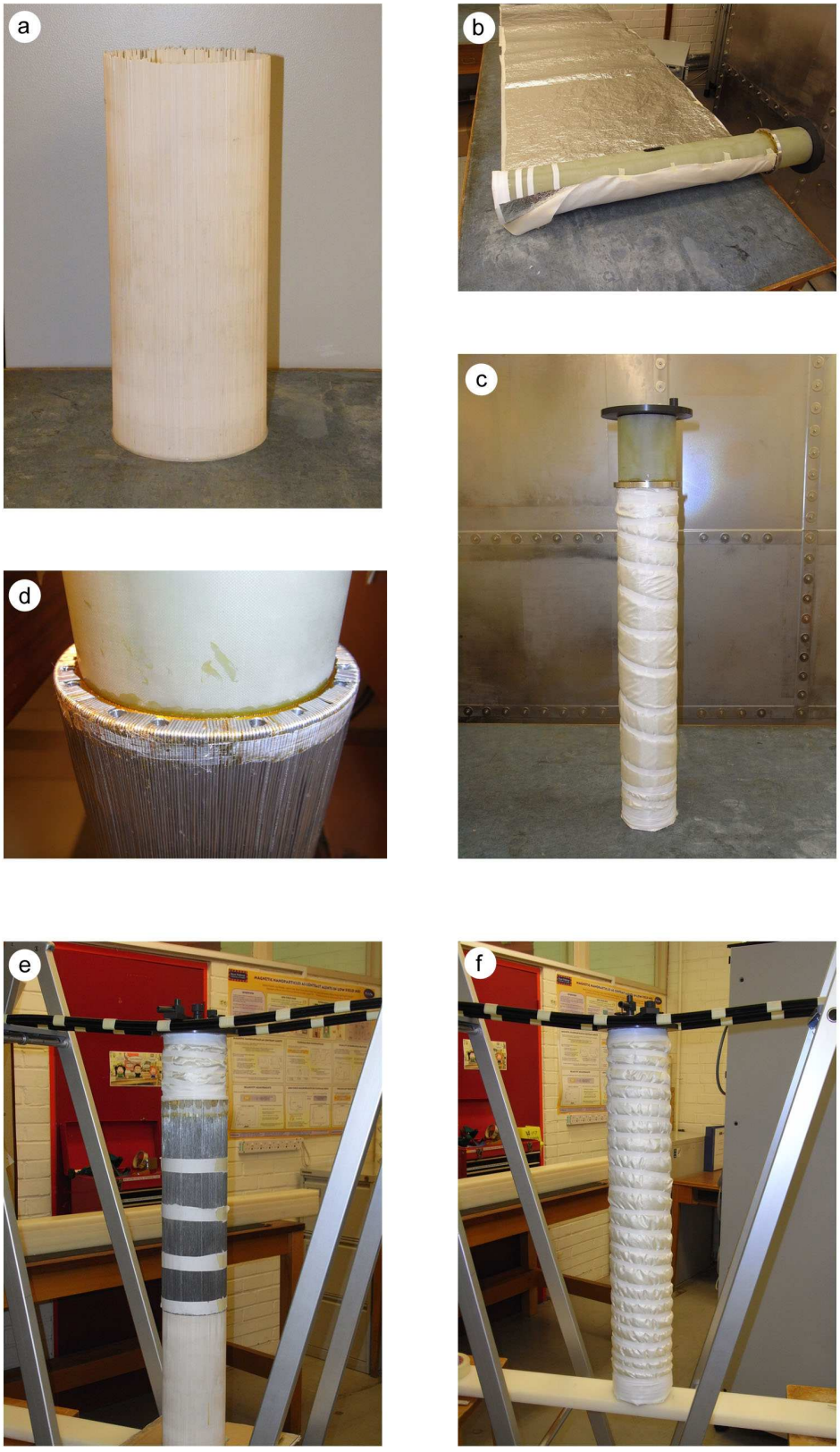

Figure 7.18: Assembly of the low noise Dewar vacuum space. (a) Alumina part of vapour shield, (b) wrapping of inner insulation, (c) inner insulation in place, (d) vapour shield thermal link, (e) top of inner insulation in place and (f) outer insulation in place.

7.3.2 SQUID and Receiver Coil Insert

Figure 7.19: Photograph of the fibreglass insert attached to the aluminium top-plate. The receiver coil wiring and SQUID sensor are not yet included.

The initial design of the SQUID insert is based around four fibreglass cylinder segments of the same grade as the two structural cylinders, with an outer diameter of 65.5 mm and a wall thickness of 3 mm. The 400 mm long bottom segment is the longest. It is screwed onto the 200 mm long segment above it with nylon screws through a Teflon connector ring. The top of the insert consists of two 100 mm long segments, each holding one 1 mm thick copper baffle below it, which are all glued together and onto the top of the 200 mm long segment with GE varnish. Figure 7.19 shows a picture of the assembled insert. Rings of high-density foam are put on top of the baffles in order to route the cold helium gas to the walls of the inner fibreglass vessel and thus cool the vapour shield more effectively.

A number of 28 mm wide holes, arranged in a spiralling fashion, were drilled into each of the segments in order to break potential vibrational modes in the cylinders and to prevent Taconis oscillations that could otherwise lead to increased liquid helium boil-off rates. The bottom cylinder has the grooves for the windings of the receiver coil. It also has corresponding holes on opposite walls at different depths from its top, that are designed to take the SQUID sensor inside its cylindrical niobium shield, which will be held in place by screwing it onto a semi-circular Teflon plate that is screwed to the inside of the fibreglass cylinder. The SQUID and receiver coil are kept on the same fibreglass segment to protect the receiver coil wiring in case the bottom were to drop off accidentally while handling the insert. The copper wiring between the room temperatute electronics and the SQUID runs through a Fisher connector that plugs into the SQUID shield. The SQUID used here will be another Two-Stage device, model number C519-B22, that has already been tested.

Gradiometric Receiver Coil

The receiver coil will consist of a second order, single turn gradiometer, see Figure 7.20, with a 150 mm baseline and a loop diameter of 65 mm.

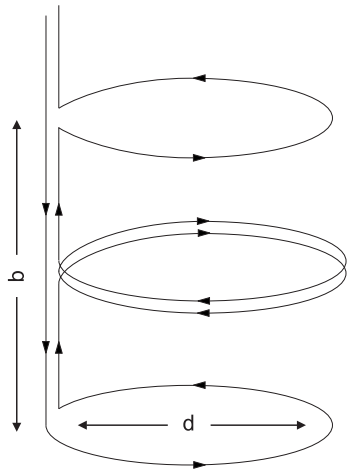

Figure 7.20: Schematic of a second order gradiometric receiver coil configuration with baseline b and pick-up loop diameter d.

The inductance of a single loop of the gradiometer is given by [117]

$$L = a\mu_0 \left[\ln\left(\frac{8a}{b}\right) - 2 + \frac{1}{4}\mu' \right] \tag{7.10}$$

where a is the loop radius, b is the radius of the wire and $\mu' = 0$ for a superconducting wire. For the above coil $a = 32.5 \times 10^{-3}\,\mathrm{m}$ and $b = 25 \times 10^{-6}\,\mathrm{m}$ for $50\,\mu\mathrm{m}$ superconducting niobium wire, giving $L = 2.96 \times 10^{-7}\,\mu\mathrm{H}$ for a single loop. Assuming the mutual inductances between the coil segments to be negligible, the total inductance of the coil is determined by adding up the inductances for each of the coil segments, calculated by multiplying the single loop inductance by the square of the number of turns in the segment. Having two single loops and one double loop segment gives $(1^2 + 2^2 + 1^2 = 6)$, such that the total inductance of the coil becomes $L_g = 1.78\,\mu\mathrm{H}$.

The field-current ratio of the sensing loop of the coil is found by rearranging the Biot-Savart law, see Equation 7.2, to obtain

$$\frac{B_z}{I} = \frac{\mu_0}{2} \frac{a^2}{(a^2 + z^2)^{3/2}}$$

This gives $B/I = 1.93 \times 10^{-5}\,\mathrm{T/A}$ at the centre of the coil, *i.e.* at $z = 0$. At $z = 30\,\mathrm{mm}$, which roughly corresponds to the distance between the sensing coil and the centre of the sample, $B/I = 7.67 \times 10^{-6}\,\mathrm{T/A} \equiv B_1$.

7.3.3 Expected Signal-to-Noise Ratio

The flux coupled to the sensing loop is given by

$$\phi_p = B_1 M_0 V_s \tag{7.11}$$

where M_0 is the initial magnetization of the sample and V_s is the sample volume. The sample volume to be used with the polarizing coil described earlier is $V_s = 2\,\mathrm{cm}^3 = 8 \times 10^{-6}\,\mathrm{m}^3$. The initial magnetization M_0 is given by

$$M_0 = \frac{\chi_0}{\mu_0} B_p \tag{7.12}$$

where the initial susceptibility χ_0 is equal to

$$\chi_0 = \frac{\mu_0 n \hbar^2 \gamma^2}{4kT} \tag{7.13}$$

Water at $T = 300\,\mathrm{K}$ has a number density of $n = 6.69 \times 10^{28}\,\mathrm{m}^{-3}$, such that $\chi_0 = 4.05 \times 10^{-9}$ and $M_0 = 3.22 \times 10^{-3} B_p$. Using $B_p = 10\,\mathrm{mT}$, Equation 7.11 gives the flux in the sensing loop generated by the protons in the water sample as $\phi_p = 1.976 \times 10^{-15}\,\mathrm{Wb} = 0.956\ \phi_0$ ($\phi_0 = 2.067 \times 10^{-15}\,\mathrm{Wb}$).

The flux coupled to the SQUID is given by

$$\phi_{SQ} = \frac{-\phi_p M_i}{(L_g + L_i)} \tag{7.14}$$

where L_i is the inductance of the input coil and M_i is the mutual inductance between the input coil and the SQUID. For SQUID C519-B22, $L_i = 1.8\,\mu\mathrm{H}$ and $M_i = 9.0\,\mathrm{nH}$. Using $\phi_p = 1.976 \times 10^{-15}\,\mathrm{Wb}$ and $L_g = 1.78\,\mu\mathrm{H}$ thus gives the corresponding flux coupled to the SQUID as $\phi_{SQ} = 4.96 \times 10^{-18}\,\mathrm{Wb} = 0.0024\ \phi_0$.

Signal-to-Noise Ratio if Limited by SQUID Noise

The time domain signal-to-noise ratio based on the intrinsic noise of the SQUID, can be determined by combining Equations 2.26 and 7.14 to get

$$\frac{\phi_{SQ}}{\langle \phi_N^2 \rangle^{1/2}} = \frac{\phi_p}{(L_g + L_i)} \left(\frac{L_i}{2\epsilon_c} \right)^{1/2} \tag{7.15}$$

which, when taking the coupled energy sensitivity of the SQUID to be $\epsilon_c \sim 50h$, results in

$$\frac{\phi_{SQ}}{\langle \phi_N^2 \rangle^{1/2}} = 2876$$

The corresponding frequency domain SNR is then given by

$$\frac{S}{N} = \frac{\phi_{SQ}}{\langle \phi_N^2 \rangle^{1/2}} \left(\frac{1}{K_f} \sqrt{\frac{T_2^*}{2K_t}} \right) \tag{7.16}$$

where K_f is the ratio of peak noise to rms noise in the frequency domain and K_t is the ratio of the capture time to T_2^*, which we take to be 2.5 and 1 respectively [118]. Setting $K_t = 1$ will give a distorted line, but a good signal-to-noise ratio.

T_2^* needs to be determined from the magnet inhomogeneity using the expression

$$\frac{1}{T_2^*} = \frac{1}{T_2} + \pi \Delta f \tag{7.17}$$

where $T_2^{-1} = \pi(0.16\,\mathrm{Hz}) = 0.5\,\mathrm{Hz}$ and $\Delta f = \alpha f_0$ since

$$\frac{\Delta f}{f_0} = \alpha = \frac{\Delta B}{B}$$

From the simulation done for the chosen magnet design, α was determined to be $\sim 50\,\mathrm{ppm}$ at a distance of 1 cm from the centre. Assuming this to be a factor of ten worse to get a conservative estimate, such that $\alpha = 500\,\mathrm{ppm}$ and taking the measurement frequency to be $f_0 = 1\,\mathrm{kHz}$, gives

$$T_2^* = [(0.5\,\mathrm{Hz}) + \pi(500\,\mathrm{ppm})(1000\,\mathrm{Hz})]^{-1} = 0.5\,\mathrm{s}$$

Substituting this value for T_2^* into Equation 7.16 gives a single-shot SNR in the frequency domain of 575.

Signal-to-Noise Ratio if Limited by Environmental Noise

The time domain SNR for this setup if environmental noise is the dominating factor, depends on the flux noise coupled to the sensing loop, given by

$$\left\langle \phi_N^2 \right\rangle^{1/2} = A_p \left\langle B_N^2 \right\rangle^{1/2} \tag{7.18}$$

where A_p is the area of the pick-up loop and $\langle B_N^2 \rangle^{1/2}$ is the magnetic field noise, which was measured to be $\sim 2 \times 10^{-13}\,\mathrm{THz}^{-1/2}$ at 1 kHz inside the MSR.

Assuming initially that the gradiometer is completely ineffective at reducing the noise, the total flux noise coupled to the gradiometer can be calculated by adding up the squares of the flux noise for all the coil segments, such that

$$\left\langle \phi_N^2 \right\rangle^{1/2} = \sqrt{6} A_p \left\langle B_N^2 \right\rangle^{1/2} \tag{7.19}$$

Dividing the signal flux coupled to the sensing loop ϕ_p by the total flux noise coupled to the coil, gives a SNR in the time domain of 1.2, corresponding to a SNR in the frequency domain of 0.17. This is a worst case scenario and improves by almost a factor of 2 if the magnet inhomogeneity is as simulated. Furthermore if the gradiometer has a 1 in 10 balance, resulting in a lowering of the noise background by a factor of 10, the SNR in the frequency domain increases from 0.17 to 1.7. With a 1 in 100 balance, which has been achieved previously with similar gradiometers elsewhere [17], the SNR can go up to 17.

7.4 Holdtime Testing

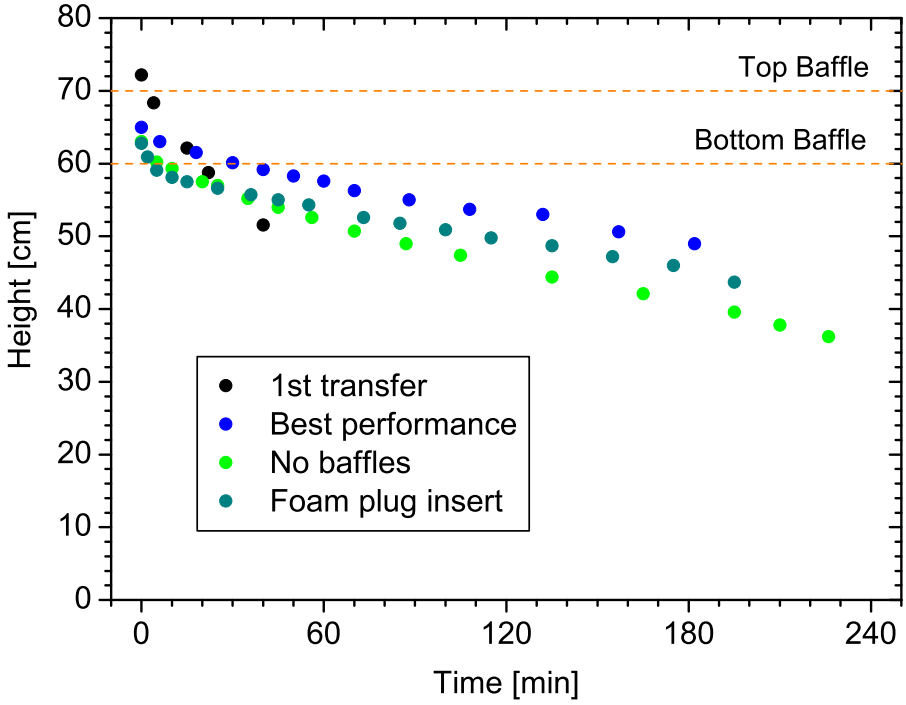

Figure 7.21: Plot showing the liquid helium level inside the home-built fibreglass Dewar as a function of time following a transfer.

Once the Dewar was fully assembled, a first and crucial test was to measure its holdtime. After pumping out the vacuum space for half a day, the Dewar was filled with liquid nitrogen and left to precool over night. Before preparing to transfer liquid helium into the Dewar, the liquid nitrogen was poured out and the top of the insert holding the two copper baffles was put in place. The boil-off following the very first transfer was very high and was assumed to be due to the helium being used up to cool the inner vessel and the still warm insert.

Subsequent consecutive transfers did result in improved boil-off rates, but the corresponding holdtimes were much lower than expected. The best achievable boil-off rate was about 36 mm/hr, giving a holdtime of approximately 16 hours and an operation time of about 5 hours, if the SQUID is positioned around 400 mm from the bottom of the insert. The minimum expected holdtime and operation times

were about twice that. Different types of foam plug inserts and baffle combinations were experimented with. Figure 7.21 shows some of the results from the initial test transfers. The boil-off rates became worse later on, at some point giving holdtimes of just over an hour.

One issue that was identified was the aluminium pump-port. During prolonged times of heavy boil-off, the top aluminium plate can become frozen to the extent that the contracting pump-port with its frozen O-rings begins to leak. When the charcoal inside the vacuum space becomes saturated, exchange gas starts to appear and the Dewar jacket goes soft. This can be prevented by heating the port if necessary and only caused a real problem once so far.

The main reason behind the poor performance of the Dewar appears to be the vapour shield. As a diagnostic measure, three Si diode thermometers were stuck to the vapour shield, one onto the aluminium wires attached to the heat exchanger at the top, a second one on the alumina rods just below the aluminium-alumina link and a final one on the bottom alumina plate. They showed that the vapour shield seemed to decouple from the inner vessel as both cool down, due to the difference in thermal contraction between the fibreglass cylinder and the surrounding aluminium ring. As a very rough guide, the differential contraction (using $\Delta l/l \sim 0.6\,\%$ for G-10 and $0.38\,\%$ for aluminium at 100 K [52]) for 106 mm of both materials would result in an additional gap between the ring and the cylinder of $\frac{1}{2}(0.12\,\mathrm{mm})$.

With the vapour shield not thermally linked to the helium vapour, the temperature environment that the inner vessel is exposed to is therefore substantially higher than it ideally should be, resulting in an increased boil-off rate. A plan to improve the holdtime of the Dewar is to unglue the aluminium wires, move the aluminium ring and then reattach the aluminium wires directly to the neck of the Dewar for a more reliable and flexible thermal contact.

7.5 Summary

Work on the design and construction of a new low-field NMR set-up with a directly accessible room temperature sample area is presented. The magnetic background environment provided by a magnetically screened enclosure has been characterized. A prototype low-noise fibreglass Dewar and a made-to-fit fibreglass SQUID insert holding a gradiometric receiver coil have been designed and constructed. Room temperature NMR coil designs have been studied from which the coil dimensions to be used here have been determined. The expected signal-to-noise ratios have been calculated for this set-up and obtaining a signal should be relatively straightforward. The holdtime of the finished fibreglass Dewar was measured to be almost 16 hours at best and has been identified as an area needing improvement.

Chapter 8

Conclusions and Future Work

The work described in this thesis falls largely into two main categories; one part was focused on the improvement of existing and the development of new low-field NMR instrumentation, the other part consisted of investigating aqueous magnetic nanoparticle solutions for their suitability as contrast agents for low-field MRI. In this chapter, the results and work presented in the preceeding chapters are discussed and conclusions are drawn. Finally, the next steps and some potential future work are outlined.

8.1 Discussion

8.1.1 Low-Field NMR Spectrometer Dipper Probe

A sensitive low-field NMR spectrometer with DC SQUID detection has been developed which is capable of maintaining a stable room temperature sample region within a cryogenic environment, with a warm to cold distance of only $\sim 1\,\mathrm{mm}$. The sensitivity of the spectrometer has been improved throughout this work, as described in Chapter 3. This improvement was a result of replacing the original SQUID array with a Two-Stage SQUID amplifier, that delivered a higher sensitivity of 30–50 h. It was also due to the incorporation of a power amplifier to increase the strength of the prepolarizing pulses, as well as the great care taken in avoiding any magnetic materials in the sample region. All this ultimately resulted in a decrease in averaging time of more than an order of magnitude for a given signal-to-noise ratio.

Using this set-up, NMR signals have been observed in the frequency range of 4 Hz to 600 kHz. All the data presented in this work was obtained from very small liquid samples between 100 and 150 µl, underlining the sensitivity of the dipper probe spectrometer. The improvements in the signal-to-noise ratio we achieved, enabled us to observe proton NMR signals from water down to 4 Hz. Furthermore, we were able to measure the intrinsic linewidth of water at finite fields with a compact shielding arrangement. We could use a prepolarizing pulse of up to 4 mT without significant broadening of the signal linewidth due to flux trapping in the inner superconducting shield. We were also able to use a prepolarizing pulse of up to 15 mT to measure T_1 in the prepolarizing field, assuming the resulting line broadening to be constant.

As described in Chapter 4, it was necessary to develop new pulse sequences in order to measure T_1 in the lowest fields, where the sample magnetization is too small for an RF or B_p measurement. For this purpose, we successfully adopted techniques used by Melton *et al.* [59] and Friedman *et al.* [3].

The performance of the dipper probe spectrometer was characterized and tested with a range of samples. We measured water, because it has a high spin density and long T_1 and T_2 relaxation times, therefore providing a good test for looking at the residual field gradients in the system. In addition, we measured oil-water mixtures to demonstrate the ability of the spectrometer to record two-component signals, which can have potential applications in measuring water contamination in oil samples, see [58]. We also looked at oil samples, which have much shorter relaxation times than water, to show the capability of the spectrometer to accurately measure samples with short T_2s, which paved the way for the magnetic nanoparticle work.

8.1.2 NMR on Aqueous Magnetic Nanoparticle Solutions

The dipper probe spectrometer has been used in conjunction with two conventional benchtop NMR spectrometers to assess the suitability of superparamagnetic nanoparticles for use as contrast agents in low-field MRI. The latter study was undertaken as part of the European Framework 6 Biodiagnostics project.

As part of the Biodiagnostics project, we measured the T_1 and T_2 frequency dependence of aqueous solutions of magnetic nanoparticles. Direct measurements of these were at much lower fields than those of other groups. In Chapter 5 we presented a theoretical model based on the random diffusion of protons in the local magnetic fields arising from the nanoparticles. This theoretical model was used to analyze our measurements of the frequency dependence of the proton relaxation rates of two different samples of superparamagnetic iron oxide nanoparticles in solution, namely fluidMAG-HEAS and POA@SPION. We found that for both nanoparticle systems, in order to describe the data, we had to use an average magnetic core diameter that was larger than that specified by the manufacturers and a hydrodynamic diameter which was smaller than that determined by photon correlation spectroscopy. These results are consistent with a spread of particle sizes, since those nanoparticles that

have the largest magnetic core size and the smallest hydrodynamic diameter are the ones that are most efficient in causing spin relaxation.

In addition, the theoretical calculations suggest that $T_1 = T_2$ at low frequencies. This was confirmed for the fluidMAG-HEAS sample, but not for the POA@SPION sample. A possible reason that $T_1 > T_2$ for POA@SPION, even at the lowest frequencies, could be the composite coating of the particles [107], which delivers an increased R_2/R_1 ratio even at low fields, thus suggesting that these nanoparticles could be particularly useful as contrast agents in low-field MRI.

In a separate experiment we investigated the relaxation properties of fluidMAG-HS/CF, a solution of $CoFe_2O_4$ nanoparticles. These samples contained a significant fraction of Brownian particles. We were looking for a correlation between the imaginary susceptibility peak of the cobalt-ferrite nanoparticles in solution and the proton relaxation times measured at the frequency of this peak, which was exactly in the frequency region that can be probed by low-field SQUID NMR. We did not observe any such correlation.

8.1.3 Development of Low-Field MRI system

The current stage in the development of our room temperature SQUID NMR capability is to build a system to perform SQUID NMR experiments where the sample is located outside of the cryogenic environment. The simplest way of achieving this is to place the Dewar inside a magnetically shielded room, since such a set-up can no longer benefit from the use of superconducting shields, as in our previous system. An alternative to using a magnetically shielded room is to build a system of three compensation coils, one for each axis, to cancel out any extraneous magnetic fields, including the Earth's magnetic field, as used in [17]. This route was not pursued in our case, since the background noise in our Biodiagnostics laboratory is quite elevated. The magnetically screened room was delivered, installed, tested, reinstalled

and finally retested. Much time and effort was spent on attempting to optimize the below-spec performance of the screened room.

As detailed in Chapter 7, much progress has already been made in the development of the new set-up. The entire system has been designed and the estimated signal-to-noise ratio looks promising. The prototype low-noise liquid helium Dewar has been built and at present has a hold time of just under a day. While this is sufficient for initial tests, further development is required to improve this. Final construction of the experimental insert and the room temperature coil assembly and support structure are currently underway.

8.2 Conclusions

The main aim of this project was to apply improvements in SQUID NMR technology to benefit measurements on room temperature samples, to lead us into the fields of low-field NMR spectroscopy and MRI. A secondary aim was to evaluate aqueous solutions of magnetic nanoparticles for use as contrast agents in low-field MRI, in conjunction with a comparison to current theoretical models of proton relaxation in their presence. We measured different types of magnetic nanoparticle dispersions, but encountered problems with the temporal stability of these suspensions under experimental conditions, which combined with a large spread in sizes of the available particles as well as insufficient characterization information, makes it difficult in some instances to obtain firm conclusions from the analysis of the data. Nevertheless, our measurements being the only ones of this kind performed on any nanoparticle solutions, give new information about the behaviour and contrast effect in low magnetic fields for each of the samples measured.

In relation to the main objective of this work, we obtained the first ever NMR signals of a room temperature sample using SQUIDs in the Low Temperature group at Royal Holloway and achieved some improvements over previous work done by other groups, such as short measurements deadtimes, small sample sizes and techniques for measuring T_1 in low fields. Our proof-of-principle dipper probe spectrometer cannot provide sufficiently high prepolarizing fields to allow us to explore its NMR spectroscopy capabilities, due to the consequent inadequate signal-to-noise ratio. This is to be addressed eventually in the home-built low-noise Dewar system, which will also form the basis of a planned NMR imaging experiment. Despite some setbacks with the performance of the magnetically shielded enclosure, the main part of this system, the Dewar, has already been built and most of the remaining components have been designed and in some cases constructed. Much progress has therefore been made towards reaching the ultimate aims of this project.

8.3 Future Work

Before moving on to future work relating to the new SQUID NMR system being developed, it is worth noting that the dipper probe spectrometer could still provide us with some interesting results. Even though using it involves relatively long sample turn-around times, it has proven to produce good and consistent data, especially with aqueous samples. With the procedures involved now well established, one possibility would be to perform measurements on well characterized magnetic nanoparticle solutions with better physical characteristics, to allow us to draw more firm conclusions as to the validity of the proton relaxation theories presented in Chapter 5. Furthermore, measurements of more widely used commercial nanoparticle contrast agents could be carried out in order to evaluate their performance as MRI contrast agents in low magnetic fields. In the future these same measurements can of course be made using the new system, which will not only offer much shorter sample turn-around times, but will also avoid any potential sample stability issues.

One measurement that was not achievable with the dipper probe spectrometer, but which is still of interest, especially using the new system, would be a demonstration of the broadband capabilities of our SQUID NMR setup by performing a spectroscopy experiment. For this purpose, initial tests could be on biological samples such as suspensions of an amino acid like glycine. Work on low-field NMR spectroscopy has already been carried out by some groups [14, 22, 119] and is of interest because the spectral resolution at low fields is essentially limited by the natural linewidth of the spectral lines, since the inhomogeneous broadening of the signals is very small. Furthermore, chemical shifts are negligible at low fields, which therefore enables pure J-spectroscopy measurements.

But ultimately, the new system is being developed to be used for low-field MRI. Once we have attained imaging capability, an interesting future research application could be neuronal current imaging. The group at Los Alamos has recently performed

simultaneous SQUID MRI and magnetoencephalography (MEG) experiments [20]. MEG uses an array of SQUIDs to measure the magnetic fields due to neuronal currents in the brain [120]. Applications include the location of epileptic foci. One difficulty with MEG is what is know as the inverse problem. The same measured magnetic fields could be a result of different sources, which often limits the spatial resolution of MEG to the cm range. In practice, MEG data need to be combined with functional MRI (fMRI) data on the same patient in order to locate the sources of the measured neuronal currents, but the temporal resolution of fMRI is only on the order of seconds, since it involves changes in blood flow to regions of neuronal activity. The Los Alamos group suggested that low-field SQUID NMR/MRI could give rise to a new method of neuronal current imaging [121], due to the fact that the frequencies of neuronal activity lie in the range accessible to low-field SQUID NMR. This idea is based on the expectation that a resonant mechanism might allow the neuronal activity to alter the relaxation properties of nearby protons in the brain at these frequencies. This has been evaluated theoretically by Cassara and Maraviglia [122] and possible approaches are suggested in [123], which promise to offer mapping of brain activity with high spatial and temporal resolution and are only possible given the sensitivity of low-field SQUID NMR. Our new set-up could be used for experiments with neuronal current phantoms designed to determine the detection limit of neuronal activity.

Magnetic nanoparticles could provide another future area of research for our planned MRI system. A major problem in magnetic drug targeting using magnetic nanoparticles is the absence of a good method for measuring the distribution of magnetic nanoparticles in the body [124]. MRI shows promise as a possible means of achieving this [125] and the potential for low-field MRI for imaging nanoparticle distributions could be investigated.

Before we can undertake any of the work described above with the new NMR system, a substantial amount of work still needs to be completed to get the system up and running. First of all, the holdtime of the Dewar needs to be optimized, since it has the potential to perform much better [13, 113], although its present holdtime is sufficient to progress with initial testing, provided that it does not get too much worse with the completed experimental insert in place. The next step is to measure the noise performance of the Dewar, with and without having the SQUID sensor attached to the gradiometer. Following that, we should try to obtain signals from water as a function of frequency and compare the results to those obtained using the dipper probe. If the overall performance is good enough, we could attempt NMR spectroscopy measurements or further work with magnetic nanoparticle solutions. Once these basic experiments have been completed satisfactorily, work can then start on optimizing the system for a given application. Depending on requirements, this could involve a redesigning of the room temperature coils, as well as the addition of a z-gradient coil to allow for 1D imaging, or even a further two sets of gradient coils for 3D imaging. At this stage the possibilities will be endless.

Bibliography

[1] R. A. Webb, "New technique for improved low temperature SQUID NMR measurements," *Rev. Sci. Instrum.*, vol. 48, pp. 1585–1594, 1977.

[2] M. B. Ketchen and J. M. Jaycox, "Ultra-low noise tunnel junction DC SQUID with a tightly coupled planar input coil," *Appl. Phys. Lett.*, vol. 40, pp. 736–738, 1982.

[3] L. J. Friedman, A. K. Wennberg, S. N. Ytterboe, and H. M. Bozler, "Direct detection of low-frequency NMR using a DC SQUID," *Rev. Sci. Instrum.*, vol. 57, pp. 410–413, 1986.

[4] M. R. Freeman, R. S. Germain, R. C. Richardson, M. L. Roukes, W. L. Gallagher, and M. B. Ketchen, "Low temperature nuclear magnetic resonance with a DC SQUID amplifier," *Appl. Phys. Lett.*, vol. 48, pp. 300–302, 1986.

[5] C. Hilbert, J. Clarke, T. Sleator, and E. L. Hahn, "Nuclear quadrupole resonance detected at 30 MHz with a DC superconducting quantum interference device," *Appl. Phys. Lett.*, vol. 47, pp. 637–639, 1985.

[6] N. Q. Fan and J. Clarke, "Low frequency nuclear magnetic resonance and nuclear quadrupole resonance spectrometer based on a DC superconducting quantum interference device," *Rev. Sci. Instr.*, vol. 62, pp. 1453–1459, 1991.

[7] D. M. TonThat and J. Clarke, "Direct current superconducting quantum interference device spectrometer for pulsed nuclear magnetic resonance and nuclear

quadrupole resonance at frequencies up to 5 MHz," *Rev. Sci. Instr.*, vol. 67, pp. 2890–2893, 1996.

[8] Y. S. Greenberg, "Application of superconducting quantum interference devices to nuclear magnetic resonance," *Rev. Mod. Phys.*, vol. 70, pp. 175–222, 1998.

[9] S. Kumar, B. D. Thorson, and W. F. Avrin, "Broadband SQUID NMR with room temperature samples," *J. Magn. Reson. B*, vol. 107, pp. 252–259, 1995.

[10] S. Kumar, W. F. Avrin, and B. R. Whitecotton, "NMR of room temperature samples with a flux-locked DC SQUID," *IEEE Trans. Magnetics*, vol. 32, pp. 5261–5264, 1996.

[11] H. C. Seton, J. M. S. Hutchinson, and D. M. Bussell, "A tuned SQUID amplifier for MRI based on a DOIT flux locked loop," *IEEE Trans. Appl. Supercond.*, vol. 7, pp. 3213–3216, 1997.

[12] H. C. Seton, J. M. S. Hutchinson, and D. M. Bussell, "A 4.2 K receiver coil and SQUID amplifier used to improve the SNR of low-field magnetic resonance images of the human arm," *Meas. Sci. Technol.*, vol. 8, pp. 198–207, 1997.

[13] H. C. Seton, J. M. S. Hutchinson, and D. M. Bussell, "Liquified gas cryostat." UK Patent GB2331798.

[14] R. McDermott, A. H. Trabesinger, M. Mück, E. L. Hahn, A. Pines, and J. Clark, "Liquid-state NMR and scalar couplings in microtesla magnetic fields," *Science*, vol. 295, pp. 2247–2249, 2002.

[15] M. Packard and R. Varian, "Free nuclear induction in the Earth's magnetic field," *Phys. Rev.*, vol. 93, p. 941, 1954.

[16] M. Burghoff, S. Hartwig, L. Trahms, and J. Bernarding, "Nuclear magnetic resonance in the nanotesla range," *Appl. Phys. Lett.*, vol. 87, p. 054103, 2005.

[17] R. F. McDermott, "SQUID-detected NMR and MRI in microtesla magnetic fields," PhD thesis, University of California, Berkeley, US, 2002.

[18] R. McDermott, N. Kelso, S.-K. Lee, M. Mössle, M. Mück, W. Myers, B. ten Haken, H. C. Seton, A. H. Trabesinger, A. Pines, and J. Clark, "SQUID-detected magnetic resonance imaging in microtesla magnetic fields," *J. Low Temp. Phys.*, vol. 135, pp. 793–821, 2004.

[19] V. S. Zotev, A. N. Matlashov, P. L. Volegov, A. V. Urbaitis, M. A. Espy, and R. H. K. Jr., "SQUID-based instrumentation for ultra-low-field MRI," *Supercond. Sci. Technol.*, vol. 20, pp. S367–S373, 2007.

[20] V. S. Zotev, A. N. Matlashov, P. L. Volegov, I. M. Savukov, M. A. Espy, J. C. Mosher, J. J. Gomez, and R. H. K. Jr., "Microtesla MRI of the human brain combined with MEG," *J. Magn. Reson.*, vol. 194, pp. 115–120, 2008.

[21] M. Espy, M. Flynn, J. Gomez, C. Hanson, R. Kraus, P. Magnelind, K. Maskaly, A. Matlashov, S. Newman, T. Owens, M. Peters, H. Sandin, I. Savukov, L. Schultz, A. Urbaitis, P. Volegov, and V. Zotev, "Ultra-low-field MRI for the detection of liquid explosives," *Supercond. Sci. Technol.*, vol. 23, p. 034023, 2010.

[22] L. Qiu, Y. Zhang, H. J. Krause, A. I. Braginski, M. Burghoff, and L. Trahms, "Nuclear magnetic resonance in the Earth's magnetic field using a nitrogen-cooled superconducting quantum interference device," *Appl. Phys. Lett.*, p. 072505, 2007.

[23] C. P. Lusher, M. R. Dann, R. P. Reed, M. E. Digby, B. P. Cowan, and J. Saunders, "Direct detection of NMR at low frequencies using a DC SQUID amplifier," *Czech. J. Phys.*, vol. 46, pp. 2831–2832, 1996.

[24] Quantum Design Inc., 6325 Lusk Boulevard, San Diego, CA 92121, USA; `http://www.qdusa.com`.

[25] Physikalisch-Technische Bundesanstalt, Division Berlin, 2-12 Abbestrasse, 10587 Berlin, Germany; `http://www.ptb.de`.

[26] D. Drung, H. Matz, and H. Koch, "A 5 MHz bandwidth SQUID magnetometer with additional positive feedback," *Rev. Sci. Instrum.*, vol. 66, pp. 3008–3015, 1995.

[27] D. Drung, C. Assmann, J. Beyer, A. Kirste, M. Peters, F. Ruede, and T. Schurig, "DC SQUID readout electronics with up to 100 MHz closed-loop bandwidth," *IEEE Trans. Appl. Supercond.*, vol. 15, pp. 777–780, 2005.

[28] D. Drung, C. Assmann, J. Beyer, A. Kirste, M. Peters, F. Ruede, and T. Schurig, "Highly sensitive and easy-to-use SQUID sensors," *IEEE Trans. Appl. Supercond.*, vol. 17, pp. 699–704, 2007.

[29] A. Casey, B. P. Cowan, M. E. Digby, H. Dyball, R. Körber, J. Li, C. P. Lusher, V. Maidanov, J. Nyeki, J. Saunders, D. Drung, and T. Schurig, "Nuclear magnetic resonance using DC SQUIDs with APF," *Physica C*, vol. 399, pp. 93–97, 2003.

[30] C. P. Lusher, J. Li, M. E. Digby, R. P. Reed, B. P. Cowan, J. Saunders, D. Drung, and T. Schurig, "Broadband nuclear magnetic resonance using DC SQUID amplifiers," *Appl. Supercond.*, vol. 6, pp. 591–601, 1998.

[31] A. Casey, A. Corcoles, C. P. Lusher, B. P. Cowan, and J. Saunders, "Studies of superfluid He-3 confined to a regular submicron slab geometry, using SQUID NMR," *Low Temp. Phys. A and B, A.I.P. Conference Proceedings*, vol. 850, pp. 97–98, 2006.

[32] A. Casey, R. Schanen, C. P. Lusher, B. P. Cowan, and J. Saunders, "Ferromagnetism of 2D solid He-3 investigated by SQUID NMR," *J. Low Temp. Phys.*, vol. 134, pp. 649–654, 2004.

[33] R. Körber, A. Casey, B. P. Cowan, M. E. Digby, J. Li, J. Luo, C. P. Lusher, J. Saunders, D. Drung, T. Schurig, J. B. Kycia, J. I. Hong, D. N. Seidman, and W. P. Halperin, "Low field DC SQUID nuclear magnetic resonance on single crystal UPt_3," *Physica C*, vol. 338, pp. 523–524, 2003.

[34] B. Yager, J. Nyéki, A. Casey, B. P. Cowan, C. P. Lusher, J. Saunders, D. Drung, and T. Schurig, "Pulsed nuclear magnetic resonance on He-3 adsorbed on bare and He-4 preplated MCM-41 using DC SQUID detection," *J. Low Temp. Phys.*, vol. 158, pp. 213–219, 2010.

[35] E. M. Purcell, H. C. Torrey, and R. V. Pound, "Resonance absorption by nuclear magnetic moments in a solid," *Phys. Rev.*, vol. 69, pp. 37–38, 1946.

[36] F. Bloch, W. W. Hansen, and M. Packard, "Nuclear induction," *Phys. Rev.*, vol. 69, p. 127, 1946.

[37] B. P. Cowan, *Nuclear Magnetic Resonance and Relaxation*. Cambridge: CUP, 1997.

[38] C. P. Slichter, *The Principles of Magnetic Resonance*. Berlin: Springer Verlag, 3rd enl. and updated ed. ed., 1990.

[39] A. Abragam, *The Principles of Nuclear Magnetism*. Oxford: Clarendon Press, 1961.

[40] J. Clarke and A. I. Braginski, eds., *The SQUID Handbook, Vol. 1 Fundamentals and Technology of SQUIDs and SQUID Systems*. Weinheim: Wiley-VCH Verlag, 2004.

[41] F. Bloch, "Nuclear induction," *Phys. Rev.*, vol. 70, pp. 460–474, 1946.

[42] D. Drung, "Advanced SQUID read-out electronics," in *SQUID Sensors: Fundamentals, Fabrication and Applications* (H. Weinstock, ed.), pp. 63–116, Dordrecht: Kluwer Academic Publishers, 1996.

[43] Bartington Instruments Ltd., 10 Thorney Leys Business Park, Witney, Oxfordshire, OX28 4GG, UK; `http://www.bartington.com`.

[44] Pickering Interfaces Ltd., Stephenson Road, Clacton-on-Sea, CO15 4NL, U.K; `http://www.pickeringtest.com`.

[45] Tektronix Inc., 14150 SW Karl Braun Drive, P.O. Box 500, Beaverton, OR 97077, USA; `http://www.tek.com`.

[46] Magnicon GmbH, Division Berlin, 2-12 Abbestrasse, 10587 Berlin, Germany; `http://www.magnicon.com`.

[47] D. Hechtfischer, "Generation of homogeneous magnetic fields within closed superconductive shields," *Cryogenics*, vol. 27, pp. 503–504, 1987.

[48] T. Uchiyama and T. Mamiya, "Low-power persistent switch for superconducting magnet," *Rev. Sci. Instrum.*, vol. 58, pp. 2192–2193, 1987.

[49] Computer program: modified by Michael Boegl, Experimental Physics 5, University of Bayreuth, Germany, based on original program from Helsinki University, Finland.

[50] D. I. Hoult and R. E. Richards, "The signal-to-noise ratio of the nuclear magnetic resonance experiment," *J. Magn. Reson.*, vol. 24, pp. 71–85, 1976.

[51] Lake Shore Cryotronics Inc., 575 McCorkle Blvd, Westerville, OH 43082-8699, USA; `http://www.lakeshore.com`.

[52] J. W. Ekin, *Experimental Techniques for Low-Temperature Measurements*. Oxford: Oxford University Press, 2006.

[53] National Instruments Corp., 11500 N Mopac Expwy, Austin, TX 78759-3504, USA; `http://www.ni.com`.

[54] A. E. Techron Inc., 2507 Warren Street, Elkhart, IN 46516, USA; `http://www.aetechron.com`.

[55] R. Körber, A. Casey, A. Shibahara, M. Piscitelli, B. P. Cowan, C. P. Lusher, J. Saunders, D. Drung, and T. Schurig, "Nuclear magnetic resonance on room temperature samples in nanotesla fields using a two-stage DC superconducting quantum interference device sensor," *Appl. Phys. Lett.*, vol. 91, p. 142501, 2007.

[56] V. Graf, F. Noack, and G. J. Béné, "Proton spin T_1 relaxation dispersion in liquid H_2O by slow proton-exchange," *J. Chem. Phys.*, vol. 72, pp. 861–863, 1980.

[57] Shell plc, Carel van Bylandtlaan 16, 2596 HR The Hague, The Netherlands; `http://www.shell.com`.

[58] G. R. Coates, L. Xiao, and M. G. Prammer, *NMR Logging Principles and Applications*. Houston: Halliburton Energy Services, 1999.

[59] B. F. Melton, V. L. Pollack, T. W. Mayes, and B. L. Willis, "Condition for sudden passage in the earth's field NMR technique," *J. Magn. Reson. A*, vol. 117, pp. 164–170, 1995.

[60] Q. A. Pankhurst, J. Connolly, S. K. Jones, and J. Dobson, "Applications of magnetic nanoparticles in biomedicine," *J. Phys. D: Appl. Phys.*, vol. 36, pp. R167–R181, 2003.

[61] Y. X. J. Wang, S. M. Hussain, and G. P. Krestin, "Superparamagnetic iron oxide contrast agents: physiochemical characteristics and applications in MR imaging," *Europ. Radiol.*, vol. 11, pp. 2319–2331, 2001.

[62] C. Sun, J. S. H. Lee, and M. Zhang, "Magnetic nanoparticles in MR imaging and drug delivery," *Adv. Drug Deliv. Rev.*, vol. 60, pp. 1252–1265, 2008.

[63] A. K. Gupta and M. Gupta, "Synthesis and surface engineering of iron oxide nanoparticles for biomedical applications," *Biomaterials*, vol. 26, pp. 3995–4021, 2004.

[64] P. Tartaj, M. P. Morales, S. Veintemillas-Verdaguer, T. González-Carreño, and C. J. Serna, "The preparation of magnetic nanoparticles for applications in biomedicine," *J. Phys. D: Appl. Phys.*, vol. 36, pp. R182–R197, 2003.

[65] C. E. Sjögren, C. Johansson, A. Naevestad, P. C. Sontum, K. Briley-Saebø, and A. K. Fahlvik, "Crystal size and properties of superparamagnetic iron oxide (SPIO) particles," *Magn. Reson. Imag.*, vol. 15, pp. 55–67, 1997.

[66] S. Foner, "Versatile and sensitive vibrating-sample magnetometer," *Rev. Sci. Instr.*, vol. 30, pp. 548–557, 1959.

[67] W. Tscharnuter, "Photon correlation spectroscopy in particle sizing," in *Encyclopedia of Analytical Chemistry* (R. A. Meyers, ed.), John Wiley & Sons Ltd., 2006.

[68] C. Johansson, M. Hanson, M. S. Pedersen, and S. Mørup, "Magnetic properties of magnetic liquids with iron-oxide particles – the influence of anisotropy and interactions," *J. Magn. Magn. Mater.*, vol. 173, pp. 5–14, 1997.

[69] B. H. Erné, M. Claesson, S. Sacanna, M. Klokkenburg, E. Bakelaar, and B. W. M. Kuipers, "Low-frequency complex magnetic susceptibility of mag-

netic composite microspheres in colloidal dispersion," *J. Magn. Magn. Mater.*, vol. 311, pp. 145–149, 2007.

[70] A. P. Astalan, C. Jonasson, K. Petersson, J. Blomgren, D. Ilver, A. Krozer, and C. Johansson, "Magnetic response of thermally blocked magnetic nanoparticles in a pulsed magnetic field," *J. Magn. Magn. Mater.*, vol. 311, pp. 166–170, 2007.

[71] F. Ludwig, E. Heim, and M. Schilling, "Characterization of magnetic core-shell nanoparticles by fluxgate magnetorelaxometry, ac susceptibility, transmission electron microscopy and photon correlation spectroscopy - a comparative study," *J. Magn. Magn. Mater.*, vol. 321, pp. 1644–1647, 2009.

[72] Imego AB, Arvid Hedvalls Backe 4, 41133 Göteborg, Sweden; `http://www.imego.com`.

[73] C. P. Bean and J. D. Livingston, "Superparamagnetism," *J. Appl. Phys.*, vol. 30, pp. S120–S129, 1959.

[74] J. L. Dormann, "Le phénomène de superparamagnétisme," *Revue Phys. Appl.*, vol. 16, pp. 275–301, 1981.

[75] E. H. Frei, S. Shtrikman, and D. Treves, "Critical size and nucleation field of ideal ferromagnetic particles," *Phys. Rev.*, vol. 106, pp. 446–455, 1957.

[76] B. Huke and M. Lücke, "Magnetic properties of colloidal suspensions of interacting magnetic particles," *Rep. Prog. Phys.*, vol. 67, pp. 1731–1768, 2004.

[77] R. Kötitz, W. Weitschies, L. Trahms, W. Brewer, and W. Semmler, "Determination of the binding reaction between avidin and biotin by relaxation measurements of magnetic nanoparticles," *J. Magn. Magn. Reson.*, vol. 194, pp. 62–68, 1999.

[78] L. Néel, "Théorie du trainage magnétique des ferromagnétiques en grains fins avec applications aux terres cuites," *Ann. Géophys.*, vol. 5, pp. 99–136, 1949.

[79] S. Bedanta and W. Kleemann, "Supermagnetism," *J. Phys. D: Appl. Phys.*, vol. 42, p. 013001, 2009.

[80] V. Schaller, "Studies of magnetic multi-core nanoparticles for biomedical applications," Licentiate of Engineering thesis, Chalmers University of Technology, Sweden, 2009.

[81] D. Tabor, *Gases, Liquids and Solids.* Cambridge: CUP, 3rd ed., 1991.

[82] S. H. Koenig and R. D. Brown, "Relaxation of solvent protons by paramagnetic ions and its dependence on magnetic field and chemical environment: Implications for NMR imaging," *Magn. Reson. Med.*, vol. 1, pp. 478–495, 1984.

[83] S. H. Koenig and K. E. Kellar, "Theory of $1/T_1$ and $1/T_2$ NMRD profiles of solutions of magnetic nanoparticles," *Magn. Reson. Med.*, vol. 34, pp. 227–233, 1995.

[84] N. Bloembergen, E. M. Purcell, and R. V. Pound, "Relaxation effects in nuclear magnetic resonance absorption," *Phys. Rev.*, vol. 73, pp. 679–712, 1948.

[85] B. I. Bleaney and B. Bleaney, *Electricity and Magnetism.* Oxford: Clarendon Press, 2nd ed., 1965.

[86] P. S. Tofts, D. Lloyd, C. A. Clark, , G. J. Barker, G. J. M. Parker, P. McConville, C. Baldock, and J. M. Pope, "Test liquids for quantitative MRI measurements of self-diffusion coefficient in vivo," *Magn. Reson, Med.*, vol. 43, pp. 368–378, 2000.

[87] R. J. S. Brown, "Distribution of fields from randomly placed dipoles: Free-precession signal decay as a result of magnetic grains," *Phys. Rev.*, vol. 121, pp. 1379–1382, 1961.

[88] A. Roch, Y. Gossuin, R. N. Muller, and P. Gillis, "Superparamagnetic colloid suspensions: Water magnetic relaxation and clustering," *J. Magn. Magn. Mater.*, vol. 293, pp. 532–539, 2005.

[89] D. Pines and C. P. Slichter, "Relaxation times in magnetic resonance," *Phys. Rev.*, vol. 100, pp. 1014–1020, 1955.

[90] A. Roch and R. N. Muller, "Longitudinal relaxation of water protons in colloidal suspensions of superparamagnetic crystals," *Proc. 11th AM of Soc. Magn. Reson.*, p. 1447, 1992.

[91] P. Gillis, A. Roch, and R. A. Brooks, "Corrected equations for susceptibility-induced T_2-shortening," *J. Magn. Reson.*, vol. 137, pp. 402–407, 1999.

[92] A. Roch, R. N. Muller, and P. Gillis, "Theory of proton relaxation induced by superparamagnetic particles," *J. Chem. Phys.*, vol. 110, pp. 5403–5411, 1999.

[93] M. Gueron, "Nuclear relaxation in macromolecules by paramagnetic ions: A novel mechanism," *J. Magn. Reson.*, vol. 19, pp. 58–66, 1975.

[94] H. C. Torrey, "Nuclear spin relaxation by translational diffusion," *Phys. Rev.*, vol. 92, pp. 962–969, 1953.

[95] J. F. Harmon and B. H. Muller, "Nuclear spin relaxation by translational diffusion in liquid ethane," *Phys. Rev.*, vol. 182, pp. 400–410, 1969.

[96] L. P. Hwang and J. H. Freed, "Dynamic effects of pair correlation functions on spin relaxation by translational diffusion in liquids," *J. Chem. Phys.*, vol. 63, pp. 4017–4026, 1975.

[97] Y. Ayant, E. Belorizky, J. Alizon, and J. Gallice, "Calcul des densités spectrales résultant d'un mouvement aléatoire de translation en relaxation par interaction dipolaire magnétique dans les liquides," *J. Phys.*, vol. 36, pp. 991–1004, 1975.

[98] J. H. Freed, "Dynamic effects of pair correlation functions on spin relaxation by translational diffusion in liquids II. Finite jumps and independent T_1 processes," *J. Chem. Phys.*, vol. 68, pp. 4034–4037, 1978.

[99] Lusher C. P. private communication.

[100] R. Kimmich and E. Anoardo, "Field-cycling NMR relaxometry," *Prog. Nucl. Magn. Reson. Spectrosc.*, vol. 44, pp. 257–320, 2004.

[101] Chemicell GmbH, 22-23 Eresburgstrasse, 12103 Berlin, Germany; `http://www.chemicell.com`.

[102] G. F. Goya, T. S. Berquó, F. C. Fonseca, and M. P. Morales, "Static and dynamic magnetic properties of spherical magnetite nanoparticles," *J. Appl. Phys.*, vol. 94, pp. 3520–3528, 2003.

[103] C. Kittel, "Theory of the structure of ferromagnetic domains in films and small particles," *Phys. Rev.*, vol. 70, pp. 965–971, 1946.

[104] V. Schaller, U. Kräling, C. Rusu, K. Petersson, J. Wipenmyr, A. Krozer, G. Wahnström, A. Sanz-Velasco, P. Enoksson, and C. Johansson, "Motion of nanometer sized magnetic particles in a magnetic field gradient," *J. Appl. Phys.*, vol. 104, p. 093918, 2008.

[105] Teachspin Inc., Tri-Main Center – Suite 409, 2495 Main Street, Buffalo, NY 14214-2153, USA; `http://www.teachspin.com`.

[106] KTH Royal Institute of Technology, 10044 Stockholm, Sweden; `http://www.kth.se`.

[107] J. Qin, S. Laurent, Y. S. Jo, A. Roch, M. Mikhaylova, Z. M. Bhujwalla, R. N. Muller, and M. Muhammed, "A high performance magnetic resonance imaging T_2 contrast agent," *Adv. Mater.*, vol. 19, pp. 1874–1878, 2007.

[108] Amuneal Manufacturing Corp., 4737 Darrah Street, Philadelphia, PA 19124, USA; http://www.amuneal.com/.

[109] Magnetic Shields Ltd., Headcorn Road, Staplehurst, Tonbridge, Kent, TN12 0DS, UK; http://www.magneticshields.co.uk.

[110] R. C. Weast, ed., *Handbook of Chemistry and Physics*. CRC Press Inc., 63rd ed., 1982.

[111] L. Guendouz, S. M. O. A. Ghaly, A. Hedjiedj, J.-M. Escanyé, and D. Canet, "Improved Helmholtz-type magnetic resonance imaging coils with high-B_1 homogeneity – spherical and ellipsoidal four-coil systems," *Concepts Magn. Reson. B (Magn. Reson. Engineering)*, vol. 33B, pp. 9–20, 2008.

[112] K. Kaminishi and S. Nawata, "Practical method of improving the uniformity of magnetic fields generated by single and double Helmholtz coils," *Rev. Sci. Instrum.*, vol. 52, pp. 447–453, 1981.

[113] H. C. Seton, J. M. S. Hutchinson, and D. M. Bussell, "Liquid helium cryostat for SQUID-based MRI receivers," *Cryogenics*, vol. 45, pp. 348–355, 2005.

[114] Oxford Instruments plc, Tubney Woods, Abingdon, Oxfordshire, OX13 5QX, UK; http://www.oxinstdirect.com.

[115] Langtec Ltd., 1 Calder Court, Altham, Lancashire, BB5 5YB, UK; http://www.langtec.co.uk.

[116] Jackson Plating Ltd., Unit 1 Fairfields Works, Fairfields Road, Hounslow, Middlesex, TW3 1UZ, UK; http://www.jacksonplating.co.uk.

[117] F. W. Grover, *Inductance calculations: working formulas and tables*. New York: Dover Publications, 1962.

[118] H. Dyball, J. Li, C. P. Lusher, B. P. Cowan, and J. Saunders, "NMR on systems of low spin density using DC squids," *J. Low Temp. Phys.*, vol. 113, pp. 951–956, 1998.

[119] S. Appelt, H. Kühn, F. W. Häsing, and B. Blümich, "Chemical analysis by ultrahigh-resolution nuclear magnetic resonance in the Earths magnetic field," *Nat. Phys.*, vol. 2, pp. 105–109, 2006.

[120] H. Hamalainen, R. Hari, R. J. Ilmoniemi, J. Knuutila, and O. V. Lounasmaa, "Magnetoencephalography – theory, instrumentation, and applications to noninvasive studies of the working human brain," *Rev. Mod. Phys.*, vol. 65, pp. 413–497, 1993.

[121] R. H. K. Jr., P. Volegov, A. Matlachov, and M. Espy, "Toward direct neural current imaging by resonant mechanisms at ultra-low field," *NeuroImage*, vol. 39, pp. 310–317, 2008.

[122] A. M. Cassara and B. Maraviglia, "Microscopic investigation of the resonant mechanism for the implementation of nc-MRI at ultra-low field MRI," *NeuroImage*, vol. 41, pp. 1228–1241, 2008.

[123] A. M. Cassara, B. Maraviglia, S. Hartwig, L. Trahms, and M. Burghoff, "Neuronal current detection with low-field magnetic resonance: Simulations and methods," *Magn. Reson. Imag.*, vol. 27, pp. 1131–1139, 2009.

[124] Q. A. Pankhurst, N. K. T. Thanh, S. K. Jones, and J. Dobson, "Progress in applications of magnetic nanoparticles in biomedicine," *J. Phys. D: Appl. Phys.*, vol. 42, p. 224001, 2009.

[125] M. W. Wilson, R. K. Kerlan, N. A. Fidelman, A. P. Venook, J. M. LaBerge, J. Koda, and R. L. Gordon, "Hepatocellular carcinoma: Regional therapy

with a magnetic targeted carrier bound to doxorubicin in a dual MR imaging/conventional angiography suite – initial experience with four patients," *Radiology*, vol. 230, pp. 287–293, 2004.